

Analysis of pulsations and vibrations in fluid-filled pipe systems

Citation for published version (APA):

Jong, de, C. A. F. (1994). *Analysis of pulsations and vibrations in fluid-filled pipe systems*. [Phd Thesis 1 (Research TU/e / Graduation TU/e), Mechanical Engineering]. Technische Universiteit Eindhoven. <https://doi.org/10.6100/IR423649>

DOI:

[10.6100/IR423649](https://doi.org/10.6100/IR423649)

Document status and date:

Published: 01/01/1994

Document Version:

Publisher's PDF, also known as Version of Record (includes final page, issue and volume numbers)

Please check the document version of this publication:

- A submitted manuscript is the version of the article upon submission and before peer-review. There can be important differences between the submitted version and the official published version of record. People interested in the research are advised to contact the author for the final version of the publication, or visit the DOI to the publisher's website.
- The final author version and the galley proof are versions of the publication after peer review.
- The final published version features the final layout of the paper including the volume, issue and page numbers.

[Link to publication](#)

General rights

Copyright and moral rights for the publications made accessible in the public portal are retained by the authors and/or other copyright owners and it is a condition of accessing publications that users recognise and abide by the legal requirements associated with these rights.

- Users may download and print one copy of any publication from the public portal for the purpose of private study or research.
- You may not further distribute the material or use it for any profit-making activity or commercial gain
- You may freely distribute the URL identifying the publication in the public portal.

If the publication is distributed under the terms of Article 25fa of the Dutch Copyright Act, indicated by the "Taverne" license above, please follow below link for the End User Agreement:

www.tue.nl/taverne

Take down policy

If you believe that this document breaches copyright please contact us at:

openaccess@tue.nl

providing details and we will investigate your claim.

ANALYSIS OF PULSATIONS AND VIBRATIONS
IN FLUID-FILLED PIPE SYSTEMS

PROEFSCHRIFT

ter verkrijging van de graad van doctor aan de
Technische Universiteit Eindhoven, op gezag van
de Rector Magnificus, prof.dr. J.H. van Lint,
voor een commissie aangewezen door het College
van Dekanen in het openbaar te verdedigen op
vrijdag 21 oktober 1994 om 16.00 uur

door

Christiaan Arnoldus Franciscus de Jong

geboren te Goirle

Dit proefschrift is goedgekeurd
door de promotoren:

prof.dr.ir. J.W. Verheij

prof.dr.ir. G.J.F. van Heijst

ANALYSIS OF PULSATIONS AND VIBRATIONS
IN FLUID-FILLED PIPE SYSTEMS

CIP-DATA KONINKLIJKE BIBLIOTHEEK, DEN HAAG

Jong, Christiaan Arnoldus Franciscus de

Analysis of pulsations and vibrations in fluid-filled pipe systems / Christiaan Arnoldus Franciscus de Jong. -

Eindhoven : Eindhoven University of Technology

Thesis Eindhoven. - With ref.

ISBN 90-386-0074-7

Subject headings: pipe systems ; vibration analysis / pipe systems ; acoustic measurements / centrifugal pumps.

Copyright © 1994, by the TNO Institute of Applied Physics, Delft, Netherlands

Cover design: Gerard Scholten and Wouter Mierop

ABSTRACT

Pressure pulsations and mechanical vibrations in pipe systems may cause excessive noise and may even lead to damage of piping or machinery. The excitation mechanism can be hydraulic or mechanical. In fluid-filled pipe systems pulsations and vibrations will be strongly coupled. In the present study calculation and measurement methods have been developed for the analysis of vibrations and pulsations in fluid-filled pipe systems, taking fluid-structure interaction into account.

A calculation model has been developed for the simulation of pulsations and vibrations in fluid-filled pipe systems. The analytical model is based on the transfer matrix method. It describes pressure waves in the fluid and axial extensional waves, bending waves and torsional waves in the pipes. Fluid pulsations and mechanical vibrations are coupled at discontinuities (like elbows and T-junctions) and via Poisson contraction of the pipe wall. For a given source description the model calculates pulsation and vibrations levels, but also for example mode shapes and vibro-acoustic energy flow. The practicability of the calculation model and the effects of fluid-structure interaction are illustrated by calculations for some simple systems.

Apart from the calculation method, experimental methods have also been developed. These are indirect methods for the determination of quantities like acoustic source strength, acoustical and mechanical impedance and energy flow. These quantities are important to diagnose the causes of excessive noise and vibrations and to determine input parameters for the calculation model. They are derived from measurements of pipe wall accelerations and fluid pressure pulsations, in combination with models for the dynamic behaviour of the pipe system.

The prediction and measurement methods have been tested in experiments on simple laboratory test rigs. Measurements have been performed on a straight water-filled pipe, on a system of two pipes connected by an elbow and on a system of two pipes and a rubber bellows. Generally the results of measurements and calculations agree quite well. Deviations can be attributed to an insufficiently accurate modelling of the boundary conditions.

Centrifugal pumps are important sources of pulsations and vibrations in pipe systems. Therefore much attention has been given to the testing of an indirect measurement method for the characterisation of a centrifugal pump with respect to the generation and transmission of fluid pulsations. The transfer matrix of the pump has been determined using external fluid excitation. Next, the generation of fluid pulsations is characterised by an equivalent source strength vector. In the absence of cavitation it appears that the pump generates predominantly fluctuating forces on the fluid. The method that is developed here may be used to investigate to what extent the generation of fluid pulsations is influenced by the design and the operating condition of the pump.

SAMENVATTING

Druk pulsaties en mechanische trillingen in pijpleidingsystemen kunnen geluidsoverlast veroorzaken en kunnen zelfs leiden tot beschadiging van pijpen of machines. Het aanstootmechanisme kan zowel van hydraulische als van mechanische aard zijn. Daarbij zullen pulsaties en trillingen elkaar in vloeistofge vulde leidingsystemen sterk beïnvloeden. In het hier beschreven onderzoek zijn reken- en meetmethoden ontwikkeld voor het analyseren van pulsaties en trillingen in vloeistofge vulde pijpleidingsystemen, waarbij de interactie tussen vloeistof en constructie in rekening wordt gebracht.

Er is een rekenmodel ontwikkeld voor het simuleren van pulsaties en trillingen in vloeistofge vulde pijpleidingsystemen. Het analytische rekenmodel is gebaseerd op de methode van overdrachtsmatrices. Het beschrijft drukgolven in de vloeistof en axiale rekgolven, buiggolven en torsiegolven in de pijpen. Vloeistofpulsaties en mechanische trillingen zijn gekoppeld bij discontinuïteiten (zoals bochten en vertakkingen) en via dwarscontractie van de pijp wand. Bij een gegeven bronbeschrijving levert het rekenmodel pulsatie- en trillingsniveaus, maar ook bijvoorbeeld trilvormen en akoestische energiestromen. Het gebruik van het rekenmodel en de effecten van vloeistof-constructie interactie worden getoond aan de hand van berekeningen aan enkele eenvoudige systemen.

Naast de rekenmethode zijn ook experimentele methoden ontwikkeld. Het betreft hier indirecte methoden voor het bepalen van grootheden zoals akoestische bronsterkte, akoestische en mechanische impedantie en energiestroom. Deze grootheden zijn een belangrijk hulpmiddel bij het opsporen van de oorzaken van geluid- of trillingsoverlast en bij het bepalen van invoergegevens voor het rekenmodel. Ze worden afgeleid uit metingen van versnelling van de pijp wand en drukpulsaties in de vloeistof, in combinatie met modellen voor het dynamische gedrag van het pijpleidingsysteem.

De reken- en meetmethoden zijn getoetst aan de hand van experimenten aan eenvoudige laboratoriumopstellingen. Er zijn metingen verricht aan een rechte pijp gevuld met water, twee pijpen verbonden via een bocht en een systeem van twee pijpen met een rubberbalg. Over het algemeen komen de resultaten van metingen en berekeningen behoorlijk goed overeen. Afwijkingen kunnen worden toegeschreven aan een onvoldoende nauwkeurige beschrijving van de randvoorwaarden.

Centrifugaalpompen vormen een belangrijke bron van drukpulsaties en trillingen in pijpleidingsystemen. Daarom is uitgebreid aandacht besteed aan het toetsen van een indirecte meetmethode voor het karakteriseren van een centrifugaalpompe met betrekking tot de opwekking en transmissie van vloeistofpulsaties. De overdrachtsmatrix van de pompe is bepaald met behulp van externe vloeistofaanstoting. De opwekking van vloeistofpulsaties in de pompe is vervolgens gekarakteriseerd door middel van een equivalente bronsterktevector. Bij afwezigheid van cavitatie in de pompe blijkt deze vooral wisselkrachten op de vloeistof uit te oefenen. Met behulp van de hier ontwikkelde methode kan worden onderzocht in hoeverre het ontwerp en de bedrijfsinstelling van de pompe de opwekking van vloeistofpulsaties beïnvloedt.

ACKNOWLEDGEMENTS

This doctoral thesis is based upon research projects sponsored by the TNO Defence Research Organisation and the TNO Institute of Applied Physics (TNO-TPD-TU Delft). Their permission for publication is gratefully acknowledged.

The author thanks everyone who contributed to the completion of this thesis, in particular:

- Dr.ir. J.C. Bruggeman and prof.dr.ir. J.W. Verheij for their supervision and continuous support during the research programme and the writing of the manuscript.
- the students E.J.S. Penseel, M.J.G. Frankenmolen, P.C. Kriesels and J.F.M. van Boven for their contributions to the computer programming, the experiments and the analysis.
- A.W. Witvliet for helping to design and building the test arrangements.
- ing. F.G.P. van der Knaap for his support in some of the experiments.
- Dr.ir. A. Hirschberg, prof.dr.ir. G.J.F. van Heijst and dr. D.J. Thompson for their comments upon the manuscript.

CONTENTS

ABSTRACT	v
SAMENVATTING	vi
ACKNOWLEDGEMENTS	vii
1. INTRODUCTION	1
1.1 Noise and vibrations in pipe systems	1
1.2 Review of the state-of-the-art	2
1.2.1 prediction methods	2
1.2.2 experimental methods	5
1.3 Objective and approach	6
1.4 Outline of this thesis	7
2. WAVE PROPAGATION IN STRAIGHT FLUID-FILLED PIPES	9
2.1 Introduction	9
2.2 Equations of motion	9
2.2.1 shell motion	9
2.2.2 fluid motion	13
2.3 Solution of the equations of motion	14
2.3.2 dispersion equation	16
2.3.3 internal and external fluid loading	17
2.4 Dispersion curves and approximate equations	18
2.4.1 $n=0$	19
2.4.2 $n>0$	19
2.5 Amplitude ratios	23
2.5.1 $n=0$	23
2.5.2 $n>0$	24
2.6 Vibro-acoustic energy flow	24
2.6.1 fluid-borne energy flow	25
2.6.2 structure-borne energy flow	25
2.6.3 total axial energy flow	26
2.6.4 approximate energy flow equations	26
2.7 Beam model	28
2.7.1 axial motion of pipe and fluid	29
2.7.2 flexural motion	30
2.7.3 torsional motion	30
2.8 Conclusion	31

3.	A TRANSFER MATRIX MODEL FOR THE DYNAMIC BEHAVIOUR OF FLUID-FILLED PIPE SYSTEMS	33
3.1	Introduction	33
3.2	Solution methods	34
3.2.1	system response	35
3.2.2	impedance matrix	36
3.3	Transfer matrix model for a fluid-filled pipe system	37
3.3.1	solution of the differential equations	38
3.3.2	scaling	38
3.3.3	straight fluid-filled pipes	39
3.3.4	curved pipes or elbows	42
3.3.5	other components	49
3.3.6	intermediate boundary conditions	52
3.4	Computer program <i>PRESTO</i>	54
3.4.1	numerical solution	54
3.4.2	accuracy	55
3.5	Examples	56
3.5.1	fluid-structure interaction at an end plate	56
3.5.2	response of a simple pump circuit	57
3.6	Conclusion	59
4.	EXPERIMENTAL METHODS	61
4.1	Introduction	61
4.2	Wave decomposition	62
4.2.1	circumferential mode decomposition	63
4.2.2	axial wave decomposition	65
4.2.3	the two-channel method	67
4.2.4	non-intrusive measurement of pressure pulsations	71
4.2.5	the four-channel method	73
4.3	Inverse method	76
4.4	Conclusion	78
5.	VALIDATION EXPERIMENTS	79
5.1	Introduction	79
5.2	A straight pipe	79
5.2.1	test arrangement	79
5.2.2	axial wave decomposition	84
5.2.3	axial mobility matrix at the bottom mass	86
5.2.4	transverse wave decomposition	88

5.2.5	internal wall pressure caused by transverse acceleration	89
5.2.6	comparison with <i>PRESTO</i> calculations	91
5.3	A pipe system with a 90° elbow	96
5.3.1	test arrangement	96
5.3.2	comparison with <i>PRESTO</i> calculations	97
5.4	Axial transmission through a rubber bellows	101
5.4.1	test arrangement	103
5.4.2	measurement results	104
5.5	Conclusion	108
6.	ACOUSTIC CHARACTERIZATION OF A CENTRIFUGAL PUMP	111
6.1	Introduction	111
6.2	A two-port model for the centrifugal pump	113
6.3	Characterization method and procedure	115
6.4	Description of the test facility and instrumentation	117
6.4.1	the centrifugal pump	117
6.4.2	the test loop	118
6.4.3	external excitation	119
6.4.4	pressure transducers, calibration and data processing	120
6.4.5	linearity, stability and accuracy	121
6.5	Experimental determination of the passive transfer matrix	123
6.5.1	pump at standstill	124
	pump operating	128
6.6	Experimental determination of the fluid pulsation source strength	129
6.6.1	source strength at different operating conditions	134
6.7	Conclusion	138
7.	EVALUATION	141
	APPENDIX A: Numerical solution of the dispersion equation	145
	APPENDIX B: Derivation of the beam model for a straight fluid-filled pipe	147
	NOMENCLATURE	151
	REFERENCES	155
	CURRICULUM VITAE	165

1. INTRODUCTION

1.1 Noise and vibrations in pipe systems

In many situations where machines are operating and fluids are transported, pipe systems are responsible for the transmission of noise, e.g. in buildings, ships, power plants, process plants, etc. The effectiveness of noise control measures, like the resilient mounting and acoustic enclosure of machines, may be limited due to noise transmission along pipes. Moreover, pipe systems are a critical factor in the reliability of systems. Excessive vibrations may lead to fatigue and cause damage to vital parts of installations. Fluid pulsations may also cause incorrect reading of flow meters and other control devices. On the other hand, the monitoring of pulsations or vibrations can be valuable to diagnose malfunction of machinery.

To be able to solve, or rather prevent, reliability and noise problems it is of great importance to understand the mechanisms that are responsible for the generation and the propagation of fluid pulsations and mechanical vibrations in the piping. The study of these mechanisms is the starting point in the development of practical methods for the analysis of the vibro-acoustic behaviour of fluid-filled pipe systems. Such an analysis is required to decide on the appropriate design of the pipe system or of noise and vibration reduction measures.

Noise and vibrations in pipe systems may be generated in pumps, compressors, pressure-reducing valves, bends, etc. The source mechanisms can be either hydraulic or mechanical. Turbulent flow and local flow instabilities in, for example, pumps, valves or side-branches will excite fluid pulsations. Mechanical vibrations may be excited by, for example, unbalance in rotating machinery. The distinction between hydraulic and mechanical source mechanisms is not always clear, because fluid pulsations may excite structural vibrations at the source and vice-versa.

There are many different ways in which vibro-acoustic energy can be transmitted in fluid-filled pipe systems. Several types of fluid- and structure-borne waves can propagate along a straight pipe. At each discontinuity (e.g. elbow or pipe support) the energy may be redistributed by coupling of these waves. This means that a noise or vibration reduction measure that treats only one type of wave may be largely ineffective, because it is short-circuited by transmission via other waves.

The complexity of the vibro-acoustic behaviour of flexible, fluid-filled pipe systems is predominantly determined by two parameters: the frequency and the ratio of the masses per unit pipe length of fluid and pipe wall. The number of simultaneously propagating waves in the pipes increases with frequency. The mass ratio determines whether fluid-borne and structure-borne waves may be treated separately. If this ratio is close to one, fluid pulsations and mechanical vibrations will be strongly coupled, so that it becomes necessary to take their interaction into account when analysing the dynamic behaviour.

This thesis presents some new contributions to theoretical and experimental methods to analyze this coupled behaviour. The methods are especially useful for application in systems with a heavy, homogeneous fluid (like water or oil). The description of the dynamic behaviour of two-phase flows is not covered. The present discussion focuses on deterministic methods to analyze the linear elastic behaviour of pipe systems in a frequency range where the number of propagating waves is limited. Non-linear deformations fall outside the scope of this thesis, which is aimed at noise and vibration control.

In the high-frequency range, where the pipe cross-section is larger than the acoustic and vibrational wavelengths, the vibro-acoustic behaviour of the piping is governed by a large number of waves. Fluid-borne and structure-borne waves will be strongly coupled, even independent of the mass ratio, because the wavelengths of both waves may coincide. This makes a deterministic analysis of the dynamic behaviour practically impossible. Statistical Energy Analysis (*SEA*) [Lyon 1975] is a more useful approach in this frequency range [White & Sawley 1972].

1.2 Review of the state-of-the-art

Because the problem of noise and vibrations in pipe systems has many aspects, this review is limited to deterministic prediction and measurement methods to analyze the dynamic behaviour of fluid-filled pipe systems. For general information about noise in pipeline systems the reader is referred to, for example, [VDI 3733, 1983] or [de Vos 1984].

1.2.1 prediction methods

The dynamic behaviour of fluid-filled pipe systems has been studied extensively during the last decades. Different applications have led to a wide range of publications variously related in subject. At least four application areas can be distinguished:

- 1) The analysis of water-pipe systems with relation to waterhammer (i.e. a strong transient flow, e.g. due to the rapid closing or opening of a valve), see for example

[Wylie & Streeter 1978].

- 2) The analysis of the instability of fluid-conveying pipes, that is of importance for high velocity flow through a flexible pipe, such as those used in the feed lines to rocket motors and water turbines, see for example [Blevins 1977].
- 3) The analysis of noise and vibrations of hydraulic pipe systems, see for example [Stulemeijer 1981; Ham 1982].
- 4) The analysis of fluid-filled pipes as acoustic waveguides, see for example [Junger & Feit 1982; Cremer, Heckl & Ungar 1988].

Generally only few cross-references to other application areas can be found in the publications on this subject. This thesis attempts to integrate, where appropriate, the methods of the different application areas (especially of 3 and 4).

The first three application areas are limited to the low-frequency range, where the fluid-borne noise propagates in plane waves only and the mechanical vibrations in the pipes propagate in longitudinal, flexural and torsional waves only. Traditionally, steady-flow and waterhammer analysis of hydraulic pipe systems are carried out under the assumption that the fluid pulsations and mechanical vibrations may be treated separately. The analysis method generally consists in calculating the pulsation pressure distribution in the fluid, either in the frequency domain, using the transfer matrix method [Stulemeijer 1981; Ham 1982], or in the time domain, using the method of characteristics [Smeulers 1988; Van Bokhorst *et al.* 1993]. Then this pressure distribution is used as input for a mechanical response study, e.g. using a finite element code. This method does take into account that the pipe wall elasticity reduces the propagation velocity of fluid-borne waves, but the interaction of pulsations and vibrations is otherwise neglected. The uncoupled approach is valid for gas-filled systems, but it may lead to erroneous results when applied to systems with a heavier fluid, where coupling is important.

This thesis is concerned with pipes in which the fluid-flow velocity is much smaller than the critical velocity at which the pipes become unstable, see Blevins [1977].

Several authors have presented methods to calculate the coupled dynamic behaviour of fluid-filled pipe systems, using the transfer matrix method (TMM) [Wilkinson 1978; El-Raheb 1981; Nanayakkara & Duke Perreira 1986; Lesmez 1989; Tentarelli 1990; de Montussaint & Trollé 1992], the method of characteristics (MOC) [Wiggert, Hatfield & Stuckenbruck 1987; Tijsseling 1993], the finite element method (FEM) [Everstine 1986] or an iterative method based on the MOC for the fluid and on the FEM for the structure [Kruisbrink & Heinsbroek 1992]. Both the MOC and the FEM have the disadvantage that they need a much finer discretization of the piping than the TMM and consequently

require a larger computer. As far as linear deformations are concerned, time domain methods (MOC) and frequency domain methods (TMM,FEM) in principle lead to the same results, at least to results that may easily be converted to each other by means of Fourier transformation. However, it is practical to study transient phenomena with a time domain method and steady state phenomena with a frequency domain method. The TMM, as a tool to determine the steady dynamic behaviour of linear structures of pipes or beams, is considerably more efficient than a wave reflection description (e.g. [Horner & White 1991]).

All of these methods start from a (more or less elaborate) set of equations of motion for a flexible, fluid-filled beam. However, at somewhat higher frequencies a pipe should be described as a cylindrical shell instead of a beam. The equations of motion for a straight, infinitely long, fluid-filled, cylindrical shell have been described and solved by Fuller & Fahy [1982]. A study of this shell-type behaviour is important to establish the limits of applicability of the beam-type equations of motion. Moreover, it is important to recognize that shell-type deformations may influence acceleration measurements on a pipe. Fuller [1981;1983;1984] has studied the effects of different types of excitation and of wall discontinuities and radial constraints on wave propagation in an infinitely long, circular cylindrical shell. Although these studies give a good insight in the local coupling mechanisms, they do not lead to a method to predict the dynamic behaviour of practical pipe systems, that is predominated by resonances due to reflections at elbows and other discontinuities. (*Note: for the same reason the results of a study of active control of coupled waves in infinitely long fluid-filled pipes [Brévert & Fuller 1993] are not directly applicable to practical pipe systems*). On the other hand, El-Raheb and Wagner [1985] have described a method to calculate the coupled harmonic response of cylindrical and toroidal shells to an internal acoustic field but this is only appropriate for application to very short pipes.

The literature on modelling of the generation of vibrations and pulsations in fluid-filled pipe-systems is scarce. To limit the scope of the subject we will only consider the generation of pulsations by unsteady flow. Bruggeman [1987] and Peters [1993] have investigated the application of vortex methods to study the generation of flow-induced pulsations in a pipe system with side branches. However, most sources of flow-induced noise in pipe systems exhibit more complicated flow patterns. At the moment their source strength can only be predicted on the basis of some semi-empirical models. An important example is Simpson's [1966;1967] correlation formula for the generation of hydraulic noise in centrifugal pumps. At the first international conference on pump noise and vibration in Clamart (1993) (see e.g. Bolleter [1993]) it appeared that there are no other quantitative models that relate the unsteady flow in a centrifugal pumps to an acoustic

source strength. The unsteady flow field inside a centrifugal pump has been studied using the FEM, see e.g. Badie [1993] and Thompson *et al* [1993], and various measurement methods, see e.g. Thompson *et al* [1993], Chu *et al* [1993] and Liu *et al* [1994]. However, these studies do not give information on the pressure pulsations that are radiated into the suction and discharge pipes, because they do not consider the effect of the dynamic response of these pipes. Further investigations are required to relate the unsteady flow field inside a pump to its acoustic source strength.

1.2.2 experimental methods

A large proportion of the publications on noise and vibrations in fluid-filled pipe systems concerns theoretical work. However, for lack of accurate models for several pipe system components, experimental methods are indispensable. Single point pressure or vibration measurements cannot be categorized as 'experimental method'. Since the dynamic behaviour of a fluid-filled pipe is governed by the simultaneous presence of several types of propagating waves, it is necessary to perform a decomposition of the wave contributions for a reliable analysis of the results of experiments.

Wave decomposition methods have been developed with application to acoustic and structural intensity measurement methods [Noiseux 1970; Pavić 1976; Fahy 1977; Chung & Blazer 1980]. Pavić [1976;1992] and Verheij [1980;1982] have described the configurations of accelerometers or strain gauges to determine the energy flow per wave that is propagating along a beam or a pipe. Esparcieux [1986] has shown that the contributions of different waves to the wave field on a straight pipe can be determined by means of a wavenumber-frequency transformation technique. De Jong & Verheij [1992] have described an extension of the wave decomposition methods for a beam to higher order waves with shell deformation and applied this method to the first shell-type waves on an empty steel pipe. The same method has been applied by Bourget & Fahy [1993].

Measurements on a single configuration of a pipe system reveal the actual vibro-acoustic behaviour of the system, but give only limited information on source and transmission characteristics of pipe system components. Linear source and system response effects can be separated using measurements on multiple system configurations. Changes in configuration may be achieved by connecting or disconnecting system components, or by applying artificial excitation to the system.

Verheij, Janssens & Thompson [1993] describe an experimental method to determine the contribution of the transmission along a specific sound path (e.g. a pipe system) to the total sound transfer from a machine to a receiver location. This '*equivalent forces*' method involves measurements when the machine is running and extra measurements when the

machinery is switched off, with artificial excitation of the pipe system under investigation by means of substitution sources (e.g. electrodynamic shakers). The set of equivalent forces which between them would generate similar vibrations in the pipe system as the machinery does, is determined using a matrix inversion. It is assumed that the artificial excitation can simulate the machinery noise sufficiently accurate. Statistically, this assumption is fulfilled if the sound path exhibits many modes of vibration in a frequency band, of which many are excited. If a noise source produces some strong tonal components, or if the sound path exhibits a limited number of modes, it is necessary to use a deterministic inversion method, which is based on a correct description of the dynamic behaviour of the pipe system.

Bodén [1989] gives an overview of the literature that has been produced on the subject of experimental characterization of fluid machines as sources of fluid-borne noise. It concerns 'inverse methods' to determine the source characteristics from a series of experiments at different system configurations. Recently, Frikha [1992] has proposed to use inverse methods to determine acoustic or vibrational source strength or transmission characteristics in pipe systems by means of an inverse method. However, the research into the application of inverse methods to characterize the vibro-acoustic behaviour of pipe system components is still in its infancy.

1.3 Objective and approach

The research programme that is described in this thesis has been aimed at *the development of theoretical and experimental methods for a quantitative description of the generation and propagation of noise and vibrations in fluid-filled pipe systems.*

It was decided to concentrate on relatively low frequencies, where deterministic methods are most promising. The materials and the dimensions of the piping determine the upper frequency at which these methods are still valid. The deterministic methods are especially useful to investigate noise and vibrations caused by sources with strong tonal components (e.g. blade passage tones of a centrifugal pump) in pipe systems with a limited number of resonant modes. These phenomena are of interest for low-frequency noise control (which is highly relevant for naval, oceanographic and fishery ships) and for the reliability of pipe systems in power and process plants.

A calculation method has been developed to predict the vibro-acoustic behaviour of fluid-filled pipe systems, using the formalism of the transfer matrix method (TMM). Unlike the existing TMM models for pipe systems, it is based on a detailed study of the propagation

of fluid- and structure-borne waves in fluid-filled cylindrical shells. The interaction of fluid pulsations and mechanical vibrations is taken into account. The method has been implemented in a computer program. The numerical accuracy has been investigated and the predictions have been validated by comparison with the results of some laboratory experiments. The program can be used to predict vibration levels and noise transfer in pipe systems in the design stage and to study the effects of design adjustments and noise reducing measures.

New experimental methods have been developed to decompose the contributions of the different fluid- and structure-borne waves to the wave field in the piping. Like the calculation method they are based on a detailed study of the wave propagation in fluid-filled piping. The wave decomposition gives access to descriptors of the vibro-acoustic behaviour of the pipe system, like for instance the vibro-acoustic energy flow, which quantifies the importance of the pipe system as a noise transmission path, compared with other paths.

With regard to noise generation an inverse measurement method has been developed to separate the source characteristics from the system response. Centrifugal pumps are so widely used that it was considered appropriate to test the method on a centrifugal pump.

1.4 Outline of this thesis

This thesis describes theoretical and experimental methods for the analysis of fluid pulsations and mechanical vibrations in fluid-filled pipe systems. Chapter 2 presents a review of the theory of wave propagation in straight fluid-filled pipes. It describes the derivation of the simplified (low-frequency) equations on which the calculation and measurement methods are based. The transfer matrix model for the prediction of the dynamic behaviour of fluid-filled pipe systems is presented in chapter 3. Transfer matrices for several pipe system components (straight and curved pipes, pipe supports, flanges, etc.) are derived. The solution method, the computer program and the numerical accuracy are discussed. The importance of fluid-structure interaction for the dynamic behaviour is demonstrated by two numerical examples. Chapter 4 treats the fundamentals of the experimental methods. Experiments have been performed on three laboratory test arrangements, that were designed to validate the calculation model and to test the experimental methods. These experiments are presented in chapter 5. Chapter 6 describes the experimental method to characterize a source of fluid pulsations. The method is applied to a centrifugal pump. Finally, an evaluation of this study is presented in chapter 7.

2. WAVE PROPAGATION IN STRAIGHT FLUID-FILLED PIPES

2.1 Introduction

The theory of the propagation of vibro-acoustic waves in fluid-filled, cylindrical elastic shells has been described in detail by Fuller & Fahy [1982], Möser, Heckl & Ginters [1986] and Pavić [1990]. The objective of this chapter is to present a review of the assumptions and equations, to describe the wave propagation and to develop the simplified equations that form a basis for the calculation model of Chapter 3 and the experimental methods of Chapter 4.

2.2 Equations of motion

This section describes the equations of motion for a straight, fluid-filled, circular cylindrical shell of infinite length. Both pipe wall material and fluid are assumed to be homogeneous and isotropic. The equations describe the linear elastic behaviour of pipe and fluid.

2.2.1 shell motion

The derivation of the equations that describe the vibration of a circular cylindrical shell can be found in many textbooks [Leissa 1973; Soedel 1981; Cremer, Heckl & Ungar 1988]. The different shell theories represent a simplification of the three-dimensional theory of linear elasticity. Shell theory can be applied if the thickness of the shell is small compared with the other dimensions, like the radius of curvature of the middle surface of the shell and the axial length of the shell. It is assumed that the deformation of the shell is small compared to its thickness and that Kirchhoff's hypothesis applies: "normals to the undeformed middle surface remain straight and normal to the deformed middle surface and suffer no extension". Through these assumptions the shell is considered to have a special orthotropy: an infinite stiffness in the radial direction, hence normal and shear strains vanish in this direction.

The geometry and the coordinate system for the circular cylindrical shell are shown in figure 2.1. a is the radius of curvature of the middle surface of the shell, h is the shell's thickness, z , r and θ are the cylindrical coordinates and u , v and w the orthogonal components of displacement of the shell. By Kirchhoff's assumption the displacement varies

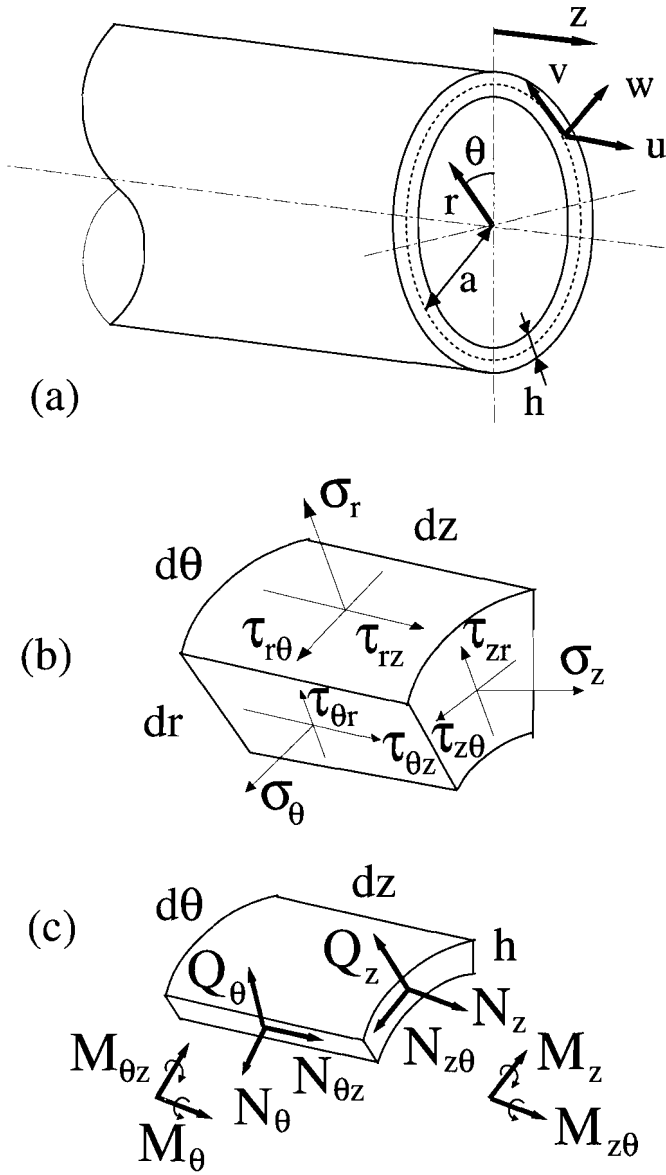


Figure 2.1: (a) geometry and cylindrical coordinate system
 (b) stresses on an infinitesimal shell element
 (c) resultant forces and moments on the pipe wall

linearly through the shell thickness:

$$u \approx u_o - (r-a) \frac{\partial w_o}{\partial z}, \quad v \approx v_o - \frac{r-a}{a} \left(\frac{\partial w_o}{\partial \theta} - v_o \right), \quad w \approx w_o, \quad (2.1)$$

where the subscript 'o' refers to the middle surface of the shell. The three remaining strain-displacement equations for the thin-walled shell are:

$$\epsilon_z = \frac{\partial u}{\partial z}, \quad \epsilon_\theta = \frac{1}{a} \frac{\partial v}{\partial \theta} + \frac{w}{a}, \quad \gamma_{z\theta} = \gamma_{\theta z} = \frac{\partial v}{\partial z} + \frac{1}{a} \frac{\partial u}{\partial \theta} \quad (2.2)$$

and the matching stress-strain equations:

$$\sigma_z = \frac{E_s}{1-\nu^2} (\epsilon_z + \nu \epsilon_\theta), \quad \sigma_\theta = \frac{E_s}{1-\nu^2} (\epsilon_\theta + \nu \epsilon_z), \quad \tau_{z\theta} = \frac{E_s}{2(1+\nu)} \gamma_{z\theta}. \quad (2.3)$$

Here E_s denotes Young's modulus of elasticity and ν Poisson's ratio. Hysteretic losses in the shell material are accounted for in a loss factor η , so that $E_s = Re(E_s)(1+i\eta)$.

Although the strains in radial direction vanish by assumption, the corresponding stresses σ_r , τ_{zr} and $\tau_{\theta r}$ cannot be neglected a priori. The equations of motion for an infinitesimal element of the shell are, in cylindrical coordinates:

$$\begin{aligned} \frac{\partial \sigma_z}{\partial z} + \frac{1}{r} \frac{\partial \tau_{z\theta}}{\partial \theta} + \frac{1}{r} \frac{\partial}{\partial r} (r \tau_{zr}) &= \rho_s \frac{\partial^2 u}{\partial t^2}, \\ \frac{1}{r} \frac{\partial \sigma_\theta}{\partial \theta} + \frac{\partial \tau_{z\theta}}{\partial z} + \frac{1}{r} \frac{\partial}{\partial r} (r \tau_{\theta r}) + \frac{\tau_{\theta r}}{r} &= \rho_s \frac{\partial^2 v}{\partial t^2}, \\ \frac{1}{r} \frac{\partial}{\partial r} (r \sigma_r) + \frac{\partial \tau_{zr}}{\partial z} + \frac{1}{r} \frac{\partial \tau_{\theta r}}{\partial \theta} - \frac{\sigma_\theta}{r} &= \rho_s \frac{\partial^2 w}{\partial t^2}. \end{aligned} \quad (2.4)$$

Only translatory inertia forces are accounted for, other volume forces, like gravity or thermal stress, have been neglected.

The absence of radial stress-strain equations is compensated for by using an integral formulation and applying boundary conditions for the normal and shear stresses at the inner and outer surfaces of the shell:

$$\begin{aligned} \sigma_r(r=a_i) &= p^i(r=a_i), \quad \tau_{zr}(r=a_i) \approx \tau_{\theta r}(r=a_i) \approx 0, \\ \sigma_r(r=a_e) &= -p^e(r=a_e), \quad \tau_{zr}(r=a_e) \approx \tau_{\theta r}(r=a_e) \approx 0, \end{aligned} \quad (2.5)$$

where $a_i = a - h/2$ and $a_e = a + h/2$ denote the internal and external radii of the shell and p^i and

p^e the internal and external fluid pressures. Friction between fluid and shell has been neglected, so that the shear stresses vanish.

The stress-strain equations (2.3) and the equations of motion (2.4) are expressed in terms of the classical force and moment 'resultants' $\{N_z, N_{z\theta}, N_\theta, N_{\theta z}, Q_z, Q_\theta, M_z, M_{z\theta}, M_\theta, M_{\theta z}\}$ (see fig.2.1) by integration of the stresses $\{\sigma_z, \sigma_\theta, \tau_{z\theta}, \tau_{zr}, \tau_{\theta r}\}$ across the shell thickness, see Leissa [1973] or Soedel [1981]. The different 'thin shell' ($h/a \ll 1$) approximations that can be applied in this integration have led to many sets of shell equations that only differ in terms proportional to the non-dimensional shell thickness parameter β^2 . This parameter is defined as:

$$\beta^2 = \frac{h^2}{12a^2} . \quad (2.6)$$

NOTE: For practical pipes h/a will seldom exceed 0.25, hence β^2 will be smaller than 0.005.

The equations of motion are expressed in terms of the force and moment resultants by integration of equations (2.4) over the shell thickness. The internal and external fluid pressures are transferred into the equations of motion by application of the boundary conditions (2.5) in the integration:

$$\int_{a_i}^{a_e} \frac{1}{r} \frac{\partial}{\partial r} (r\sigma_r) \frac{r}{a} dr = \left(1 - \frac{h}{2a}\right) p^i (r=a_i) - \left(1 + \frac{h}{2a}\right) p^e (r=a_e) . \quad (2.7)$$

NOTE: The $h/2a$ terms in this equation are the only terms in the equations of motion for the fluid-filled shell that are linear in h/a . Many authors [Fuller & Fahy 1982; Pavić 1990; Junger & Feit 1986] implicitly assume that these terms are negligibly small, while they are larger than the β^2 terms that are retained in their equations.

The integration of the set of equations of motion over the shell thickness, neglecting some minor terms of order β^2 , yields the Love-equations (here including the effects of internal and external fluid loading):

$$\begin{aligned}
\frac{\partial N_z}{\partial z} + \frac{1}{a} \frac{\partial N_{z\theta}}{\partial \theta} &= \rho_s h \frac{\partial^2 u_o}{\partial t^2}, \\
\frac{\partial N_{\theta z}}{\partial z} + \frac{1}{a} \frac{\partial N_\theta}{\partial \theta} + \frac{Q_\theta}{a} &= \rho_s h \frac{\partial^2 v_o}{\partial t^2}, \\
\frac{a_i}{a} p^i(r=a_i) - \frac{a_e}{a} p^e(r=a_e) + \frac{\partial Q_z}{\partial z} + \frac{1}{a} \frac{\partial Q_\theta}{\partial \theta} - \frac{N_\theta}{a} &= \rho_s h \frac{\partial^2 w_o}{\partial t^2}, \\
\frac{\partial M_z}{\partial z} + \frac{1}{a} \frac{\partial M_z}{\partial \theta} &= -Q_z, \quad \frac{\partial M_{z\theta}}{\partial z} + \frac{1}{a} \frac{\partial M_\theta}{\partial \theta} = -Q_\theta.
\end{aligned} \tag{2.8}$$

Rotatory inertia has been neglected in the last two equations, as its effects are equally important as the effects of radial shear deformation, that disappear due to the Kirchhoff hypothesis [Leissa 1973].

2.2.2 fluid motion

In the absence of sources, the fluid density ρ_f and the three orthogonal components of the fluid displacement ξ_z , ξ_r and ξ_θ fulfil the linearized equation of continuity for a homogeneous, compressible fluid [Michalke 1989]:

$$\frac{\partial \rho_f}{\partial t} + \rho_f \left\{ \frac{\partial^2 \xi_z}{\partial z \partial t} + \frac{1}{r} \frac{\partial}{\partial r} \left(r \frac{\partial \xi_r}{\partial t} \right) + \frac{1}{r} \frac{\partial^2 \xi_\theta}{\partial \theta \partial t} \right\} = 0. \tag{2.9}$$

Effects of mean flow are neglected, because the Mach-number, the ratio of the mean flow velocity to the acoustical wavespeed in the fluid, will generally be very small ($Ma < 0.01$) in a heavy fluid like water or oil. The isentropic equation of state relates fluid density and pressure:

$$\frac{\partial \rho_f}{\partial p} = \frac{\rho_f}{K_f}, \tag{2.10}$$

where the fluid bulk modulus K_f is related to the velocity of sound c_a in the unconfined fluid by $K_f = \rho_f c_a^2$.

NOTE: The presence of a small volume fraction of gas bubbles in the fluid can cause a dramatic reduction of the wave speed [Junger & Feit 1986]. The extra compressibility and damping due to a homogeneous distribution of small gas bubbles may be accounted for in a reduced complex fluid bulk modulus K_f .

The fluid motion is governed by the linearized Euler equations:

$$\frac{\partial p}{\partial z} = -\rho_f \frac{\partial^2 \xi_z}{\partial t^2}, \quad \frac{1}{r} \frac{\partial p}{\partial \theta} = -\rho_f \frac{\partial^2 \xi_\theta}{\partial t^2}, \quad \frac{\partial p}{\partial r} = -\rho_f \frac{\partial^2 \xi_r}{\partial t^2}, \quad (2.11)$$

Viscosity has been neglected, which is allowed when the shear number $Sh = a_1(\omega/\nu)^{1/2}$ is high ($Sh \gg 1$), where ν is the kinematic viscosity [Tijedman 1975]. Viscous losses may be important for damping of pressure waves in a viscous oil, at high frequencies and in narrow pipes. Damping by viscous friction may be taken into account by introduction of a frequency-dependent, complex fluid bulk modulus: $K_f = Re(K_f)(1 + i\sqrt{2}/Sh)$.

The combination of equations (2.9), (2.10) and (2.11), leads to the homogeneous wave equation for the acoustic pressure p :

$$\frac{1}{c_a^2} \frac{\partial^2 p}{\partial t^2} - \frac{\partial^2 p}{\partial z^2} - \frac{1}{r} \frac{\partial}{\partial r} \left(r \frac{\partial p}{\partial r} \right) - \frac{1}{r^2} \frac{\partial^2 p}{\partial \theta^2} = 0. \quad (2.12)$$

Fluid pressure and wall motion are related through the condition of compatibility at the surfaces of the shell:

$$\xi_r \left(r = a - \frac{h}{2} \right) \approx \xi_r \left(r = a + \frac{h}{2} \right) \approx w_0. \quad (2.13)$$

The equations (2.8) to (2.13) give a complete description of wave propagation in an infinitely long, fluid-filled circular pipe.

2.3 Solution of the equations of motion

The free motion of the coupled system of fluid and shell may be solved from the equations that have been presented above. This section describes the general solution of the equations of motion.

2.3.1 coupled modes

For the investigation of stationary noise and vibration problems it is convenient to solve the wave equations for the fluid-filled pipe in the frequency domain. Hence a Fourier transform with respect to time is performed. This transformation, for example for the acoustic pressure in the fluid, is defined as:

$$p(z,r,\theta,t) = \frac{1}{2\pi} \int_{-\infty}^{\infty} \hat{p}(z,r,\theta,\omega) e^{i\omega t} d\omega . \quad (2.14)$$

All variables of motion must be periodic with respect to the azimuthal angle θ . Hence, they can be expanded in circumferential modes n :

$$\hat{p}(z,r,\theta,\omega) = \sum_{n=-\infty}^{\infty} \hat{p}_n(z,r,\omega) e^{in\theta} . \quad (2.15)$$

The internal and external fluid variables, p and ξ , can be expanded in radial cylinder modes m . For the internal fluid the condition that p^i should be bounded for $r \rightarrow 0$, is fulfilled by an expansion in Bessel functions of the first kind J_n . For the external fluid, the radiation condition $p^e \rightarrow 0$ for $r \rightarrow \infty$, is fulfilled by an expansion in Hankel functions of the second kind H_n [Junger & Feit 1986; Abramowitz & Stegun 1972]:

$$\hat{p}_n^i(z,r,\omega) = \sum_{m=1}^{\infty} \hat{p}_{nm}^i(z,\omega) J_n(\gamma_{nm}^i r) , \quad (2.16)$$

$$\hat{p}_n^e(z,r,\omega) = \sum_{m=1}^{\infty} \hat{p}_{nm}^e(z,\omega) H_n(\gamma_{nm}^e r) ,$$

where γ_{nm} is the radial wavenumber in the internal or external fluids.

For each mode (n,m) the dependence on the axial coordinate will be governed by two waves, propagating in opposite directions, with a complex axial wavenumber k_{nm} , e.g.:

$$\hat{p}_{nm}^i(z,\omega) = P_{nm}^{i+}(\omega) e^{-ik_{nm}^i z} + P_{nm}^{i-}(\omega) e^{ik_{nm}^i z} . \quad (2.17)$$

The amplitudes P_{nm} are complex numbers, to account for phase differences between the waves that are travelling in positive and negative axial direction. Summarizing, the acoustic pressure in the internal fluid can be expressed as:

$$(2.18)$$

$$p^i(z,r,\theta,t) = \frac{1}{2\pi} \int_{-\infty}^{\infty} \sum_{n=-\infty}^{\infty} \sum_{m=1}^{\infty} (P_{nm}^{i+} e^{-ik_{nm}^i z} + P_{nm}^{i-} e^{ik_{nm}^i z}) J_n(\gamma_{nm}^i r) e^{in\theta} e^{i\omega t} d\omega .$$

The other motion variables are expanded similarly. The relationship between the radial wavenumber γ_{nm} and the axial wavenumber k_{nm} can be derived by substitution of equation (2.18) into the wave equation (2.12):

$$(\gamma_{nm}^{i,e})^2 = (k_a^{i,e})^2 - (k_{nm}^{i,e})^2, \quad (2.19)$$

where $k_a = \omega/c_a$ denotes the wavenumber for free acoustic waves in the internal and external fluids and c_a is the sound velocity in the unconfined fluid. The internal and external acoustic pressures are directly related to the radial displacement of the pipe wall, because of the compatibility condition, eq.(2.13). With help of the Euler equations (2.11), the ratio of the amplitudes of the acoustic pressure (P) and the radial wall displacement (W) can be expressed as:

$$\frac{P_{nm}^{i\pm} J_n(\gamma_{nm}^i a_i)}{W_{nm}^\pm} = \rho_f^i a_i \omega^2 \frac{J_n(\gamma_{nm}^i a_i)}{\gamma_{nm}^i a_i J_n'(\gamma_{nm}^i a_i)}, \quad (2.20)$$

where the prime on the Bessel function denotes differentiation with respect to its argument. The ratio of external wall pressure to wall displacement is equivalent, with the Bessel function J_n replaced by the Hankel function H_n , see eq.(2.16).

2.3.2 dispersion equation

The equations of motion per mode (n,m) of a fluid-filled pipe can be expressed in a matrix equation [Leissa 1973; Fuller & Fahy 1982] :

$$\begin{pmatrix} L_{11} & L_{12} & L_{13} \\ L_{21} & L_{22} & L_{23} \\ L_{31} & L_{32} & L_{33} \end{pmatrix} \begin{pmatrix} U_{nm}^\pm \\ V_{nm}^\pm \\ W_{nm}^\pm \end{pmatrix} = \begin{pmatrix} 0 \\ 0 \\ 0 \end{pmatrix}. \quad (2.21)$$

U , V and W are the modal amplitudes of the three orthogonal displacements of the shell (see fig.2.1). The homogeneous matrix equation (2.21) gives non-trivial solutions only if

$$\det([L]) = 0. \quad (2.22)$$

Substitution of the appropriate set of shell equations in eq.(2.21) and equating the determinant to zero leads to the dispersion equation, the wavenumber-frequency relationship for free waves in the fluid-filled pipe. The elements of the matrix $[L]$ are different for different shell theories [Leissa 1973]. The matrices $[L]$ for all shell theories can be expressed as the sum of a matrix $[L_{\text{membrane}}]$, that describes the motion of the shell under membrane stresses only, and a matrix $\beta^2 [L_{\text{bending}}]$, that describes the effect of local bending of the shell, where β^2 is the non-dimensional wall thickness parameter of eq.(2.6):

$$[L] = [L_{\text{membrane}}] + \beta^2 [L_{\text{bending}}] . \quad (2.23)$$

For example Flügge's shell theory leads to the non-dimensional matrix coefficients

$$\begin{aligned} L_{11} &= \Omega^2 - \kappa_{nm}^2 - \frac{1-\nu}{2} n^2 (1 + \beta^2) , \\ L_{22} &= \Omega^2 - \frac{1-\nu}{2} \kappa_{nm}^2 (1 + 3\beta^2) - n^2 , \\ L_{33} &= 1 - \Omega^2 - FL_i + FL_e + \beta^2 \{ 1 - 2n^2 + (\kappa_{nm}^2 + n^2)^2 \} , \\ L_{12} &= L_{21} = \frac{1+\nu}{2} \kappa_{nm} n , \\ L_{13} &= L_{31} = -i \kappa_{nm} \left\{ \nu + \beta^2 \left(\kappa_{nm}^2 - \frac{1-\nu}{2} n^2 \right) \right\} , \\ L_{23} &= L_{32} = in \left(1 + \frac{3-\nu}{2} \beta^2 \kappa_{nm}^2 \right) . \end{aligned} \quad (2.24)$$

Here Ω is the frequency, made non-dimensional with respect to the ring frequency ($\Omega = f/f_{\text{ring}} = \omega a/c_p$, where c_p is the longitudinal wavespeed in a flat plate of the shell material) and κ_{nm} is the wavenumber, made non-dimensional with respect to the middle shell radius a ($\kappa_{nm} = k_{nm} a$). The internal and external fluid-loading in the radial direction lead to the non-dimensional factors $FL_{i,e}$ in the matrix coefficient L_{33} :

$$FL_i = \Omega^2 \frac{\rho_f^i a_i^2}{\rho_s a h} \frac{J_n(\gamma_{nm}^i a_i)}{\gamma_{nm}^i a_i J_n'(\gamma_{nm}^i a_i)} \quad \text{and} \quad FL_e = \Omega^2 \frac{\rho_f^e a_e^2}{\rho_s a h} \frac{H_n(\gamma_{nm}^e a_e)}{\gamma_{nm}^e a_e H_n'(\gamma_{nm}^e a_e)} . \quad (2.25)$$

The presence of the Bessel functions in the matrix $[L]$ causes the dispersion equation (2.22) to have an infinite number of solutions at each frequency.

Solutions to the dispersion equation have been obtained numerically, by expanding the Bessel function in its argument, as described in appendix A.

2.3.3 internal and external fluid loading

For wavelengths that are large compared to the pipe diameter, the Bessel function's argument $\gamma_{nm}^{i,e} a$ will be much smaller than one. Hence the approximate expressions for the Bessel functions with small arguments [Abramowitz & Stegun 1972] can be used to investigate the effect of internal and external fluid loading. For $n=0$ it follows that:

$$\frac{J_0(\gamma_{0m}^i a_i)}{\gamma_{0m}^i a_i J_0'(\gamma_{0m}^i a_i)} \approx -\frac{2}{(\gamma_{0m}^i a_i)^2} \quad \text{and} \quad \frac{H_0(\gamma_{0m}^e a_e)}{\gamma_{0m}^e a_e H_0'(\gamma_{0m}^e a_e)} \approx \ln(\gamma_{0m}^e a_e). \quad (2.26)$$

After substitution of these approximate expressions in the dimensionless parameters $FL_{i,e}$ (eq.2.25) we can see that for $n=0$ the external fluid loading is much smaller than the internal fluid-loading, even when the density of the external fluid is as big as the density of the internal fluid. External loading will be important for gas-filled pipes in an external heavy fluid only. For $n>0$ the approximate fluid loading functions are:

$$\frac{J_n(\gamma_{nm}^i a_i)}{\gamma_{nm}^i a_i J_n'(\gamma_{nm}^i a_i)} \approx \frac{1}{n} \quad \text{and} \quad \frac{H_n(\gamma_{nm}^e a_e)}{\gamma_{nm}^e a_e H_n'(\gamma_{nm}^e a_e)} \approx -\frac{1}{n}. \quad (2.27)$$

Hence for $n \neq 0$ the external fluid loading will be equally important as the internal fluid loading if the densities of the two fluids are comparable. It may be concluded that the external fluid loading can be neglected for fluid-filled pipes in air. Subsequently in this thesis only internal fluid loading will be considered. If necessary external fluid loading can easily be accounted for, by applying eqs.(2.26-27).

2.4 Dispersion curves and approximate equations

The dispersion curves $\kappa(\Omega)$ for wave propagation in a straight fluid-filled cylinder have been analyzed in detail by several authors [Fuller & Fahy 1982; Möser *et al.* 1986; Pavić 1990]. Esparcieux [1986] has validated the theoretical dispersion curves on an oil-filled pipe. Since we are interested in the frequency range where the wavelengths are large compared to the pipe diameter, only the behaviour at low non-dimensional frequencies ($\Omega < 1$) will be considered. The solutions of the dispersion equation represent waves that are either propagating along the pipe axis ($\kappa_{nm} = \pm k_{nm}^r a$), evanescent ($\kappa_{nm} = \pm ik_{nm}^i a$), or propagating with a decaying amplitude ($\kappa_{nm} = \pm k_{nm}^r a \pm ik_{nm}^i a$). As discussed by Fuller [1981,1982], the complex wavenumbers always occur in pairs which together form an attenuated standing wave along the pipe. Evanescent and attenuated standing waves in the positive z -direction will decay along the pipe with a factor $\exp(-k_{nm}^i z)$, hence the amplitude of these waves will be reduced to 0.2% after a distance equal to one pipe diameter ($z=2a$) if $k_{nm}^i a > \pi$. Therefore only solutions of the dispersion equation with $k_{nm}^i a < \pi$ are of interest for the transport of vibro-acoustic energy along straight pipes with a length to diameter ratio greater than one. The evanescent and attenuated standing waves may be important for energy transport in short pipes [Bobrovnikskii 1992]. Evanescent nearfields will also determine the vibratory behaviour of pipes near discontinuities, like supports or

elbows.

Figures 2.2 show the non-dimensional dispersion curves $\kappa(\Omega)$ for a water-filled steel pipe of thickness $h/a=0.05$ at four circumferential mode numbers: (a) $n=0$, (b) $n=1$ (c) $n=2$ (d) $n=3$, resulting from numerical calculations (see appendix A) using the Flügge equations.

2.4.1 $n=0$

At $n=0$ the shell displacement is independent of the circumferential angle θ . Figure 2.2a shows three real dispersion curves. In the low-frequency range ($\Omega < 0.15$) the wave velocity $c=\omega/k$ of these waves is nearly constant. The matching amplitude relationships reveal the character of each wave. The dispersion curve 'F' describes a pressure wave in the fluid. The corresponding wavespeed depends not only on the fluid compressibility but also on the circumferential elasticity of the pipe wall. At the low frequencies that are considered here, it may be approximated by the Korteweg-Lamb equation [Junger & Feit 1986]:

$$c_F \approx \sqrt{\frac{K_f}{\rho_f} \left(1 + 2 \frac{a}{h} \frac{K_f}{E_s}\right)^{-1}} \doteq \check{c}_F. \quad (2.28)$$

In very flexible pipes ($2aK_f/hE_s \gg 1$) the wavespeed will be nearly independent of the fluid compressibility. The description of, for example, the propagation of blood pressure pulses in arteries can therefore be based on an incompressible fluid model [Kuiken 1984]. The dash-dotted line in fig.2.2a shows the approximate dispersion curve of eq.(2.28), which agrees to within 1% with the results of numerical calculation. The curves 'E' and 'T' indicate an axial quasi-longitudinal extensional wave and a torsional waves in the pipe wall. At low frequency the pipe appears to behave as a rod, for which the propagation velocities of the extensional and torsional waves are approximately equal to:

$$c_E \approx \sqrt{\frac{E_s}{\rho_s}} \doteq \check{c}_E \quad \text{and} \quad c_T = \sqrt{\frac{G_s}{\rho_s}}, \quad \text{with} \quad G_s = \frac{E_s}{2(1+\nu)}. \quad (2.29)$$

2.4.2 $n>0$

Only positive mode numbers will be considered, because the dispersion curves for positive and negative circumferential modes n are equal. Figure 2.2b shows one real dispersion curve and two imaginary curves at $n=1$. They represent travelling bending waves and evanescent nearfields. At very low non-dimensional frequencies ($\Omega \leq 0.05$) both the real curve and one of the imaginary curves follow the Euler/Bernoulli beam theory (the solid line in fig.2.2b), for which the wavespeed equals [Cremer *et al.* 1988]:

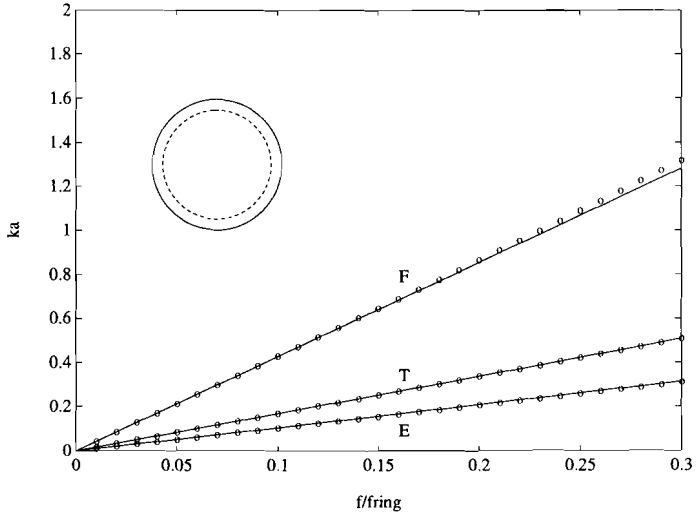


Figure 2.2a: mode shape and non-dimensional dispersion curves for a water-filled steel pipe of thickness $h/a=0.05$ at $n=0$, obtained by numerical calculation (o) and from the equations (2.28) and (2.29) (-).

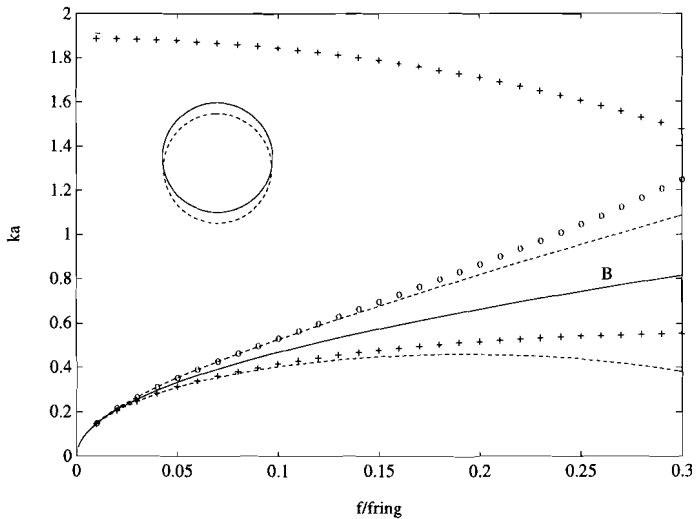


Figure 2.2b: mode shape and non-dimensional dispersion curves for a water-filled steel pipe of thickness $h/a=0.05$ at $n=1$, obtained by numerical calculation: real wavenumbers (o) and imaginary wavenumbers (+) and from eq.(2.31): (--) and eq.(2.30): (-).

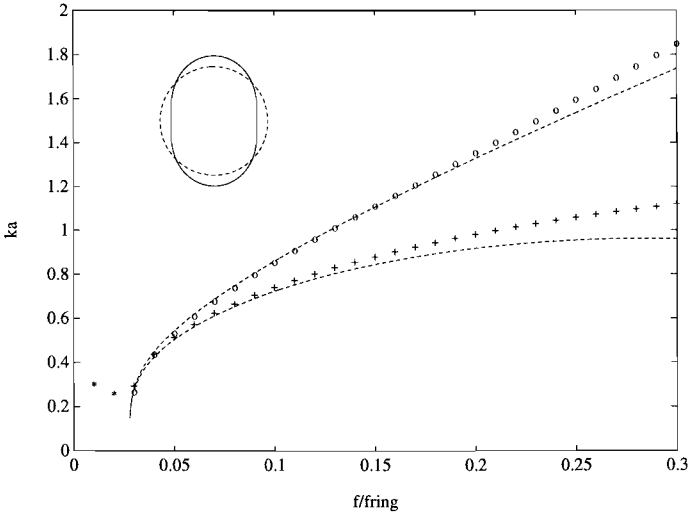


Figure 2.2c: mode shape and non-dimensional dispersion curves for a water-filled steel pipe of thickness $h/a=0.05$ at $n=2$, obtained by numerical calculation: real wavenumbers (o), imaginary wavenumbers ($+$) and imaginary part of complex wavenumbers ($*$) and from eq.(2.31) (--).

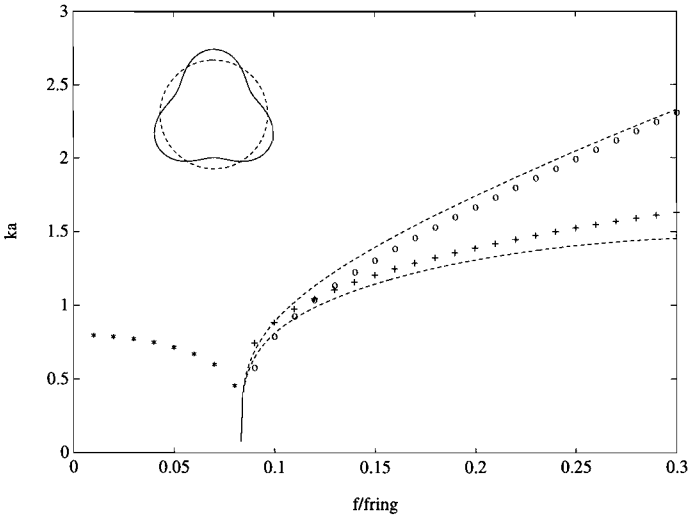


Figure 2.2d: mode shape and non-dimensional dispersion curves for a water-filled steel pipe of thickness $h/a=0.05$ at $n=3$, obtained by numerical calculation: real wavenumbers (o), imaginary wavenumbers ($+$) and imaginary part of complex wavenumbers ($*$) and from eq.(2.31) (--).

$$c_B \approx \sqrt[4]{\frac{E_s I_s \omega^2}{m'}} \doteq \check{c}_B, \quad (2.30)$$

where $I_s \approx \pi a^3 h$ is the second moment of inertia of the pipe cross section and $m' = \rho_s 2\pi a h + \rho_f \pi a_1^2$ the mass per unit length of the pipe plus internal fluid. The divergence of real and imaginary wavenumbers at somewhat higher frequencies is also found in the Timoshenko beam theory [Kurtz 1990]. It is due to the effects of transverse shear and rotatory inertia. An approximate wavenumber equation that describes these effects is given in eq.(2.31) below. The dashed and dash-dotted lines in figure 2.2b show that this approximate equation gives a reasonably accurate description up to $\Omega \approx 0.2$. The upper imaginary wavenumber curve is of importance only for pipes with a length to diameter ratio of order one.

At $n=0$ and $n=1$ the pipe cross-section remains undeformed. Higher circumferential modes display 'lobar' mode shapes. These modes exhibit a so-called 'cut-on' frequency below which no real wavenumber solution exists, see figures 2.2c&d. The cut-on frequencies coincide with the resonance frequencies of the corresponding ring modes, for which n is the number of bending wavelengths that fit on the circumference of the pipe. Möser *et al.* [1986] have shown that the axial phase velocity of the 'lobar' waves at their cut-on frequency is very high, but that the corresponding group velocity is very small. At frequencies below cut-on a complex wavenumber exists, that may be of importance for transport of acoustic energy in short pipes [Bobrovnikskii 1992]. Above cut-on the $n=2$ and $n=3$ dispersion curves show both real and imaginary branches. As for $n=1$, these represent travelling waves and evanescent nearfields respectively.

Approximate expressions may be derived for the real and imaginary dispersion curves. Expanding the dispersion equation for $n>0$ in the small parameters Ω^2 and β^2 leads to the following first-order approximation:

$$\begin{aligned} \kappa_{nm}^2 \approx & \sqrt{\frac{n^2(1+n^2+2n\mu)\Omega^2 - n^4(1-n^2)^2\beta^2}{1-v^2}} \\ & \pm \frac{(\frac{3}{2} + n^2 + 2n\mu)\Omega^2 - n^2(1-n^2)^2\beta^2}{1-v^2} + \dots, \end{aligned} \quad (2.31)$$

where $\mu = \rho_f A_f / \rho_s A_s$ denotes the ratio of the mass per unit length of fluid and pipe. Figures 2.2 shows that the approximate curves are in close agreement with the results of numerical

calculation at low values of Ω . The non-dimensional cut-on frequency $\Omega_{\text{cut-on}}^2$ of the lobar modes is found at $\kappa_{nm}=0$, hence it can approximately be estimated from:

$$\Omega_{\text{cut-on}}^2 \approx \beta^2 \frac{n^2(n^2-1)^2}{1+n^2+2n\mu} . \quad (2.32)$$

which has also been found by Möser [1986] (where eq.4 misses a square) and Pavić [1992].

NOTE: the Donnell-Mushtary equations, that are used by Fuller & Fahy [1982] and Junger & Feit [1986], predict cut-on frequencies for pure propagating $n=1$ and $n=2$ waves that are 30% too low [de Jong & Verheij 1992]. Only at higher circumferential order n do they become comparable with the other sets of equations [Leissa 1973].

2.5 Amplitude ratios

The three-dimensional motion of shell and fluid is described by the ratio of the amplitudes of shell displacement at each wavenumber solution, that can be determined from eq.(2.21) as:

$$\frac{U_{nm}^{\pm}}{W_{nm}^{\pm}} = \frac{L_{12}L_{23} - L_{13}L_{22}}{L_{11}L_{22} - L_{12}L_{21}} \quad \text{and} \quad \frac{V_{nm}^{\pm}}{W_{nm}^{\pm}} = \frac{L_{13}L_{21} - L_{11}L_{23}}{L_{11}L_{22} - L_{12}L_{21}} . \quad (2.33)$$

These ratios are fixed. This implies that each wave may be characterised by one representative displacement component, by preference the component with the largest amplitude. The fixed ratio of internal wall pressure to radial wall displacement, eq.(2.20), implies that the internal acoustic pressure may be determined indirectly from the radial wall displacement. This offers the possibility of a non-intrusive method to measure pressure pulsations in a pipe, which may be very interesting, in particular for situations where aggressive or radio-active fluids are transported and for high pressure pipes.

2.5.1 $n=0$

Since we have neglected fluid-wall friction, the torsional wave motion is independent of the fluid motion. In a pipe with a flexible wall internal pressure pulsations cause a radial 'breathing' motion of the wall. Radial wall displacement is coupled to the axial displacement due to Poisson contraction. The non-dimensional ratio of axial to radial displacement and the low-frequency ($\Omega^2 \ll 1$) approximation of the ratio of internal wall pressure to radial displacement, for the fluid wave and the extensional wave, are given by:

$$\frac{U_{0m}^{\pm}}{W_{0m}^{\pm}} = \pm \frac{i\nu \kappa_{0m}}{\Omega^2 - \kappa_{0m}^2} \quad \text{and} \quad \frac{a_i P_{0m}^{\pm}}{K_f W_{0m}^{\pm}} \approx - \frac{2 \kappa_a^2}{\kappa_a^2 - \kappa_{0m}^2}, \quad (2.34)$$

where $\kappa_a = \omega a / c_a$ is the non-dimensional wavenumber for free waves in the unconfined fluid. The ratio of internal pressure to radial wall displacement appears to be approximately frequency-independent at low frequencies. The ratio of axial to radial wall displacement is inversely proportional to the frequency. Surprisingly, the wall motion due to the fluid wave is predominantly axial at low non-dimensional frequencies [Pavić 1992]. For pipes which are not too flexible κ_F^2 is much greater than Ω^2 so that the radial wall motion starts to dominate the axial motion only when the non-dimensional fluid wavenumber κ_F exceeds the Poisson ratio ν . The consequences of the coupling between the axial waves in the fluid and the shell for pressure and acceleration measurements in fluid-filled pipes will be discussed in chapter 4.

2.5.2 $n > 0$

To lowest order in Ω the displacement ratios for $n > 0$ (eq.2.33) may be approximated as:

$$\frac{U_{nm}^{\pm}}{W_{nm}^{\pm}} \approx \pm i \kappa_{nm} \frac{n^2 - \nu \kappa_{nm}^2}{(n^2 + \kappa_{nm}^2)^2} \quad \text{and} \quad \frac{V_{nm}^{\pm}}{W_{nm}^{\pm}} \approx i n \frac{n^2 + (2 + \nu) \kappa_{nm}^2}{(n^2 + \kappa_{nm}^2)^2} \quad (2.35)$$

Hence the axial shell displacement is smaller than the radial and tangential displacement for $\kappa < 1$. The non-dimensional ratio of the internal fluid wall pressure and the radial wall displacement is approximately equal to:

$$\frac{a_i P_{nm}^{\pm}}{K_f W_{nm}^{\pm}} \approx (a_i/a)^2 \frac{\kappa_a^2}{n}, \quad \text{or:} \quad \frac{P_{nm}^{\pm}}{W_{nm}^{\pm}} \approx \frac{\rho_f a_i \omega^2}{n}. \quad (2.36)$$

At low wavenumbers ($\kappa^2 \ll 1$) this ratio is much smaller than the ratio of wall pressure to radial displacement for $n=0$, see eq.(2.34). From the dimensionful expression in eq.(2.36) it is clear that the wall pressure is due to the inertia of the fluid, where the amount of fluid that is involved in the pipe motion decreases with the mode number n .

2.6 Vibro-acoustic energy flow

All the different waves that have been identified in section 2.4 may contribute to the transport of vibro-acoustic energy along a straight pipe. And for each wave, except for the torsional wave, the energy flow will be distributed over fluid and pipe wall. Non of these

contributions may be neglected a priori. For noise control purposes it is very important to be able to identify the distribution of energy flow. The equations that govern the energy distribution have been given by Fuller & Fahy [1982] and by Pavić [1990;1992]. We will here review these equations and establish approximate equations that will be applied in the measurement method for vibro-acoustic energy flow of chapter 4. Note that convective effects on the vibro-acoustic energy flow are not considered here, although these effects may be important at high flow speeds [Brévert & Fuller 1992].

2.6.1 fluid-borne energy flow

At negligibly small Mach-number, the axial fluid-borne energy flow P_{zf} is obtained by integration of the time averaged acoustic intensity, the product of pressure and particle velocity, over the pipe cross section:

$$P_{zf} = - \int_0^{2\pi} \int_0^{a_i} \langle p \frac{\partial \xi_z}{\partial t} \rangle_t r dr d\theta , \quad (2.37)$$

where $\langle \rangle_t$ denotes time averaging. The axial particle displacement ξ_z is related to the axial gradient of the pressure via the Euler equation (2.11). In the frequency domain this leads to the equation [Verheij 1980]:

$$\hat{P}_{zf}(z, \omega) = \frac{-1}{2\rho_f \omega} \int_0^{2\pi} \int_0^{a_i} \text{Im} \left(\left(\frac{\partial \hat{p}}{\partial z} \right)^* \hat{p} \right) r dr d\theta , \quad (2.38)$$

where $\hat{}$ denotes a Fourier amplitude (eq.2.14), $*$ denotes a complex conjugate and Im denotes the imaginary part of a complex quantity.

2.6.2 structure-borne energy flow

The structure-borne energy flow P_{zs} is defined using the concept of structural intensity [Pavić 1990; Williams 1991]. The axial structural intensity I_{zs} in a thin shell is built up out of five different contributions, that are due to longitudinal extension $\{N_z \dot{u}\}$, tangential shear $\{N_{z\theta} \dot{v}\}$, radial shear $\{Q_z \dot{w}\}$, bending $\{M_z (\partial \dot{w} / \partial z)\}$ and twisting $\{M_{z\theta} (\dot{v} - \partial \dot{w} / \partial \theta) / a\}$, so that the spectrum of the structure-borne energy flow may be obtained from:

(2.39)

$$\hat{P}_{zs}(z, \omega) = \frac{\omega}{2} \int_0^{2\pi} \text{Im} \left(\hat{N}_z^* \hat{u} + \hat{N}_{z\theta}^* \hat{v} + \hat{Q}_z^* \hat{w} + \hat{M}_z^* \frac{\partial \hat{w}}{\partial z} + \hat{M}_{z\theta}^* \frac{1}{a} (\hat{v} - \frac{\partial \hat{w}}{\partial \theta}) \right) a d\theta .$$

The latter three terms are proportional to the shell thickness parameter β^2 and therefore much smaller than the first two for the low-frequency behaviour of practical pipes [Fuller

1981; Williams 1991]. The membrane stresses N_z and $N_{z\theta}$ can be expressed in terms of the shell displacements after integration of eq.(2.3) over the shell thickness, neglecting terms proportional to β^2 :

$$N_z \approx \frac{E_s h}{1-\nu^2} \left(\frac{\partial u}{\partial z} + \nu \left(\frac{1}{a} \frac{\partial v}{\partial \theta} + \frac{w}{a} \right) \right), \quad N_{z\theta} \approx \frac{E_s h}{2(1+\nu)} \left(\frac{\partial v}{\partial z} + \frac{1}{a} \frac{\partial u}{\partial \theta} \right). \quad (2.40)$$

2.6.3 total axial energy flow

The total energy flow in a straight pipe is obtained by summation of the energy flow over the circumferential and axial modes (n,m). Applying the modal expansion (eq.2.18) to the energy flow equations leads to inter-modal products $(n1,m1) \times (n2,m2)$. In the integration over θ the cross-products of circumferential modes $e^{i(n1-n2)\theta}$ disappear when $n1 \neq n2$ [Pavić 1990]. This means that the total axial energy flow can be expanded in circumferential modes:

$$\hat{P}_z = \sum_n \left((\hat{P}_{zf})_n + (\hat{P}_{zs})_n \right). \quad (2.41)$$

The cross-products of axial modes, however, do not disappear. As argued by Pavić [1990] this means that an energy coupling exists between the various axial waves that may coexist at the same circumferential mode number n. The interference of waves that travel at different wavespeed causes the energy flow per wave to be dependent on the axial position. Nevertheless, the total energy flow, i.e. fluid-borne plus structure-borne, is constant along an undamped straight pipe.

No general conclusions can be drawn regarding the distribution of energy over the modes, or over fluid and structure, in a straight fluid-filled pipe of finite length since this distribution depends strongly on the boundary conditions at both ends of the pipe.

2.6.4 approximate energy flow equations

Let us assume that there is just one type of wave present, with a real wavenumber, so that we may neglect the cross-modal coupling. This will help us to obtain equations that relate the energy flow per wave type to the shell displacement. The amplitude ratios are fixed and may be applied to select the characteristic displacement for each wave type, see section 2.5.

At $n=0$ substitution of the amplitude ratio of the displacements (eq.2.34) in the membrane stress equations (2.40) leads to:

$$(N_z)_{0m}^\pm = \mp i \frac{E_s}{1-\nu^2} \frac{h}{a} \frac{\Omega^2}{\kappa_{0m}} U_{0m}^\pm \quad \text{and} \quad (N_{z\theta})_{0m}^\pm = \mp i \frac{E_s}{2(1+\nu)} \frac{h}{a} \kappa_{0m} V_{0m}^\pm. \quad (2.42)$$

Hence the extensional and torsional contributions to the structure-borne energy flow in the three $n=0$ waves (eq.2.28&2.29) are given by:

$$(\hat{P}_{zs})_{F,E}^\pm = \frac{\omega}{2} 2\pi a \operatorname{Im} \left((N_z^*)_{F,E}^\pm U_{F,E}^\pm \right) = \pm A_s \rho_s c_{F,E} \frac{\omega^2}{2} |U_{F,E}^\pm|^2, \quad (2.43)$$

$$(\hat{P}_{zs})_T^\pm = \frac{\omega}{2} 2\pi a \operatorname{Im} \left((N_{z\theta}^*)_T^\pm V_T^\pm \right) = \pm A_s \rho_s c_T \frac{\omega^2}{2} |V_T^\pm|^2,$$

where A_s is the pipe wall cross-sectional area. As expected the pipe behaves as a rod at low frequency: the energy flow equations show a product of a specific impedance $A_s \rho_s c$ and a squared velocity amplitude $\omega^2 |U|^2$ [Cremer *et al.* 1988]. For $(\gamma_{0m} a_i)^2 \ll 1$ the Bessel function J_0 approximately equals 1, so that the equation for fluid-borne energy flow at $n=0$ reduces to the energy flow equation for plane waves in a pipe:

$$(\hat{P}_{zf})_{F,E}^\pm = \pm \frac{A_f}{\rho_f c_{F,E}} \frac{1}{2} |\hat{P}_{F,E}^\pm|^2, \quad (2.44)$$

where A_f is the internal cross-sectional area of the pipe.

At $n>0$ substitution of the modal expansion of the displacement amplitude ratio (eq.2.35) in the equations (2.40) yields:

$$(N_z)_{nm}^\pm \approx E_s \frac{h}{a} \frac{n^2 \kappa_{nm}^2}{(n^2 + \kappa_{nm}^2)^2} W_{nm}^\pm \quad \text{and} \quad (N_{z\theta})_{nm}^\pm \approx \pm E_s \frac{h}{a} \frac{n \kappa_{nm}^3}{(n^2 + \kappa_{nm}^2)^2} W_{nm}^\pm. \quad (2.45)$$

Note that the derivation of these equations should be performed very accurately, because the n^2 -terms in the numerator of U/W and V/W (eq.2.35) cancel after substitution in eq.(2.40) so that the smaller κ^2 -terms determine the result. The extensional and tangential shear contributions to the energy flow then result in:

$$(\hat{P}_{zs})_{\text{ext}}^\pm \approx \pm m' \check{c}_B \frac{n^2 (n^2 - \nu \kappa_{nm}^2) \check{c}_B^3}{(n^2 + \kappa_{nm}^2)^4 c_{nm}^3} \frac{\omega^2}{2} |W_{nm}^\pm|^2, \quad (2.46)$$

$$(\hat{P}_{zs})_{\text{shear}}^\pm \approx \pm m' \check{c}_B \frac{n^2 (n^2 + (2 + \nu) \kappa_{nm}^2) \check{c}_B^3}{(n^2 + \kappa_{nm}^2)^4 c_{nm}^3} \frac{\omega^2}{2} |W_{nm}^\pm|^2,$$

where \check{c}_B is defined by eq.(2.30). For small values of κ ($\kappa^2 \ll n^2$) both contributions are

equal. This supports the conclusion in section 2.4 that the pipe behaves as a simple beam at low frequencies and $n=1$, because in such a beam the contributions of transverse shear forces and bending moments to the energy flow are equal [Cremer *et al.* 1988]. For a pipe the bending stiffness corresponds to the product of the extensional stiffness E_s and the moment of inertia of the cross-section $I_s=\pi a^3 h$. The total structure-borne energy flow at $n>0$ equals:

$$(\hat{P}_{zs})_{nm}^{\pm} = (\hat{P}_{zs})_{ext}^{\pm} + (\hat{P}_{zs})_{shear}^{\pm} \approx \pm 2n^2 m' \check{c}_B \left(\frac{\check{c}_B / c_{nm}}{n^2 + \kappa_{nm}^2} \right)^3 \frac{\omega^2}{2} |W_{nm}^{\pm}|^2. \quad (2.47)$$

Note that the Poisson contraction vanishes in the summation of the two contributions. The fluid-borne energy flow at $n>0$ is of minor importance for $\Omega^2 \ll 1$ [Fuller & Fahy 1982].

2.7 Beam model

In the previous sections we have shown that the low frequency ($\Omega^2 \ll 1$) vibrational behaviour of a fluid-filled cylindrical shell, with a ratio of length L to radius a $L/a \ll 1$, is predominantly determined by the $n=0$ and $n=1$ circumferential modes. In this limit the pipe cross-section remains undeformed, so that the pipe behaves as a fluid-filled beam. In the next chapter we will present a transfer matrix model for the prediction of the dynamic behaviour of three-dimensional pipe systems. This model is based on a quasi one-dimensional description of straight pipes. Here we will derive the equations that govern this beam-like behaviour of a straight pipe from the three-dimensional shell equations.

An undeformed pipe cross-section will have seven degrees of freedom in a Cartesian coordinate system $\{x, y, z\}$, see figure 2.3. The corresponding variables of motion are: three displacements $\{\bar{u}_x, \bar{u}_y, \bar{u}_z\}$ and forces $\{\bar{F}_x, \bar{F}_y, \bar{F}_z\}$, three rotations $\{\bar{\phi}_x, \bar{\phi}_y, \bar{\phi}_z\}$ and moments $\{\bar{M}_x, \bar{M}_y, \bar{M}_z\}$, axial fluid displacement $\{\bar{v}_f\}$ and pressure $\{\bar{p}\}$. The overbar denotes that these variables may be obtained by averaging of the local shell and fluid variables $\{u, v, w, \xi_z\}$ and $\{N_z, N_{z0}, p\}$ over a pipe cross-section, see appendix B. The resulting set of 14 first-order differential equations may be grouped in four independent sets of coupled equations that describe the motion in different planes.

El-Raheb [1981], Lesmez [1989], Tentarelli [1990], Frikha [1992] and Tijsseling [1993] have come to equivalent sets of equations starting from beam theory, but there are some differences. El-Raheb and Frikha neglect the effect of Poisson contraction. Lesmez incorrectly takes a rotary inertia for the fluid into account. Tijsseling adds the effects of

gravity and of friction. The latter is incorporated in terms of the Darcy-Weisbach friction factor. Tentarelli includes frequency-dependent fluid friction, following D'Souza & Oldenburger [1964].

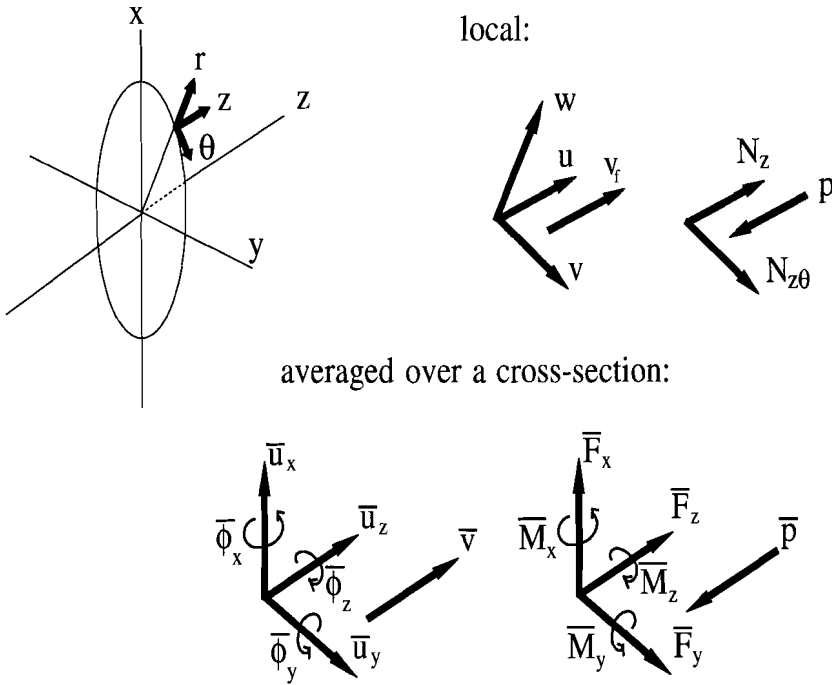


Figure 2.3:

Orientation of local wall displacements and forces and of displacements, rotations, forces and moments in the beam model of a straight pipe.

2.7.1 axial motion of pipe and fluid

The axial motion concerns plane waves in the fluid and quasi-longitudinal extensional waves in the pipe ($n=0$). Pipe and fluid motion are coupled via Poisson contraction of the pipe wall. The four differential equations that describe the axial motion are:

$$\begin{aligned} \frac{d\bar{p}}{dz} &= \rho_f \omega^2 \bar{v}_f, & \frac{d\bar{v}_f}{dz} &= -\frac{1}{K_f} \left(1 + \frac{2aK_f}{hE_s} \right) \bar{p} + 2\nu \frac{a}{a_i} \frac{\bar{F}_z}{E_s A_s}, \\ \frac{d\bar{F}_z}{dz} &= -\rho_s A_s \omega^2 \bar{u}_z, & \frac{d\bar{u}_z}{dz} &= \frac{\bar{F}_z}{E_s A_s} - 2\nu \frac{a}{a_i} \frac{\bar{p} A_f}{E_s A_s}. \end{aligned} \quad (2.48)$$

2.7.2 flexural motion

Flexural motion of the pipe may occur in two perpendicular planes, the xz -plane and the yz -plane, see fig.2.3. The equations that are derived in appendix B are equivalent to the Timoshenko beam bending equations [Cremer *et al.* 1988]. These are for the xz -plane:

$$\begin{aligned} \frac{d\bar{F}_x}{dz} &= -m'\omega^2\bar{u}_x, & \frac{d\bar{u}_x}{dz} &= \frac{\bar{F}_x}{\kappa_s G_s A_s} + \bar{\phi}_y, \\ \frac{d\bar{M}_y}{dz} &= -\bar{F}_x - \rho_s I_s \omega^2 \bar{\phi}_y, & \frac{d\bar{\phi}_y}{dz} &= \frac{\bar{M}_y}{E_s I_s}, \end{aligned} \quad (2.49)$$

where $\kappa_s = 2(1+\nu)/(4+3\nu)$ is the shear coefficient, a shape factor that describes the effective area that is involved in the transverse shear on a pipe cross-section. Note that the internal fluid contributes to the inertia for the transverse motion of the pipe ($m' = \rho_s A_s + \rho_f A_f$) but not to the rotatory inertia I_s . For the yz -plane the equations are similar

$$\begin{aligned} \frac{d\bar{F}_y}{dz} &= -m'\omega^2\bar{u}_y, & \frac{d\bar{u}_y}{dz} &= \frac{\bar{F}_y}{\kappa_s G_s A_s} - \bar{\phi}_x, \\ \frac{d\bar{M}_x}{dz} &= \bar{F}_y - \rho_s I_s \omega^2 \bar{\phi}_x, & \frac{d\bar{\phi}_x}{dz} &= \frac{\bar{M}_x}{E_s I_s}, \end{aligned} \quad (2.50)$$

2.7.3 torsional motion

As we saw in section 2.4 the torsional motion of a straight pipe is not coupled to other degrees of freedom. The equations of torsional motion are:

$$\frac{d\bar{M}_z}{dz} = -\rho_s J_s \omega^2 \bar{\phi}_z, \quad \frac{d\bar{\phi}_z}{dz} = \frac{\bar{M}_z}{G_s J_s}, \quad (2.51)$$

where $J_s \approx 2\pi a^3 h$ is the torsional moment of inertia of the pipe.

2.7.4 review of the limitations for application of the beam model

The quasi one-dimensional model becomes incomplete (but not incorrect) when higher-order 'lobar' modes cut on, above $\Omega_{\text{cut-on}}$ (eq.2.32), or when higher-order acoustic modes occur in the fluid. In a rigid pipe the first acoustic cut-on frequency occurs at $0.293c_a/a_s$ (see e.g. Morse & Ingard [1968]). Further the model is developed under the assumptions that:

- pipe and fluid exhibit a linear elastic behaviour
- pipe wall material and fluid are homogeneous and isotropic

- the wall thickness is small compared to the pipe radius ($\beta^2 \ll 1$)
- the effect of fluid flow is negligible, the Mach-number is low ($Ma \ll 1$)
- viscosity may be neglected, the Shear-number is high ($Sh \gg 1$)
- the length of a straight pipe section is large compared to its diameter ($L/a \gg 1$)

2.8 Conclusion

The equations of motion for a straight fluid-filled circular cylinder have been reviewed in this chapter. Solutions are given in the form of an expansion in an infinite number of circumferential and axial modes (n,m). The dispersion curves for the different modes have been obtained numerically by truncation of the series expansion. Each mode (n,m) may describe two vibrational waves that are travelling along the pipe in positive and negative axial directions. For each wave the amplitudes of the three orthogonal components of displacement of the shell and of the internal fluid pressure and displacement are related through fixed ratios. Therefore the axial vibro-acoustic energy flow in each wave that propagates in the pipe may be expressed in one characteristic wave amplitude.

The frequency range in which the pipe diameter is small compared to the wavelengths is very important for purposes of vibration and noise control in pipe systems. Approximate expressions have been derived that simplify the description of wave propagation in this frequency range ($\Omega < 0.2$). The two lowest circumferential modes (n=0 and n=1) determine the behaviour at these low frequencies. It is shown that in the low-frequency approximation the shell equations for these modes reduce to quasi-one-dimensional beam equations. These approximate equations form a basis for the prediction model and the experimental methods that are proposed in the next chapters.

3. A TRANSFER MATRIX MODEL FOR THE DYNAMIC BEHAVIOUR OF FLUID-FILLED PIPE SYSTEMS

3.1 Introduction

The dynamic behaviour of fluid-filled pipe systems is quite complicated, because it is governed by several coupled waves in fluid and structure. Furthermore, the lay-out of individual pipe systems may differ considerably. A pipe system may consist of any combination of typical components, like straight pipe sections, elbows, pumps, valves, bellows, accumulators, supports, etc. The Transfer Matrix Method (TMM) [Pestel & Leckie 1963] offers an efficient description of the harmonic behaviour of these systems. Each typical component may be described by a transfer matrix, that relates the structural vibrations and fluid pulsations at its outlet port to these at its inlet port. The vibro-acoustic state at each port may be described by a state vector $\{Q\}$ that consists of the single frequency Fourier coefficients of a dynamic quantity (a force, pressure or moment) and a kinematic quantity (a displacement or rotation) for each degree-of-freedom of the port. The transfer matrix $[T_{oi}]$ relates the state vector $\{Q_o\}$ at the outlet port of a component to the state vector $\{Q_i\}$ at its inlet port:

$$\{Q_o\} = [T_{oi}] \{Q_i\} . \quad (3.1)$$

A system transfer matrix may then be assembled by successive multiplication of the transfer matrices of the components of a pipe system. An $N \times N$ system matrix represents a set of N linear equations with $2N$ unknown variables. This set of equations may be solved for the N remaining unknown variables after the introduction of N boundary conditions. The application of the method will have to be repeated at every frequency of interest.

Pipe systems with fluid-structure interaction may also be modelled by the Finite Element Method (FEM), see for example Everstine [1986] and Yeo & Schmid [1989], but these FEM calculations require impressive computer systems. The advantage of the TMM over the FEM is that the size of the matrices that are handled increases much less with the size of the system that is modelled. This may be illustrated by the following example. Let us consider a simple pipe system, consisting of two straight pipes and an elbow, see figure 3.1. This may, for example, represent a system that connects a pump with a pressure vessel. The FEM approximates the deformation of this system as a combination of finite elements that are deformed according to predefined shape functions. The number of nodes M in a FEM model of this system will therefore depend on the highest frequency of

interest, or rather on the ratio of the length of the system to the smallest wavelength of interest. Each node will have N degrees-of-freedom, so that the system matrix will be of size $NM \times NM$. In the TMM a straight pipe may be described as a distributed parameter system with a single $2N \times 2N$ transfer matrix. The size of this transfer matrix is independent of the frequency or of the length of the pipe, because the TMM uses the exact solutions of the wave equations as shape functions. The system transfer matrix is obtained after multiplication of the transfer matrices of the components:

$$[T_{\text{sys}}] = [T_{43}^{\text{pipe}}][T_{32}^{\text{elbow}}][T_{21}^{\text{pipe}}] \quad (3.2)$$

Hence the system matrix of the TMM will remain of size $2N \times 2N$, which is much smaller than the size of the corresponding FEM matrix ($NM \times NM$).

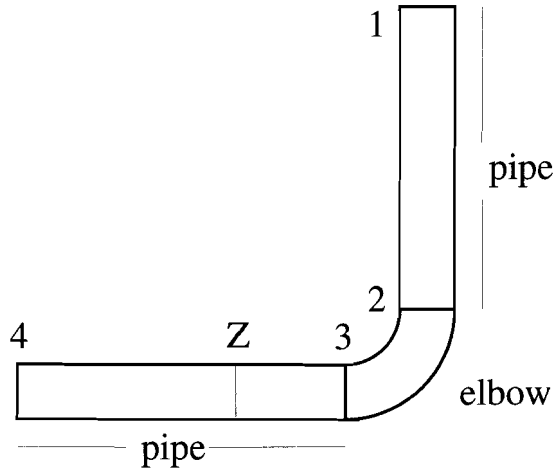


Figure 3.1: a simple pipe system

Note that this simple example overestimates the advantage of the TMM. In the next sections it will be shown that the TMM system matrix may become larger than the single pipe transfer matrix if the system contains supports, branches or vibration and pulsation sources. Moreover, the size of the matrix may have to be increased to prevent round-off errors at higher frequencies and longer systems. Nevertheless the TMM system matrix will remain substantially smaller than a FEM matrix. The TMM model for fluid-filled pipe systems can therefore run on a personal computer (386).

3.2 Solution methods

Once the system matrix has been assembled, the choice of the appropriate solution method depends on the desired result. Two main types of application of the TMM may be distinguished:

- 1) To determine the system resonances and the corresponding mode-shapes, or the response of the system to a given excitation (section 3.2.1).
- 2) To determine the impedance matrix of the system, that can be used to investigate the transmission of vibro-acoustic energy through the system (section 3.2.2).

3.2.1 system response

The determination of the system response for a pipe system that is described by an $N \times N$ transfer matrix requires the introduction of N boundary conditions: one boundary condition per degree-of-freedom at the inlet and at the outlet port. Since each degree-of-freedom (n) is represented by a kinematic (u_n) and a dynamic (F_n) variable, the boundary conditions may be chosen from:

$$u_n = u_n^K, \quad F_n = F_n^K \quad \text{or} \quad F_n - i\omega \sum_m Z_{nm}^K u_m = 0, \quad (3.3)$$

where $(n,m)=1,2,\dots,N/2$, the superscript K refers to an imposed ('known') value and the coefficients Z_{nm}^K form a termination impedance matrix. For example, a clamped boundary is described by $u_n=0$ and a free boundary by $F_n=0$, while a source of pulsations or vibrations at a boundary will cause u_K or F_K to differ from 0.

The boundary conditions may be expressed in matrix form. It is convenient to use a boundary condition matrix $[B]$ to rearrange the state vector so that the known variables (superscript K) are separated from the unknown variables (superscript U):

$$\begin{pmatrix} \{Q_o^K\} \\ \{Q_o^U\} \end{pmatrix} = [B_o][T_{\text{sys}}][B_i] \begin{pmatrix} \{Q_i^K\} \\ \{Q_i^U\} \end{pmatrix} \doteq [T_{oi}] \begin{pmatrix} \{Q_i^K\} \\ \{Q_i^U\} \end{pmatrix}, \quad (3.4)$$

where subscript i refers to the inlet and subscript o to the outlet port of the system. This matrix equation may be rewritten as:

$$\begin{pmatrix} \{Q_o^K\} \\ \{Q_o^U\} \end{pmatrix} = \begin{bmatrix} [T_{oi}^{KK}] & [T_{oi}^{KU}] \\ [T_{oi}^{UK}] & [T_{oi}^{UU}] \end{bmatrix} \begin{pmatrix} \{Q_i^K\} \\ \{Q_i^U\} \end{pmatrix}. \quad (3.5)$$

The unknown variables at the inlet of the pipe system can then be solved from:

$$[T_{oi}^{KU}] \{Q_i^U\} = \{Q_o^K\} - [T_{o,i}^{KK}] \{Q_i^K\}. \quad (3.6)$$

A solution only exists when the sub-matrix $[T_{oi}^{KU}]$ is not singular. $[T_{oi}^{KU}]$ may become singular at the resonance frequencies of an undamped pipe system. Hence the system resonance frequencies are found at zeros of the matrix determinant:

$$\det([T_{oi}^{KU}(f)]) = 0. \quad (3.7)$$

The singularity will be prevented by the introduction of damping in the system transfer matrix. Once the inlet vector has been determined, the outlet vector is determined by substitution in eq.(3.5).

The above method solves all unknown state variables at a single frequency. Frequency response functions are found by repeating the procedure for multiple frequencies. Once the state vectors at the inlet and outlet of the system are known, the motion of each arbitrary point in the pipe system may be obtained by simple matrix multiplication. Let us assume that we are interested in the state vector at position Z in the pipe system of figure 3.1. This state vector is related to the known state vector at the inlet of the system as

$$\{Q_Z\} = [T_{3Z}^{\text{pipe}}] [T_{23}^{\text{elbow}}] [T_{12}^{\text{pipe}}] \{Q_1\}. \quad (3.8)$$

Mode shapes may be determined by repeating this calculation for a selection of positions along the system.

3.2.2 impedance matrix

The system transfer matrix $[T_{\text{sys}}]$ can be rewritten as a system impedance matrix $[Z_{\text{sys}}]$, that relates the generalized force vector $\{F\}$ at both ports to the velocity vector $i\omega\{U\}$:

$$\begin{pmatrix} \{F_i\} \\ \{F_o\} \end{pmatrix} = i\omega [Z_{\text{sys}}] \begin{pmatrix} \{U_i\} \\ \{U_o\} \end{pmatrix} = i\omega \begin{bmatrix} [Z^{ii}] & [Z^{io}] \\ [Z^{oi}] & [Z^{oo}] \end{bmatrix} \begin{pmatrix} \{U_i\} \\ \{U_o\} \end{pmatrix}. \quad (3.9)$$

The sub-matrices $[Z^{ii}]$ and $[Z^{oo}]$ are the driving-point impedance matrices on the inlet and the outlet of the system. The sub-matrices $[Z^{io}]$ and $[Z^{oi}]$ describe the 'blocked' transfer impedances [Verheij 1982]. Like in the system response calculation it is convenient to rearrange the state vectors. Here efforts (F) and displacements (U) are grouped. The reorganized system transfer matrix becomes:

$$\begin{pmatrix} \{F_o\} \\ \{U_o\} \end{pmatrix} = \begin{bmatrix} [T_{oi}^{FF}] & [T_{oi}^{FU}] \\ [T_{oi}^{FU}] & [T_{oi}^{UU}] \end{bmatrix} \begin{pmatrix} \{F_i\} \\ \{U_i\} \end{pmatrix}. \quad (3.10)$$

Hence the impedance matrix can be derived from the transfer matrix as:

$$i\omega [Z_{sys}] = \begin{bmatrix} -[T_{oi}^{UF}]^{-1} [T_{oi}^{UU}] & [T_{oi}^{UF}]^{-1} \\ [T_{oi}^{FU}] - [T_{oi}^{FF}] [T_{oi}^{UF}]^{-1} [T_{oi}^{UU}] & [T_{oi}^{FF}] [T_{oi}^{UF}]^{-1} \end{bmatrix}. \quad (3.11)$$

The sub-matrix $[T_{oi}^{UF}]$ may become singular at frequencies where the system will resonate if all boundaries are clamped.

Impedance methods are widely used to investigate the transmission of vibrational energy in beam and pipe structures [see e.g.: Pinnington & White 1981; Cushieri 1988; Horner & White 1991; Petersson 1993]. It is surprising that the TMM is seldom referred to, although it has been recognized long ago [Pestel & Leckie 1963] recognized as an efficient method to determine the impedance matrix of a system that consist of a cascade of components.

3.3 Transfer matrix model for a fluid-filled pipe system

In section 2.7 a quasi one-dimensional model has been presented for the low-frequency dynamic behaviour of a straight fluid-filled pipe. The vibrational state of a pipe cross-section is described by 14 variables of motion: three orthogonal displacements $\{u_x, u_y, u_z\}$ and forces $\{F_x, F_y, F_z\}$, three rotations $\{\phi_x, \phi_y, \phi_z\}$ and moments $\{M_x, M_y, M_z\}$, axial fluid displacement $\{v\}$ and pressure $\{p\}$ (the overbar is omitted here). These variables are collected in a state vector:

$$\{Q\} = \{ p, F_z, v, u_z, F_x, \phi_y, u_x, M_y, F_y, \phi_x, u_y, M_x, M_z, \phi_z \}. \quad (3.12)$$

The beam model equations describe pressure waves in the fluid and extensional, bending and torsional waves in the pipe. Four groups of coupled variables may be distinguished. Fluid pulsations $\{p, v\}$ and extensional vibrations $\{F_z, u_z\}$ are coupled due to Poisson contraction of the pipe wall. The two orthogonal components of bending waves involve both transverse $\{F_{x,y}, u_{x,y}\}$ and rotational $\{M_{y,x}, \phi_{y,x}\}$ vibrations. The orientation of the state variables has been defined in figure 2.3 (page 30) in a local coordinate system that follows the pipe system. The z-axis of this local coordinate system is always orientated along the pipe axis. If an elbow is present, the y-axis points towards the centre of curvature. The use of a local coordinate system has the advantage that a uniform expression can be applied for the transfer matrices of straight pipes.

3.3.1 solution of the differential equations

The set of first order differential equations that describes wave propagation in a straight fluid-filled pipe (eq.2.48-51), may be represented as:

$$\frac{d}{dz} \begin{pmatrix} \{Q_S\} \\ \{Q_A\} \end{pmatrix} = \begin{pmatrix} [0] & [\tau_{SA}] \\ [\tau_{AS}] & [0] \end{pmatrix} \begin{pmatrix} \{Q_S\} \\ \{Q_A\} \end{pmatrix} \doteq [\tau] \begin{pmatrix} \{Q_S\} \\ \{Q_A\} \end{pmatrix}, \quad (3.13)$$

where $\{Q_S\}$ represents the vector of symmetrical state variables and $\{Q_A\}$ the vector of anti-symmetrical variables [Brown 1967; Tentarelli 1990]. The general solution to this differential equation may be written as a transfer matrix equation:

$$\{Q_o\} = [T] \{Q_i\} = e^{[\tau]L} \{Q_i\}, \quad (3.14)$$

where L denotes the length of the pipe between the inlet and outlet ports.

Any function $f([\tau])$ of a square ($N \times N$) matrix may be expressed exactly by a power series of the matrix $[\tau]$, truncated at order $N-1$ [Pestel & Leckie 1963]:

$$e^{[\tau]L} = C_0 [I] + C_1 [\tau] + C_2 [\tau]^2 + \dots + C_{N-1} [\tau]^{N-1}. \quad (3.15)$$

Here $[I]$ is an $N \times N$ identity matrix. The Cayley-Hamilton Theorem states that the eigenvalues λ_m ($m=1, \dots, N$) have to fulfil the same polynomial equation:

$$e^{\lambda_m L} C_0 + C_1 \lambda_m + C_2 \lambda_m^2 + \dots + C_{N-1} \lambda_m^{N-1}, \quad (3.16)$$

so that the coefficients C_0, C_1, \dots, C_{N-1} may be solved from this set of N linear equations once the eigenvalues of $[\tau]$ have been determined from the characteristic equation

$$\det \left[\begin{pmatrix} -\lambda_m [I] & [\tau_{SA}] \\ [\tau_{AS}] & -\lambda_m [I] \end{pmatrix} \right] = 0. \quad (3.17)$$

The beam model for a straight fluid-filled pipe shows three sets of four coupled equations and one set of two coupled equations. Hence the largest matrix $[\tau]$ is of size 4×4 . The corresponding transfer matrices may be derived analytically.

3.3.2 scaling

Because the solution of the system transfer matrix equation involves a matrix inversion it is useful to scale the equations so that the transfer matrix is non-dimensional and that the matrix coefficients are of the same order of magnitude. This scaling is performed using specific impedances, the driving point impedances for each degree-of-freedom of a semi-infinite straight pipe. These specific impedances are estimated from the approximate

expressions for the wave velocities, eq.(2.28-2.30). The effort components of the state vector are scaled with ωZ_s , so that they have a dimension of length like the displacements. Denoting the scaled variables by a tilde (\sim) the scaling relationships are given by:

$$\begin{aligned} p &= \rho_f \check{c}_F \omega \check{p} , \quad F_z = A_s \rho_s \check{c}_E \omega \check{F}_z , \quad v = \check{v} , \quad u_z = \check{u}_z , \\ F_x &= m' \check{c}_B \omega \check{F}_x , \quad \phi_y = (\omega / \check{c}_B) \check{\phi}_y , \quad u_x = \check{u}_x , \quad M_y = m' \check{c}_B^2 \check{M}_y , \\ F_y &= m' \check{c}_B \omega \check{F}_y , \quad \phi_x = (\omega / \check{c}_B) \check{\phi}_x , \quad u_y = \check{u}_y , \quad M_x = m' \check{c}_B^2 \check{M}_x , \\ M_z &= A_s \rho_s c_T a \omega \check{M}_z , \quad \phi_z = \check{\phi}_z / a . \end{aligned} \quad (3.18)$$

When modelling a pipe system that consists of more than one type of pipe (defined by inner and outer diameters and material properties), we will select a reference for the scaling and adapt the transfer matrix of the pipes with different geometrical or material properties to this scaling.

3.3.3 straight fluid-filled pipes

The differential equations of the quasi one-dimensional model for the dynamic behaviour of a straight pipe (section 2.7) may be solved analytically using the method that has been presented in section 3.3.1. Here the transfer matrix for a pipe of length L will be derived per group of coupled degrees-of-freedom, using the scaling of eq.(3.18).

axial transmission via fluid and pipe wall

The equations (2.48) lead to the characteristic equation:

$$\lambda_m^4 + \lambda_m^2 (\check{k}_F^2 + \check{k}_E^2) + \check{k}_F^2 \check{k}_E^2 (1 - \sigma \check{v}^2) = 0 . \quad (3.19)$$

with the definitions

$$\check{v} \doteq 2v \frac{a}{a_1} \quad \text{and} \quad \sigma \doteq \frac{A_f K_f}{A_s E_s} \left(1 + 2 \frac{a}{h} \frac{K_f}{E_s} \right)^{-1} = \frac{A_f \rho_f \check{c}_F^2}{A_s \rho_s \check{c}_E^2} . \quad (3.20)$$

The approximate wavenumbers (\check{k}) appear in this equation because the approximate wave velocities are used in the scaling (see eq.(3.18)). As expected, the eigenvalues are nearly equal to $\lambda_{1,2} \doteq \pm i k_F \approx \pm i \check{k}_F$ and $\lambda_{3,4} \doteq \pm i k_E \approx \pm i \check{k}_E$. The deviation from these approximate solutions is due to the Poisson term $\sigma \check{v}^2$. With a scaled state vector $\{\check{p}, \check{F}_z, \check{v}, \check{u}_z\}$ the analytical expression of the non-dimensional transfer matrix for axial extensional and pressure waves $[\check{T}_z]$ is given by:

$$(3.21)$$

$$\begin{bmatrix} C_0 - \check{k}_F^2 C_2 & \check{v} \check{k}_F \check{k}_E C_2 & \check{k}_F (C_1 - \check{k}_F^2 C_3) & -\check{v} \check{k}_F \check{k}_E^2 C_3 \\ \sigma \check{v} \check{k}_F \check{k}_E C_2 & C_0 - \check{k}_E^2 C_2 & \sigma \check{v} \check{k}_F^2 \check{k}_E C_3 & -\check{k}_E (C_1 - \check{k}_E^2 C_3) \\ -\check{k}_F (C_1 - (\check{k}_F^2 + \sigma \check{v}^2 \check{k}_E^2) C_3) & \check{v} \check{k}_E (C_1 - (\check{k}_F^2 + \check{k}_E^2) C_3) & C_0 - \check{k}_F^2 C_2 & -\check{v} \check{k}_E^2 C_2 \\ -\sigma \check{v} \check{k}_F (C_1 - (\check{k}_F^2 + \check{k}_E^2) C_3) & \check{k}_E (C_1 - (\check{k}_E^2 + \sigma \check{v}^2 \check{k}_F^2) C_3) & -\sigma \check{v} \check{k}_F^2 C_2 & C_0 - \check{k}_E^2 C_2 \end{bmatrix}$$

with the coefficients, based on the exact solutions (k_F, k_E) of equation (3.19):

$$(3.22)$$

$$\begin{pmatrix} C_0 \\ C_2 \\ C_1 \\ C_3 \end{pmatrix} = \frac{1}{k_E^2 - k_F^2} \begin{bmatrix} k_E^2 & -k_F^2 & 0 & 0 \\ 1 & -1 & 0 & 0 \\ 0 & 0 & k_E^2 & -k_F^2 \\ 0 & 0 & 1 & -1 \end{bmatrix} \begin{pmatrix} \cos(k_F L) \\ \cos(k_E L) \\ \sin(k_F L)/k_F \\ \sin(k_E L)/k_E \end{pmatrix}$$

transmission via flexural motion

Both the equations (2.49) and (2.50) lead to the characteristic equation for flexural motion:

$$(3.23)$$

$$\lambda_m^4 + \lambda_m^2 \check{k}_B^2 (\chi + \zeta) - \check{k}_B^4 (1 - \chi \zeta) = 0 .$$

with the definitions

$$(3.24)$$

$$\chi \doteq \frac{E_s I_s}{\kappa_s G_s A_s} \check{k}_B^2 \quad \text{and} \quad \zeta \doteq \frac{\rho_s I_s}{m'} \check{k}_B^2 \doteq \frac{\rho_s I_s}{\rho_s A_s + \rho_f A_f} \check{k}_B^2 .$$

At low frequencies ($\zeta \ll 1$; $\chi \ll 1$) the eigenvalues will agree with the Euler-Bernoulli beam theory, describing travelling waves $\lambda_{1,2} \doteq \pm i k_B \approx \pm i \check{k}_B$ and evanescent nearfields $\lambda_{3,4} \doteq \pm k_N \approx \pm \check{k}_B$. With a scaled state vector $\{\tilde{F}_x, \tilde{\phi}_y, \tilde{u}_x, \tilde{M}_y\}$ the non-dimensional transfer matrix for flexural motion in the xz -plane $[\tilde{T}_{xz}]$ is given by

(3.25)

$$\left[\begin{array}{cccc} C_0 - \chi \check{k}_B^2 C_2 & -\check{k}_B^2 C_2 & -\check{k}_B(C_1 - \chi \check{k}_B^2 C_3) & -\check{k}_B^3 C_3 \\ -\check{k}_B^2 C_2 & C_0 - \zeta \check{k}_B^2 C_2 & \check{k}_B^3 C_3 & \check{k}_B(C_1 - \zeta \check{k}_B^2 C_3) \\ \check{k}_B(\chi C_1 - (1 + \chi^2) \check{k}_B^2 C_3) & \check{k}_B(C_1 - (\chi + \zeta) \check{k}_B^2 C_3) & C_0 - \chi \check{k}_B^2 C_2 & \check{k}_B^2 C_2 \\ -\check{k}_B(C_1 - (\chi + \zeta) \check{k}_B^2 C_3) & -\check{k}_B(\zeta C_1 - (1 + \zeta^2) \check{k}_B^2 C_3) & \check{k}_B^2 C_2 & C_0 - \zeta \check{k}_B^2 C_2 \end{array} \right]$$

and, with a scaled state vector $\{\tilde{F}_y, \tilde{\phi}_x, \tilde{u}_y, \tilde{M}_x\}$, the matrix for flexural motion in the yz -plane $[\tilde{T}_{yz}]$ equals

(3.26)

$$\left[\begin{array}{cccc} C_0 - \chi \check{k}_B^2 C_2 & \check{k}_B^2 C_2 & -\check{k}_B(C_1 - \chi \check{k}_B^2 C_3) & \check{k}_B^3 C_3 \\ \check{k}_B^2 C_2 & C_0 - \zeta \check{k}_B^2 C_2 & -\check{k}_B^3 C_3 & \check{k}_B(C_1 - \zeta \check{k}_B^2 C_3) \\ \check{k}_B(\chi C_1 - (1 + \chi^2) \check{k}_B^2 C_3) & -\check{k}_B(C_1 - (\chi + \zeta) \check{k}_B^2 C_3) & C_0 - \chi \check{k}_B^2 C_2 & -\check{k}_B^2 C_2 \\ \check{k}_B(C_1 - (\chi + \zeta) \check{k}_B^2 C_3) & -\check{k}_B(\zeta C_1 - (1 + \zeta^2) \check{k}_B^2 C_3) & -\check{k}_B^2 C_2 & C_0 - \zeta \check{k}_B^2 C_2 \end{array} \right]$$

Both matrices share the same coefficients:

$$\begin{pmatrix} C_0 \\ C_2 \\ C_1 \\ C_3 \end{pmatrix} = \frac{1}{k_N^2 + k_B^2} \begin{bmatrix} k_N^2 & k_B^2 & 0 & 0 \\ -1 & 1 & 0 & 0 \\ 0 & 0 & k_N^2 & k_B^2 \\ 0 & 0 & -1 & 1 \end{bmatrix} \begin{pmatrix} \cos(k_B L) \\ \cosh(k_N L) \\ \sin(k_B L)/k_B \\ \sinh(k_N L)/k_N \end{pmatrix}. \quad (3.27)$$

All coefficients of the matrices for flexural motion contain a combination of a cos- or sin-function with a cosh- or sinh-function to describe the combined effect of propagating waves and evanescent nearfields, respectively. For longer pipes and higher frequencies the argument $k_N L$ will become large. Physically, the effect of nearfields on the vibro-acoustic transfer will decrease with increasing $k_N L$. However, the cosh- and sinh-functions in the transfer matrix may become very large, so that the information in the cos- and sin-functions may get lost due to numerical round-off errors. This problem can be overcome by dividing the straight pipe into shorter pipes, for which $k_N L$ is sufficiently small to avoid numerical errors. These shorter pipes have to be treated as sub-systems that are solved in parallel, instead of multiplying them in series, see section 3.5.

transmission via torsional motion

The two equations (2.51) exhibit eigenvalues $\lambda_{1,2} = \pm ik_T$. The scaled state vector for torsion is $\{\tilde{M}_z, \tilde{\phi}_z\}$. The corresponding non-dimensional transfer matrix is given by:

$$[\tilde{T}_\phi] = \begin{bmatrix} \cos(k_T L) & -\sin(k_T L) \\ \sin(k_T L) & \cos(k_T L) \end{bmatrix}. \quad (3.28)$$

complete transfer matrix of a straight pipe

The sub-matrices that have been given above may be combined into a complete transfer matrix, that relates the state vectors (eq.3.12) at the inlet and outlet ports of a straight pipe:

$$[\tilde{T}_{\text{pipe}}] = \begin{bmatrix} [\tilde{T}_z] & [0] & [0] & [0] \\ [0] & [\tilde{T}_{xz}] & [0] & [0] \\ [0] & [0] & [\tilde{T}_{yz}] & [0] \\ [0] & [0] & [0] & [\tilde{T}_\phi] \end{bmatrix}. \quad (3.29)$$

3.3.4 curved pipes or elbows

In analogy to the modelling of wave propagation in straight pipes (Chapter 2), shell theory may be applied to determine the equations of motion of a uniformly curved pipe of circular cross-section [El-Raheb & Wagner 1985; Whatham 1986]. However, no analytical solutions to these equations are available. The solutions of toroidal shell equations cannot be separated in independent circumferential modes [Firth 1981; Firth & Fahy 1984]. Due to this modal coupling, pressure pulsations and structural vibrations exhibit a strong interaction in a curved pipe. Pressure waves ($n=0$) in a curved pipe will, for example, generate extensional waves ($n=0$) and bending waves ($n=1$). Bending waves will be coupled to $n>1$ lobar waves. This 'junction coupling' will even be greater if the cross-section of the curved pipe is not circular. The Bourdon gauge, consisting of a flattened toroidal tube, relies on this principle to measure internal fluid pressure [Tentarelli 1990]. Here we will restrict ourselves to the modelling of uniformly curved, fluid-filled circular pipes. The TMM requires a simplified model for the beam-like behaviour of curved pipes, that accounts for the coupling effects.

Two totally different approaches have been reported. The *discrete* model represents the curved pipe as a series of small angle bends and short straight pipes [Wilkinson 1978; Lesmez 1989]. The *continuous* model is based on a set of first order differential equations for the uniformly curved pipe [Davidson & Smith 1969; Davidson & Samsury 1972; El-Raheb 1981; Tentarelli 1990].

These beam-type models do not describe higher-order ($n > 1$) waves in the pipe wall. However, the coupling to lobar deformation of the wall causes the curved pipe to be more flexible to bending than a comparable length of straight pipe. Both discrete and continuous beam models can approximately account for this effect by dividing the bending stiffness $E_s I_s$ of the curved pipe by a *flexibility factor* ff [Von Kármán 1911, Kellogg Company 1964]. In this approximation the lobar deformation of the elbow is assumed to be locally reacting. For an elbow with angle γ (radians), radius of curvature R , mean radius a and wall thickness h the flexibility factor equals $ff = 1.65a^2/hR$, provided that $R/a > 1.7$, that $R\gamma > 2a$ and that there are no flanges or similar stiffeners within a distance equal to a pipe radius from either end of the elbow. The same flexibility factor should be used for in-plane and out-of-plane bending of the elbow. Flexibility factors for elbows with flanges are given in an ASME code [ASME 1992]. The elbow flexibility is especially important for the response of systems where the elbows are not short compared to the length of the straight pipes [Everstine 1986].

The state vectors in the TMM are defined in local coordinates, that are connected with the orientation of the pipe system components. The local z -axis is orientated along the pipe axis and the local y -axis points towards the centre of curvature of the elbow. Therefore the description of an elbow or bend requires a local coordinate transformation. Generally, this transformation involves two consecutive rotations, α and γ , see figure 3.2. The transfer matrix for an elbow may therefore be expressed as a matrix product $[T_\gamma][T_\alpha]$.

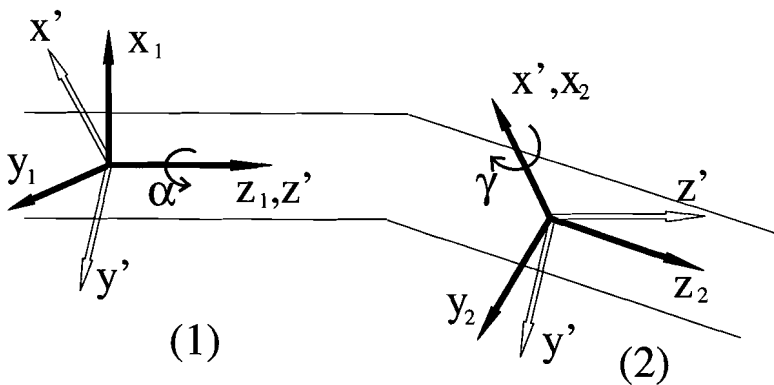


Figure 3.2: rotation of the local coordinate system at a bend point: (1) rotation over angle α around the z -axis; (2) rotation over angle γ around the new x -axis.

The matrix $[T_\alpha]$ performs the rotation over angle α around the z-axis, so that the y-axis points to the centre of curvature:

$$[T_\alpha] = \begin{bmatrix} 1 & 0 & 0 & 0 & 0 & 0 & 0 & 0 & 0 & 0 & 0 & 0 & 0 & 0 \\ 0 & 1 & 0 & 0 & 0 & 0 & 0 & 0 & 0 & 0 & 0 & 0 & 0 & 0 \\ 0 & 0 & 1 & 0 & 0 & 0 & 0 & 0 & 0 & 0 & 0 & 0 & 0 & 0 \\ 0 & 0 & 0 & 1 & 0 & 0 & 0 & 0 & 0 & 0 & 0 & 0 & 0 & 0 \\ 0 & 0 & 0 & 0 & C_\alpha & 0 & 0 & 0 & S_\alpha & 0 & 0 & 0 & 0 & 0 \\ 0 & 0 & 0 & 0 & 0 & C_\alpha & 0 & 0 & 0 & -S_\alpha & 0 & 0 & 0 & 0 \\ 0 & 0 & 0 & 0 & 0 & 0 & C_\alpha & 0 & 0 & 0 & S_\alpha & 0 & 0 & 0 \\ 0 & 0 & 0 & 0 & 0 & 0 & 0 & C_\alpha & 0 & 0 & 0 & -S_\alpha & 0 & 0 \\ 0 & 0 & 0 & 0 & -S_\alpha & 0 & 0 & 0 & C_\alpha & 0 & 0 & 0 & 0 & 0 \\ 0 & 0 & 0 & 0 & 0 & S_\alpha & 0 & 0 & 0 & C_\alpha & 0 & 0 & 0 & 0 \\ 0 & 0 & 0 & 0 & 0 & 0 & -S_\alpha & 0 & 0 & 0 & C_\alpha & 0 & 0 & 0 \\ 0 & 0 & 0 & 0 & 0 & 0 & 0 & S_\alpha & 0 & 0 & 0 & C_\alpha & 0 & 0 \\ 0 & 0 & 0 & 0 & 0 & 0 & 0 & 0 & 0 & 0 & 0 & 0 & 1 & 0 \\ 0 & 0 & 0 & 0 & 0 & 0 & 0 & 0 & 0 & 0 & 0 & 0 & 0 & 1 \end{bmatrix} \quad (3.30)$$

with $C_\alpha = \cos(\alpha)$ and $S_\alpha = \sin(\alpha)$. Note that this is a dimensional transfer matrix.

Both the discrete and the continuous model for the elbow transfer matrix $[T_\gamma]$ describe the junction coupling and the rotation over the angle γ that aligns the new z-axis with the pipe axis.

discrete model

In the discrete model a curved pipe is approximated by a series of M bend points connected by $M+1$ straight pipes, see figure 3.3. M should be chosen so that the length l_m of the straight pipes is small compared with the shortest wavelength of interest. The model is only valid for $l_m/a > 1$, so that a further discretization is useless. The straight pipes are described by the transfer matrix of section 3.3.3. The bending stiffness $E_s I_s$ is divided by the appropriate flexibility factor ff . The inertia and elasticity of pipe and fluid at the bend points are neglected. The transfer matrix for the bend points is derived from the equations of continuity and equilibrium of forces and results in (e.g. Lesmez [1989]):

(3.31)

$$[T_\gamma] = \begin{bmatrix} 1 & 0 & 0 & 0 & 0 & 0 & 0 & 0 & 0 & 0 & 0 & 0 & 0 & 0 \\ A_f(1-C_\gamma) & C_\gamma & 0 & 0 & 0 & 0 & 0 & 0 & S_\gamma & 0 & 0 & 0 & 0 & 0 \\ 0 & 0 & 1 & (C_\gamma-1) & 0 & 0 & 0 & 0 & 0 & 0 & S_\gamma & 0 & 0 & 0 \\ 0 & 0 & 0 & C_\gamma & 0 & 0 & 0 & 0 & 0 & 0 & S_\gamma & 0 & 0 & 0 \\ 0 & 0 & 0 & 0 & 1 & 0 & 0 & 0 & 0 & 0 & 0 & 0 & 0 & 0 \\ 0 & 0 & 0 & 0 & 0 & C_\gamma & 0 & 0 & 0 & 0 & 0 & 0 & 0 & -S_\gamma \\ 0 & 0 & 0 & 0 & 0 & 0 & 1 & 0 & 0 & 0 & 0 & 0 & 0 & 0 \\ 0 & 0 & 0 & 0 & 0 & 0 & 0 & C_\gamma & 0 & 0 & 0 & 0 & -S_\gamma & 0 \\ A_f S_\gamma & -S_\gamma & 0 & 0 & 0 & 0 & 0 & 0 & C_\gamma & 0 & 0 & 0 & 0 & 0 \\ 0 & 0 & 0 & 0 & 0 & 0 & 0 & 0 & 0 & 1 & 0 & 0 & 0 & 0 \\ 0 & 0 & 0 & -S_\gamma & 0 & 0 & 0 & 0 & 0 & 0 & C_\gamma & 0 & 0 & 0 \\ 0 & 0 & 0 & 0 & 0 & 0 & 0 & 0 & 0 & 0 & 0 & 1 & 0 & 0 \\ 0 & 0 & 0 & 0 & 0 & 0 & 0 & S_\gamma & 0 & 0 & 0 & 0 & C_\gamma & 0 \\ 0 & 0 & 0 & 0 & 0 & S_\gamma & 0 & 0 & 0 & 0 & 0 & 0 & 0 & C_\gamma \end{bmatrix}$$

with $C_\gamma = \cos(\gamma)$ and $S_\gamma = \sin(\gamma)$. Like $[T_\alpha]$ (eq.3.30) this is a dimensional transfer matrix.

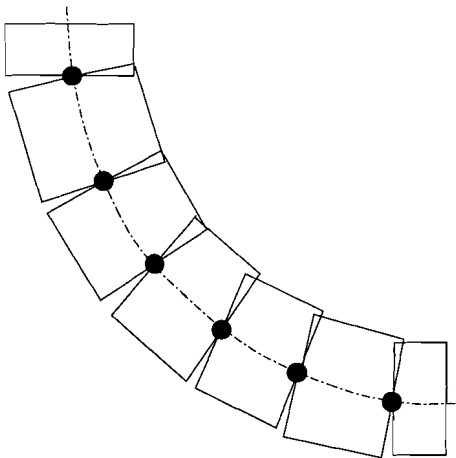


Figure 3.3: discrete model of a uniformly curved pipe

continuous model

Davidson & Smith [1969] and Davidson & Samsury [1972] have developed a set of first-order differential equations that describe the beam-type, coupled vibration of a uniformly curved, liquid-filled pipe. This low-frequency approximation is valid for curved pipes with $a/R \ll 1$. Tentarelli [1990] extended the model with the effect of Poisson contraction. As in the discrete model, the bending stiffness is modified by the appropriate flexibility factor ff . The orientation of the state variables is given in figure 2.3, with the y-axis pointing to the centre of curvature and the z-axis replaced by a curved $R\gamma$ -axis. The following set of equations for in-plane motion may be obtained:

$$\begin{aligned} \frac{dp}{Rd\gamma} &= \rho_f \omega^2 v, & \frac{dv}{Rd\gamma} &= -\frac{p}{K_f} \left(1 + \frac{2aK_f}{hE_s}\right) + 2v \frac{a}{a_i} \frac{F_z}{E_s A_s} + \frac{u_y}{R}, \\ \frac{dF_z}{Rd\gamma} &= -\rho_s A_s \omega^2 u_z + \frac{F_y}{R}, & \frac{du_z}{Rd\gamma} &= \frac{F_z}{E_s A_s} - 2v \frac{a}{a_i} \frac{p A_f}{E_s A_s} + \frac{u_y}{R}, \\ \frac{dF_y}{Rd\gamma} &= -m' \omega^2 u_y - \frac{F_z}{R} + \frac{A_f p}{R}, & \frac{du_y}{Rd\gamma} &= \frac{F_y}{\kappa_s G_s A_s} - \phi_x - \frac{u_z}{R}, \\ & & \frac{dM_x}{Rd\gamma} &= -\rho_s I_s \omega^2 \phi_x + F_y, & \frac{d\phi_x}{Rd\gamma} &= \frac{M_x}{E_s I_s / ff} \end{aligned} \quad (3.32)$$

and the equations for out-of-plane motion are given by:

$$\begin{aligned} \frac{dF_x}{Rd\gamma} &= -m' \omega^2 u_x, & \frac{du_x}{Rd\gamma} &= \frac{F_x}{\kappa_s G_s A_s} + \phi_y, \\ \frac{dM_y}{Rd\gamma} &= -\rho_s I_s \omega^2 \phi_y - F_x - \frac{M_z}{R}, & \frac{d\phi_y}{Rd\gamma} &= \frac{M_y}{E_s I_s / ff} - \frac{\phi_z}{R}, \\ \frac{dM_z}{Rd\gamma} &= -\rho_s J_s \omega^2 \phi_z + \frac{M_y}{R}, & \frac{d\phi_z}{Rd\gamma} &= \frac{M_z}{G_s J_s} + \frac{\phi_y}{R}. \end{aligned} \quad (3.33)$$

These equations differ from the straight pipe equations (2.48-51) in the terms proportional to $1/R$, that describe the junction coupling. Due to these coupling terms the equations of motion cannot be separated further than in a set of eight coupled in-plane equations (3.32) and a set of six coupled out-of-plane equations (3.33). The procedure that has been given in section 3.3.1 may be applied to solve the equations. No analytical solutions have been obtained, but the eigenvalues and the non-dimensional transfer matrix $[T_\gamma]$ may be readily derived numerically.

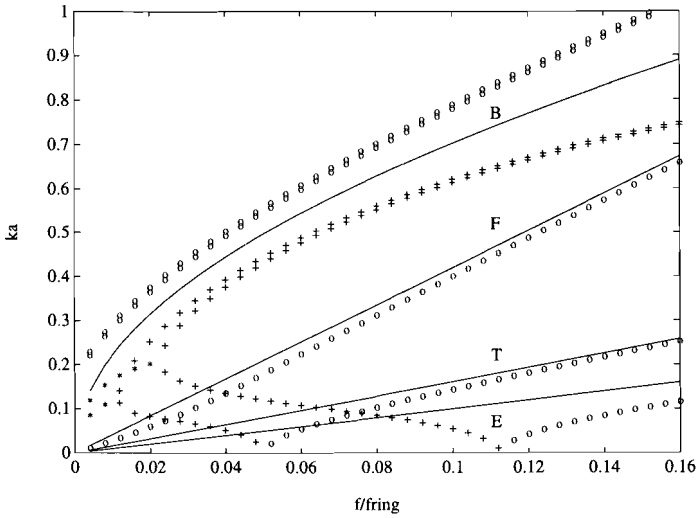


Figure 3.4: non-dimensional dispersion curves for waves in a uniformly curved, water-filled steel pipe of thickness $h/a=0.05$ and curvature $R/a=6$. The markers denote real (o), imaginary (+) and complex (*) wavenumbers. The lines give the curves for fluid (F), extensional (E), torsional (T) and bending (B) waves in a straight pipe of the same thickness and flexibility ($ff=5.5$).

As an illustration of the effect of curvature on the wave propagation in a uniformly curved pipe, figure 3.4 shows the non-dimensional dispersion curves $\kappa(\Omega)$ for a pipe with $h/a=0.05$ and $R/a=6$. From comparison with the waves in a straight pipe of the same dimensions (the solid curves in fig.3.4) it can be seen that the fluid waves are hardly influenced. Torsional and extensional waves in a curved pipe appear to exhibit a cut-on frequency, below which they are evanescent. The solid curve (B) describes the Bernoulli-bending of a straight pipe with the bending stiffness divided by the flexibility factor for the curved pipe. The bending waves in the curved pipe propagate at a somewhat lower velocity. A small difference in wavenumber for in-plane and out-of-plane bending waves, that can be seen as nearly coinciding markers ('o,+') in figure 3.4, is caused by a different coupling to other waves (e.g. the out-of-plane bending is not coupled to longitudinal waves as is the in-plane bending).

comparison

The discrete and continuous models give two different approximations for the three-dimensional equations of motion of the elbow. The continuous model is based upon the assumption that $a/R \ll 1$. The discrete model may also be used for short radius elbows, provided that the elbow length is small compared to the shortest straight pipe bending wavelength of interest.

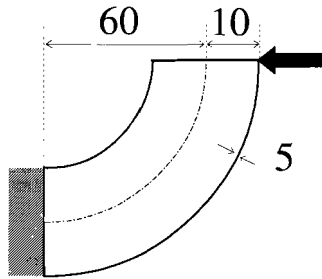


Figure 3.5: a water-filled steel 90° elbow ($E_s=2.1 \cdot 10^{11}(1+0.01i) \text{ N/m}^2$, $\rho_s=7800 \text{ kg/m}^3$, $\nu=0.3$, $K_f=2.15 \cdot 10^9 \text{ N/m}^2$, $\rho_f=1000 \text{ kg/m}^3$). The sizes are in mm. At one end the elbow is clamped and closed, the other end is open and driven by an in-plane transverse force.

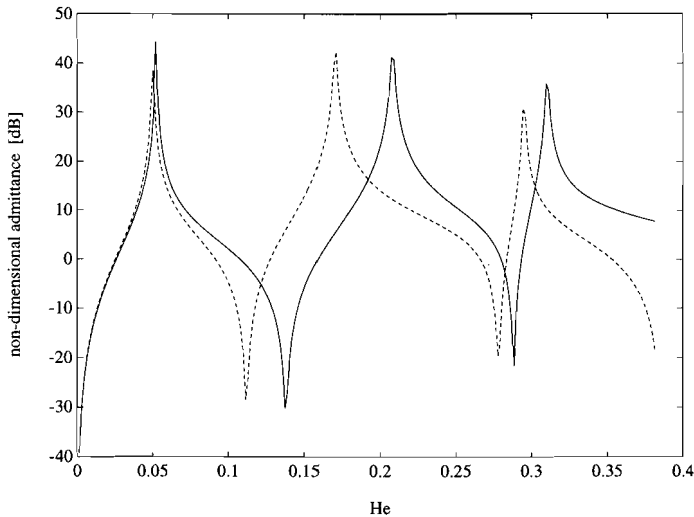


Figure 3.6: non-dimensional input admittance (\bar{u}_y/\bar{F}_y) for transverse vibration of the elbow of figure 3.5, for the continuous (solid line) and discrete (dashed line) models, as a function of the Helmholtz number $He=fL/c_F$.

The models are compared by calculating the response of a fluid-filled elbow to in-plane, transverse excitation. Geometry and material parameters are given in figure 3.5. Both models use the same flexibility factor $ff=1.65a^2/hR\approx 5.5$. Figure 3.6 shows the resulting spectrum of the non-dimensional input admittance ($Z_{Bu,y}/F_y$) at the free end. It appears that the continuous model (solid line) predicts that the elbow is stiffer than the discrete model (dashed line) predicts. Note that the height of the peaks is determined by the finite resolution in the frequency (Helmholtz number), so that no conclusions may be drawn from the comparison of peak heights. Doubling the number of bending points (to 12) did not change the impedance curve for the discrete model. The choice of model for an elbow will have to depend on the specific geometry of the elbow. In practice elbows often are of short radius ($a/R=1/3$ is very common). Short radius elbows can probably better be modelled by the discrete model than by the continuous model, that assumes that $a/R\ll 1$. However, the difference between the models is not very important if the length of the elbows is small compared with the straight pipe lengths in the system. TMM calculations, with both models, have been compared with three-dimensional FEM calculations (using ANSYS) for an empty pipe system consisting of a 90° elbow ($a/R\approx 0.37$) between two straight pipes ($L/\gamma R\approx 4.5$) [Van Boven 1993], see figure 3.7.

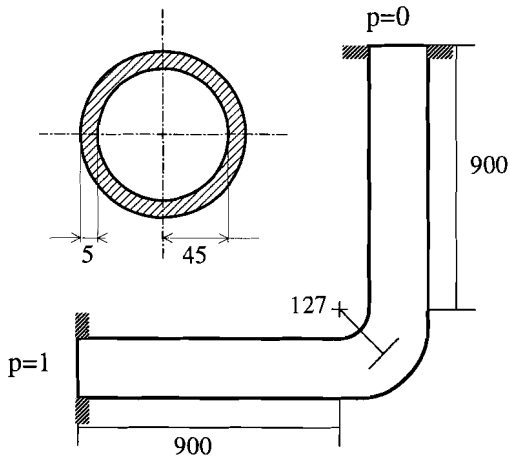


Figure 3.7: geometry of the empty pipe-elbow-pipe system. Sizes are in mm, the figure is not to scale. The pipe material is steel ($E_s=2.1\cdot 10^{11}(1+0.001i)$ N/m², $\nu=0$, $\rho_s=7800$ kg/m³).

The FEM mesh was built of 1008 eight-node shell elements, with 12 elements on a pipe circumference. Hence, the pipe cross-section can deform, so that no flexibility factor is needed. The discrete TMM model of the elbow consisted of two bend points. Table 3.1 gives the lowest four resonance frequencies for clamped/free boundary conditions.

	f_1 [Hz]	f_2 [Hz]	f_3 [Hz]	f_4 [Hz]
FEM model	28	65	387	506
TMM continuous	28	62	375	496
TMM discrete	28	61	362	480

Table 3.1: resonance frequencies of a pipe-elbow-pipe system, for three different models.

The comparison shows small differences between the models, up to 6% at higher frequencies. Although the continuous model appears to give a better agreement with the three-dimensional FEM model, it cannot be concluded that this model is better, because it is not unthinkable that the flexibility factor (that is equal for the TMM models) is too high. Both models will be compared with an experiment in chapter 5.

Elbows may be modelled by either a discrete or a continuous model in the TMM. Both models are approximate, therefore one should be careful with the interpretation of response calculations for systems in which elbows take up a significant part of the length of the system.

3.3.5 other components

Apart from straight pipes and elbows, pipe systems may consist of many different components, for example flanges, bellows, accumulators, valves, orifice plates, pumps, supports or suspensions, branches, diameter or material transitions, etc. Here we will consider the passive transmission of pulsations and vibrations through components. Pumps and valves may also act as source of pulsations or vibrations. This active behaviour will be described in section 3.3.6, as an imposed boundary or intermediate condition to the system.

Some of these components may be modelled as a combination of lumped impedances (masses, springs and dashpots), that can be described in a transfer matrix [e.g. Pestel & Leckie 1964; Snowdon 1971]. We will rearrange the state vectors at the inlet (designated by subscript i) and outlet (subscript o) of the component, to group efforts (superscript F) and displacements (superscript U), as in section 3.2.2.

in-line mass

The unscaled transfer matrix for a lumped, in-line mass may thus be expressed as:

$$\begin{pmatrix} \{F_o\} \\ \{U_o\} \end{pmatrix} = \begin{bmatrix} [I] & \omega^2 [M] \\ [0] & [I] \end{bmatrix} \begin{pmatrix} \{F_i\} \\ \{U_i\} \end{pmatrix}. \quad (3.34)$$

If the mass does not cause fluid-structure interaction, which is for example the case for a flange, then the sub-matrix $[M]$ will be diagonal. The seven matrix coefficients on the diagonal contain the appropriate mass and rotatory inertia terms. The fluctuating pressure difference across a valve or an orifice plate may drive structural vibrations and this fluid-structure interaction will cause off-diagonal terms in the lumped transfer matrix.

in-line stiffness

Flexible components, for example rubber bellows or accumulators, are sometimes applied to relieve the system of mechanical stress, to compensate for volume changes due to temperature fluctuations and to isolate sources of vibrations and pulsations from the piping. The unscaled transfer matrix for an in-line flexible component may be expressed as:

$$\begin{pmatrix} \{F_o\} \\ \{U_o\} \end{pmatrix} = \begin{bmatrix} [I] & [0] \\ [K]^{-1} & [I] \end{bmatrix} \begin{pmatrix} \{F_i\} \\ \{U_i\} \end{pmatrix}, \quad (3.35)$$

where sub-matrix $[K]$ may be complex to describe stiffness and damping. Unlike the mass sub-matrix, this stiffness sub-matrix will not be diagonal, because the translational and rotatory degrees-of-freedom may be coupled. For example, a rubber bellows may be described by means of a stiffness matrix. A complex 'distensibility' parameter [Purhouse 1986] is introduced to describe the effect of the radial stiffness of the bellows on the effective compressibility of the fluid. Coupling factors can be introduced to account for fluid-structure interaction. The estimation of the stiffness, damping and coupling factors for a rubber bellows, however, will be difficult, because these parameters may depend heavily on temperature, internal static pressure and static deflection of the bellows [Veit 1976; Verheij 1982].

out-of-line impedance

Pipe hangers, mechanical supports and side branches may be modelled as out-of-line impedances, for which the transfer matrix can be written as:

$$\begin{pmatrix} \{F_o\} \\ \{U_o\} \end{pmatrix} = \begin{bmatrix} [I] & -i\omega [Z] \\ [0] & [I] \end{bmatrix} \begin{pmatrix} \{F_i\} \\ \{U_i\} \end{pmatrix}. \quad (3.36)$$

A side branch can consist of a linear cascade of components, for which the system transfer matrix can be found by multiplication of component matrices, as for the main pipe line.

The system impedance matrix of the side branch may be determined by the method that was described in section 3.2.2. The sub-matrix $[Z]$ then follows after applying boundary conditions at the end of the branch. The impedance matrix of a pipe hanger or support can be obtained from theoretical modelling. The impedance matrix of a support that is much more flexible than its foundation might be determined in a test rig for the characterization of flexible components [Verheij 1982]. Whenever the impedance of a support is much larger than the local impedance of the pipe system, it should be considered as rigid. In this way one avoids introducing into the model an impedance matrix that contains very large numbers, which may cause numerical instability. A rigid support is not described by a transfer matrix, but by an intermediate boundary condition, see section 3.3.6.

The experimental determination of the relevant transfer matrix coefficients of in-line components will be discussed in chapter 4. An example of an experimentally determined transfer matrix is given in chapter 6 (pulsation transfer through a centrifugal pump).

Transfer matrices of larger components in which higher-order internal modes become important, can be modelled by means of the finite element method (FEM) and then introduced into the TMM. A hybrid method that combines the TMM with the FEM has been successfully applied by Craggs & Stredulinsky [1990] to acoustic wave propagation in a rigid pipe system. The hybrid method is also known as the Finite Element Transfer Method (FETM) in structural mechanics [Tesár & Fillo 1988]. The development of such a hybrid method would be a useful extension of the work that is described in this thesis.

3.3.6 intermediate boundary conditions

The modelling of boundary conditions at the inlet and outlet of a pipe system in the TMM has been treated in section 3.2.1. Internal sources of pulsations or vibrations and rigid supports will locally impose a value for one or more state variables in the system. These are designated 'intermediate boundary conditions'. These intermediate boundary conditions will influence the size of the transfer matrix that describes the pipe system, as will be explained below.

internal sources

Let us consider an internal source, for example a centrifugal pump, that excites vibrations or pulsations in a pipe system. The 'passive' transmission of pulsations and vibrations through the pump is described by a transfer matrix $[T_S]$, whilst the 'active' generation of pulsations or vibrations may be described by a source strength vector $\{Q_S\}$. The state vectors at the inlet and the outlet of the pump are then related as:

$$\{Q_o\} = [T_S]\{Q_i\} + \{Q_S\}. \quad (3.37)$$

In the TMM it is convenient to represent this sum of vectors by increasing the number of columns in the $N \times N$ transfer matrix with the number of variables that are imposed by the source (N_S):

$$\{Q_o\} = \begin{bmatrix} [T_S] & [B_S] \end{bmatrix} \begin{pmatrix} \{Q_i\} \\ \{Q_S\} \end{pmatrix}, \quad (3.38)$$

where the intermediate boundary condition matrix B_S (of N rows and N_S columns) selects the appropriate state variables to be imposed to the system. If this source is preceded by a pipe system that may be described by a transfer matrix $[T_1]$ and followed by a system with matrix $[T_2]$, the transfer matrix equation for the total system will become:

$$\{Q_o\} = \begin{bmatrix} [T_2][T_S][T_1] & [T_2][B_S] \end{bmatrix} \begin{pmatrix} \{Q_i\} \\ \{Q_S\} \end{pmatrix}. \quad (3.39)$$

This equation may be readily solved after application of boundary conditions, because the imposed vector $\{Q_S\}$ does not introduce any new unknown variables.

rigid supports

Let us assume that a rigid support imposes N_R local displacements or rotations to be equal to zero. This implies that the support sustains N_R reaction forces F_R , that will appear as extra unknown variables in the equations that describe such a support. Hence the $N \times N$ transfer matrix for this support will be extended with both N_R rows and N_R columns. The transfer matrix equation may be expressed as:

$$\begin{pmatrix} \{Q_o\} \\ \{0\} \end{pmatrix} = \begin{bmatrix} [I] & [B_F] \\ [B_u] & 0 \end{bmatrix} \begin{pmatrix} \{Q_i\} \\ \{F_R\} \end{pmatrix}, \quad (3.40)$$

where the sub-matrix $[B_u]$ selects the imposed displacement or rotation variables and the sub-matrix $[B_F]$ the corresponding forces or moments. Like the internal source above, a rigid support may be located between two pipe systems with transfer matrices $[T_1]$ and $[T_2]$. The total system can then be described by

$$\begin{pmatrix} \{Q_o\} \\ \{0\} \end{pmatrix} = \begin{bmatrix} [T_2][T_1] & [T_2][B_F] \\ [B_u][T_1] & [0] \end{bmatrix} \begin{pmatrix} \{Q_i\} \\ \{F_R\} \end{pmatrix}. \quad (3.41)$$

This transfer matrix equation contains N_R extra unknown variables in the inlet state vector.

It also introduces N_R extra known variables (equal to zero) in the outlet state vector, so that the unknown variables may be solved.

3.4 Computer program *PRESTO*

The above transfer matrix model for fluid-filled pipe systems is built into a computer program, that is called *PRESTO* (Pipe system *RES*ponse and Transfer of *nO*ise). The program is based on the mathematical software package *MATLAB*. The program consists of several subroutines to determine the transfer matrices of pipe system components, to build the system matrix and to solve the matrix equation.

3.4.1 numerical solution

The solution method for the TMM has been given in section 3.2. In the program the matrix equation $[T_{o1}^{KU}]\{Q_i^U\} = \{Q_o^K\} - [T_{o1}^{KK}]\{Q_i^K\}$ is solved for $\{Q_i^U\}$ by means of Gaussian elimination with partial pivoting. $\{Q_o^U\}$ is then obtained by substitution of $\{Q_i^U\}$ in eq.(3.5). In section 3.4 it was shown that the size of the system transfer matrix increases if the pipe system contains internal sources or rigid supports, but this does not influence the solution method. With the first version of the program it appeared that the applicability was seriously hampered by numerical round-off errors due to the cosh- and sinh-terms in the transfer matrices for flexural motion of straight pipes, see section 3.3.3. Problems occurred when the condition number, defined as the ratio of the largest and smallest singular values of the sub-matrix $[T_{o1}^{KU}]$, see eq.(3.5), reached the order of magnitude of the inverse of the numerical resolution of the computer. The condition number for the straight pipe matrix is of the order of magnitude of $\exp(k_N L)$. In *MATLAB* the resolution is 10^{-16} , so that round-off errors become important (greater than 0.1%) when $k_N L \geq \ln(10^{13})$, i.e. when the pipe length is more than $4\frac{3}{4}$ times longer than the wavelength of the bending nearfield. A solution to this problem has been found in dividing the pipe system into sub-systems, for which the condition number of the relevant part of the transfer matrix is smaller than a predefined value (e.g. 10^{13}). These sub-system transfer matrix equations are then solved in parallel. The size of the system transfer matrix increases by 14 columns and 14 rows for each new sub-system. This may be illustrated by the following example. Let us consider a pipe system that is divided into two sub-systems with transfer matrices $[T_{sub1}]$ and $[T_{sub2}]$. A parallel solution of these sub-systems involves not only the solution of the state vectors at the inlet $\{Q_i\}$ and outlet $\{Q_o\}$ of the system, but also of the state vector $\{Q_c\}$ at the pipe cross-section where the sub-systems are connected. The system matrix equation can then be written as:

$$\begin{pmatrix} \{0\} \\ \{Q_o\} \end{pmatrix} = \begin{bmatrix} [T_{\text{sub1}}] & -[I] \\ [0] & [T_{\text{sub2}}] \end{bmatrix} \begin{pmatrix} \{Q_i\} \\ \{Q_c\} \end{pmatrix}. \quad (3.42)$$

The 14 unknown variables in $\{Q_c\}$ may be solved, because 14 extra equations have been introduced. Hence the same approach can be chosen to solve a local response at a pipe cross-section directly, instead of deriving it from the state vector at a system boundary by matrix multiplication. A similar solution method has been applied by Tentarelli [1990]. In *PRESTO* the matrix condition number is introduced as the parameter that governs the necessity to introduce sub-systems. The ratio of pipe length to bending nearfield wavelength decreases with frequency, so that more sub-systems will be needed at higher frequencies. The numerical efficiency is greatly enhanced by letting the program decide at each frequency whether or not sub-systems are required, with the condition number of the (sub-)system transfer matrix as control parameter [van Boven 1993; 1994].

3.4.2 accuracy

The relative error in the solution vector Q_i^U due to perturbations in the input data can be expressed as:

$$\frac{\|\Delta\{Q_i^U\}\|}{\|\{Q_i^U\}\|} \leq \text{cond}([T_{oi}^{KU}]) \frac{\|\Delta[T_{oi}^{KU}]\|}{\|[T_{oi}^K]\|} + \text{cond}(\{F\}) \frac{\|\{\Delta F\}\|}{\|\{F\}\|}, \quad (3.43)$$

with $\{F\} = \{Q_o^K\} - [T_{oi}^{KK}]\{Q_i^K\}$. Here $\|\cdot\|$ denotes the norm of a matrix or vector. The condition numbers can be calculated from:

$$\text{cond}([T_{oi}^{KU}]) = \|[T_{oi}^{KU}]^{-1}\| \cdot \|[T_{oi}^{KU}]\|, \quad \text{cond}(\{F\}) = \frac{\|[T_{oi}^{KU}]^{-1}\| \cdot \|\{F\}\|}{\|\{Q_i^U\}\|}. \quad (3.44)$$

The condition number of the sub-matrix $[T_{oi}^{KU}]$ may become quite large (it may easily be larger than 10^{10} !). This means that small perturbations in the input data may be greatly amplified. However, as long as analytically determined transfer matrices are used, the relative error in $[T_{oi}^{KU}]$ will be predominantly determined by numerical round-off errors, the effect of which can be limited by bounding the size of the subsystems, as described in section 3.4.1. Perturbations in the boundary conditions, for example due to the use of measured data, are amplified proportional to the condition number of the boundary condition vector $\text{cond}(\{F\})$, that is close to one. Hence the accuracy of the results of the numerical model can be acceptable, in spite of the large condition numbers $\text{cond}([T_{oi}^{KU}])$. However, one should be very careful with the introduction of experimentally determined transfer matrices into the model.

3.5 Examples

This section shows two examples of the application of the TMM computer program *PRESTO*. More examples will be given, in relation to experiments, in chapter 5.

3.5.1 fluid-structure interaction at an end plate

The first example concerns a straight, water-filled, steel pipe, see figure 3.8. At one side the fluid is driven by an oscillating piston, the other end is closed by a mass-less end plate. The aim of this example is to show the effect of fluid-structure interaction on the dynamic behaviour of pipe and fluid. Poisson contraction has been neglected ($v=0$), so that the fluid pulsations will only couple to pipe wall vibrations at the end plate if it is free to move. The interaction at the end plate (at $z=L$) is governed by the equations of continuity and equilibrium:

$$v(z=L) = u_z(z=L) , \quad A_f p(z=L) = F_z(z=L) . \quad (3.45)$$

This configuration is compared with a configuration in which fluid-structure interaction is suppressed by clamping the end plate. Figure 3.9 shows the input impedance of the fluid at the piston as calculated by *PRESTO* for both configurations. These can be explained as follows. Because the fluid is driven by an ideal volume source at $x=0$, the impedance of the fluid at the end plate equals:

$$Z_f(z=L) = \frac{A_f p(z=L)}{\dot{v}(z=L)} = \frac{-i \rho_f A_f c_F}{\tan(k_F L)} . \quad (3.46)$$

Without coupling, maxima in the impedance will occur at the resonance frequencies of a pipe with closed ends ($Z_f(L) \rightarrow \infty$), where the pipe length agrees with multiples of half a wavelength in the fluid ($k_F L = \pi$). The impedance of the pipe, that is clamped at $z=0$, is:

$$Z_p(z=L) = \frac{F_z(z=L)}{\dot{u}_z(z=L)} = \frac{i \rho_s A_s c_E}{\tan(k_E L)} . \quad (3.47)$$

Without coupling, the pipe (with clamped/free boundary conditions) will show a resonance when its length agrees with a quarter of the wavelength of quasi-longitudinal waves in the wall ($k_E L = \pi/2$). The resonance frequencies of the coupled system occur at frequencies where $Z_f(L) = Z_p(L)$, as can be seen from eqs.(3.45)-(3.47). Since the ratio of the wave velocities of quasi-longitudinal and fluid waves $c_E/c_F \approx 3.9$ for the given pipe, the uncoupled structural resonance would nearly coincide with the second uncoupled fluid resonance. However, the end plate would show a large displacement at the structural resonance, while the uncoupled fluid resonance requires a minimum displacement at the end plate. Therefore

both resonances will show a strong interaction, resulting in two coupled resonances at frequencies that are shifted in comparison with the uncoupled resonance frequencies. Similar effects are shown by Fahy [1985] for a mass-spring system that is coupled to a fluid column.

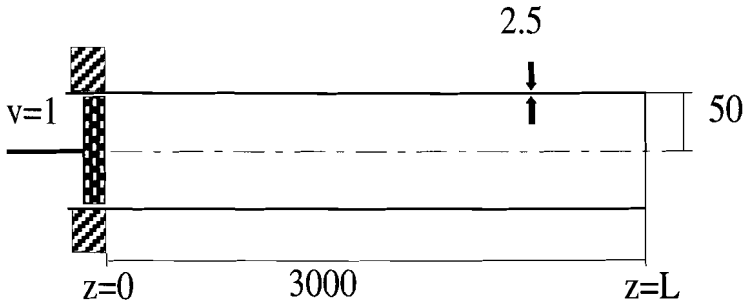


Figure 3.8: a straight water-filled steel pipe ($E_s=2.1 \cdot 10^{11}(1+0.001i) \text{ N/m}^2$, $\nu=0$, $\rho_s=7800 \text{ kg/m}^3$, $K_f=2.15 \cdot 10^9 \text{ N/m}^2$, $\rho_f=1000 \text{ kg/m}^3$). The sizes are in mm. At one end the pipe is clamped and the fluid is driven by an oscillating piston, at the other end the pipe is closed with a massless end plate that is either clamped or free to move.

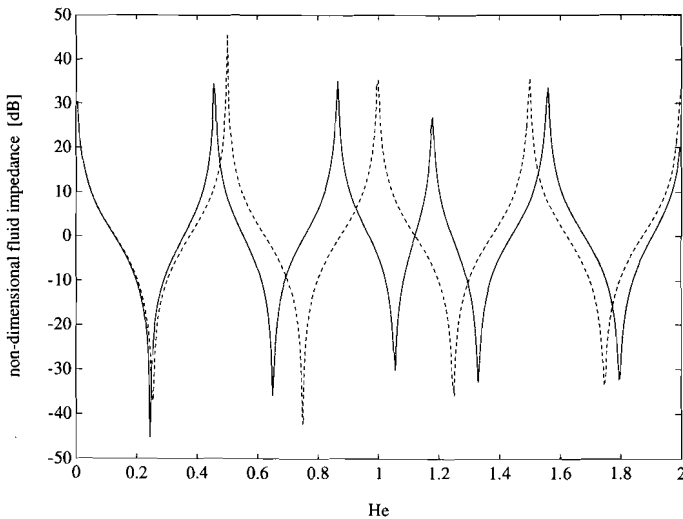


Figure 3.9: non-dimensional input impedance (\bar{p}/\bar{v}) of the fluid at the piston in figure 3.7, with a free (-) or clamped (--) end plate, as a function of the Helmholtz number $He=fL/c_F$.

3.5.2 response of a simple pump circuit

A response calculation of a simplified model of a pipe system with a centrifugal pump and a pressure vessel is considered. With this example it is intended to show that similar coupling effects as in the simple example of section 3.5.1 are found. Geometry, material properties and boundary conditions are given in figure 3.10. The fluid is non-viscous and the mean flow does not affect the pulsations and vibrations. Since the pump only excites the fluid, it is interesting to compare the results with the results of a calculation for the fluid only, to study the effect of fluid-structure interaction. The reduced fluid wave velocity, due to the effect of the circumferential stiffness of the pipes (eq.2.28), is used in the uncoupled calculation. Figure 3.11 shows the spectrum of the pressure pulsation at the suction side of the pump (position A), scaled with the pulsation source strength Δp . The results of coupled (solid line) and uncoupled (dashed line) calculations are compared. Let us look at the resonance peaks between 50 and 100 Hz. Here the second uncoupled fluid resonance (where the system length equals one fluid wavelength) nearly coincides with a structural resonance, so that two new coupled resonances arise, just like in the example of section 3.5.1. This again illustrates the practical importance of a coupled calculation when predicting the vibration response of a fluid-filled pipe system. The mode shape for the coupled resonance at 87 Hz is displayed in figure 3.12, where the displacement is exaggerated.

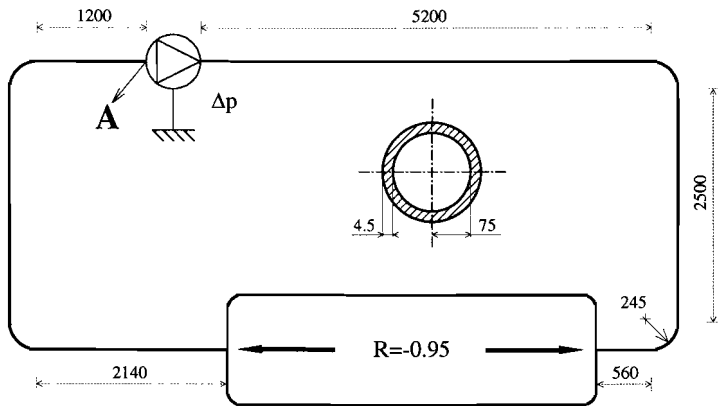


Figure 3.10: a pipe system with a pump and a pressure vessel. Sizes are in mm. The pipes are made of steel ($E_s=2.1 \cdot 10^{11}(1+0.01i) \text{ N/m}^2$, $\rho_s=7800 \text{ kg/m}^3$, $\nu=0.3$) and filled with water ($K_f=2.15 \cdot 10^9 \text{ N/m}^2$, $\rho_f=1000 \text{ kg/m}^3$). The pipe system model is terminated at the vessel with clamped boundary conditions for the structure and a reflection coefficient $R=-0.95$ for the fluid. The pump is modelled as an intermediate boundary condition: clamped for the structure and a source strength Δp for the fluid.

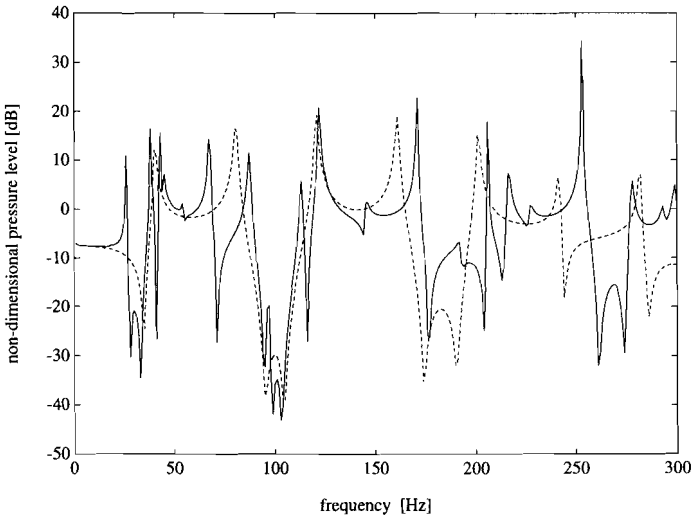


Figure 3.11: pressure, scaled with the pressure source strength, at position A in figure 3.10. The solid line is the result of the PRESTO-calculation and the dashed line is the result of a calculation without fluid-structure interaction.

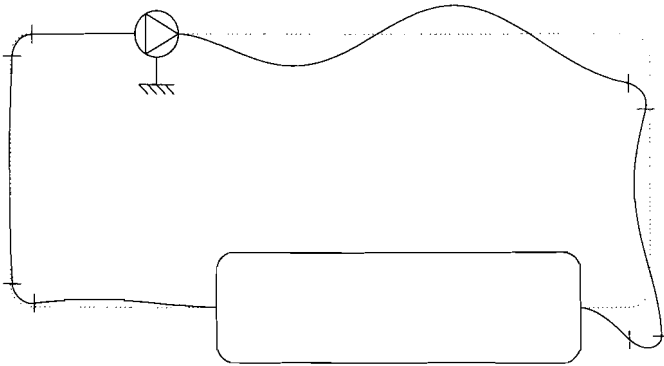


Figure 3.12: Mode shape for the coupled resonance of the pump circuit at 87 Hz.

3.6 Conclusion

A transfer matrix model for the beam-like dynamic behaviour of fluid-filled pipe systems has been presented in this chapter. This model may be applied to determine the response of pipe systems to a source of pulsations or vibrations, with the source strength as input, or to investigate the transmission of vibro-acoustic energy through the system, in terms of its impedance matrix.

Analytical expressions have been derived for the transfer matrix coefficients for a straight fluid-filled pipe. Two different approximate models (a continuous and a discrete model) for elbows have been reviewed and their results have been compared, with a three-dimensional FEM calculation as a reference. The comparison shows that the approximate elbow models introduce an uncertainty in the response predictions of pipe systems, that may become serious when modelling pipe systems in which elbows take up a large part of the system length. This difficulty may possibly be overcome in a hybrid method, in which the elbow transfer matrix is determined from a three-dimensional FEM calculation. A procedure for modelling other pipe system components (flanges, bellows, supports, etc.) has been described, as well as the handling of intermediate boundary conditions.

The model has been built into the computer program *PRESTO*. The sensitivity for input errors has been evaluated and a method to control the convergence of the solution with respect to numerical round-off errors has been described. Finally two examples have been given to demonstrate the applicability of the program and the importance of fluid-structure interaction for the response of fluid-filled pipe systems.

4. EXPERIMENTAL METHODS

4.1 Introduction

This chapter describes methods for the experimental determination of quantities like vibro-acoustic energy flow, terminating and transfer impedances or source strength in fluid-filled pipe systems. In chapter 2 we saw that the vibro-acoustic behaviour of fluid-filled pipes is governed by the simultaneous propagation of multiple types of waves. In practical pipe systems many of these waves will be coupled strongly at elbows, supports and other discontinuities, so that it is very likely that several wave types will be excited. For measurements this means that each single transducer signal and each quantity of interest may consist of contributions of multiple waves. Therefore, performing measurements of pressure pulsations or accelerations on a pipe without applying a wave decomposition technique or, at least, checking that the wave type under investigation is predominant, may lead to serious errors in the interpretation and in the results of further processing of the data.

The experimental wave decomposition technique involves the estimation of the complex amplitude spectra of the separate waves from measurements of accelerations or pressure pulsations (or other physical quantities for which practicable transducers are available) at a number of positions in a section of the pipe system. The estimation relies on the analytical model for wave propagation in a straight fluid-filled pipe that has been given in chapter 2. The resulting wave amplitudes give a complete description of the local wave field in the pipe section. All other wave field descriptors, like energy flow, acoustic and mechanical impedances and reflection coefficients, can directly be derived from these amplitudes.

Wave decomposition lies at the basis of the well-established two-microphone-method for measuring the reflection coefficient for acoustic waves in a duct [Chung & Blazer 1980]. It is related to the techniques for measuring acoustic intensity [Fahy 1977; Pavić 1977] and structure-borne energy flow [Noiseux 1970; Pavić 1976; Verheij 1980], that are based on a finite difference approximation of the wave fields. However, the wave decomposition technique has the advantage that it does not suffer from finite difference approximation errors and that it gives direct access to a whole series of wave field descriptors. Recently the application of wave decomposition techniques has been studied in relation to higher order waves in ducts by Stahl [1987] and Åbom [1989], in relation to beam flexure by Taylor [1990], Trollé & Luzzato [1990] and Halkyard [1993] and in relation to waves in fluid-filled pipes by Pavić [1992,1993]. The appropriate wave type decomposition

techniques for application to fluid-filled pipes are described in section 4.2

The experimental methods to determine the wave field in a given pipe system, provide a tool for the more elaborate methods to determine the vibro-acoustic characteristics of pipe system components. We saw in chapter 3 that passive components may be characterized in terms of their impedance or transfer matrix and active components in terms of their vibro-acoustic source strength vector. Generally the number of characteristic parameters (e.g. matrix coefficients) is too large to be solved from measurements in a single pipe system configuration, so that the characterization methods have to rely on successive measurements on different configurations. Experimental characterization methods that rely on measurements on different configurations to determine source and transfer characteristics, have been studied for components of duct systems. The 'two-load' method [Kathuriya & Munjal 1976] and the 'two-source-location' method [Munjal & Doige 1990], have been applied to ventilation and exhaust systems in which the influence of pipe vibrations on the duct acoustics may be neglected. Section 4.3 describes the application of this type of 'inverse' methods for the characterization of components of fluid-filled pipe systems.

4.2 Wave decomposition

It has been shown in chapter 2 that the solutions to the equations of motion of a straight fluid-filled pipe may be decomposed in mutually independent circumferential modes ($n=0,1,..$). At each circumferential mode n , multiple axial waves ($m=1,2,..$) may exist. Fortunately, many of these waves are evanescent at frequencies far below the ring frequency of the pipe, so that they are only of importance for measurements on very short pipes or very close to discontinuities. For practical application the wave decomposition method can be restricted to a limited number of relevant wave types. Here, we will limit ourselves to the frequency range below the cut-on frequency (f_{c3}) of $n=3$ propagating waves. The extension of the methods that are presented in this chapter to the next higher order ($n=3,4,..$) modes is straightforward, since these lobar waves all exhibit a behaviour like the $n=2$ mode. It is assumed that the higher order ($n>2$) evanescent waves do not contribute to the measured wave field in the frequency range below f_{c3} . The validity of this assumption depends on the modal content of the excitation and the distance between the measurement cross-section and the locations where these evanescent waves are excited. Figure 2.2d shows that the non-dimensional complex wavenumber for $n=3$ at low frequencies (for a water-filled steel pipe with wall with $h/a=0.05$) is approximately equal to $k_3 a \approx 0.7$, so that the corresponding evanescent wave amplitude (that is proportional to e^{-kz}) is reduced to 1% at a distance of 6.6 times the pipe radius from the excitation location. Excitation of higher order evanescent waves may for example take place at elbows. The

modal content of the excitation is geometry dependent. For example, an elbow may be connected to the pipes by means of flanges, that are stiffer than the pipe wall. Below frequencies where the flanges exhibit lobar deformation, these flanges will suppress the excitation of higher order modes.

4.2.1 circumferential mode decomposition

The circumferential modes ($n=0,1,2$) are decomposed by application of an array of transducers at a pipe cross-section. Each motion variable \hat{q} ($q=u,v,w,p,$ etc.) may be described as:

(4.1)

$$\hat{q}(z,\theta,\omega) = \hat{q}_0(z,\omega) + \hat{q}_1(z,\omega) \cos(\theta + \alpha_1(z,\omega)) + \hat{q}_2(z,\omega) \cos(2\theta + \alpha_2(z,\omega)) .$$

Consequently the three amplitudes ($\hat{q}_0, \hat{q}_1, \hat{q}_2$) and the two polarization angles (α_1, α_2) may be derived from measurements at five, or more, circumferential positions at the pipe wall. Measurements using less transducers per pipe cross-section may cause an ambiguity with respect to the type of wave that is responsible for the measured response. It is advantageous to select the circumferential positions of the transducers in such a way that the decomposition results in simple addition and subtraction of transducer signals. These operations may be performed by means of special purpose analogue electronic devices so that a single electrical signal remains for each modal amplitude at each pipe cross-section. It remains to select which variables of motion are to be measured.

In section 2.5 it was argued that each wave may be characterized by the complex amplitude spectrum of one representative quantity, for example a component of the pipe wall motion. The spectra of all other quantities may be obtained by multiplication of this representative spectrum with fixed amplitude ratios that have been given in section 2.5. The choice of the characteristic variable of motion for each wave will depend on which variable is predominating and, moreover, for which variable appropriate transducers are available.

The wave type decomposition techniques that are described in this thesis rely on the use of accelerometers and pressure transducers. The application of accelerometers is well-established and procedures to calibrate the amplitude and phase characteristics and to select sets of accelerometers with matched sensitivities are readily available [Verheij 1982,1990]. The accelerometers are mounted on the pipe wall in radial, axial or tangential direction with the help of aluminium studs, see figure 4.1. Although there is a direct relationship between the pressure in a flexible pipe and the radial 'breathing' motion of the pipe wall (eq.2.20), the corresponding radial acceleration may be too small to be measured with accelerometers (as will be explained in section 4.2.4. Where possible, acceleration compensated piezo-electric

pressure transducers, mounted flush in the pipe wall, are used to measure the internal fluid pressure. Pinnington and Briscoe [1992,1993] have recently demonstrated the use of a piezo-electric (PVDF) wire, wrapped circumferentially around the pipe, to determine the internal fluid-pressure from the circumferential strain of the wall. This type of sensor seems very interesting for situations where non-intrusive measurement of the fluid pressure is necessary. Strain gauges may also be used for the wave decomposition [Pavić 1992,1993]. Halkyard & Mace [1993] have shown that the wave decomposition for flexural waves in a beam can be improved by applying a combination of accelerometers and strain gauges, instead of only accelerometers. However, the amplitude and phase calibration is more difficult for strain transducers than for accelerometers.

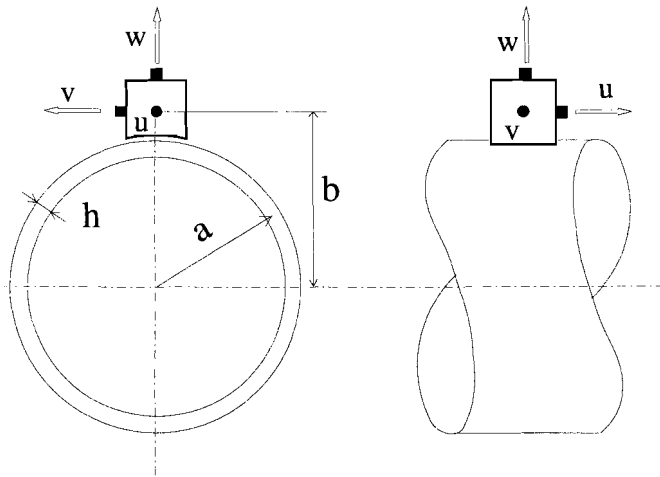


Figure 4.1: Stud for mounting accelerometers on the pipe wall in axial, radial and transverse directions.

In practice a set of four accelerometers will be used for the circumferential mode decomposition of the pipe wall motion. They are mounted at equidistant positions ($\theta_A=0^\circ$, $\theta_B=90^\circ$, $\theta_C=180^\circ$, $\theta_D=270^\circ$), see figure 4.2a. Their operation may be explained as follows. In this configuration all accelerometer signals will be in-phase for the $n=0$ mode. Signals of transducers at opposite sides of the pipe will be out-of-phase for $n=1$. For the $n=2$ mode the signals of transducers at opposite sides of the pipe will be in-phase, but out-of-phase with the signals of the other two transducers. The modal amplitudes are then derived from:

$$\hat{q}_0 = \frac{1}{4} (\hat{q}_A + \hat{q}_B + \hat{q}_C + \hat{q}_D),$$

$$|\hat{q}_1| \cos(\alpha_1) = \frac{1}{2} (\hat{q}_A - \hat{q}_C), \quad |\hat{q}_1| \sin(\alpha_1) = \frac{1}{2} (\hat{q}_B - \hat{q}_D), \quad (4.5)$$

$$|\hat{q}_2| \cos(\alpha_2) = \frac{1}{4} \left((\hat{q}_A + \hat{q}_C) - (\hat{q}_B + \hat{q}_D) \right),$$

where α_1 and α_2 are the initial polarization angles of the $n=1$ and $n=2$ modes. To determine the polarization angle of the $n=2$ motion an extra measurement is performed after rotating the set of accelerometers through 45° , see figure 4.2b, so that:

$$|\hat{q}_2| \sin(\alpha_2) = \frac{1}{4} \left((\hat{q}_E + \hat{q}_G) - (\hat{q}_F + \hat{q}_H) \right). \quad (4.6)$$

Note that the measurement with the rotated set of accelerometers is only necessary if one is interested in obtaining the amplitude and polarization angle of the $n=2$ waves, while the measurement with the first set is sufficient to determine the contributions of the other two modes, while suppressing the $n=2$ motion.

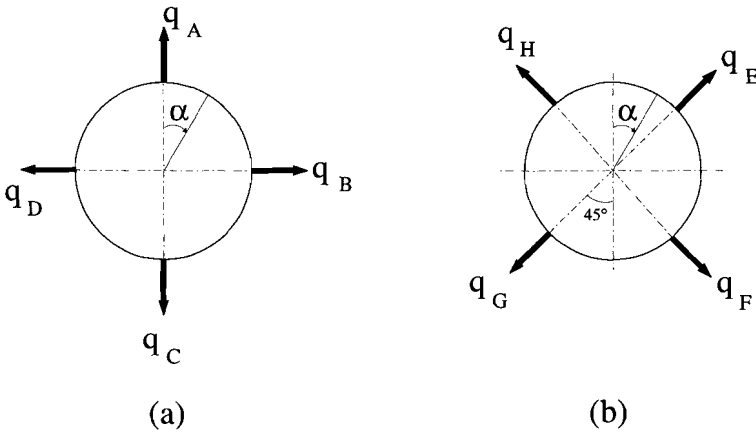


Figure 4.2: Transducer configuration for circumferential wave decomposition for $n < 3$.

(a) first measurement;

(b) second measurement after rotation of the set of transducers through 45° .

4.2.2 axial wave decomposition

Once the circumferential modes n have been decomposed, the axial modes m corresponding to each mode $n=0,1,2$ may be decomposed by selection of the appropriate transducer configuration, at a number of axial positions along the pipe. The modal amplitude of the generalized motion variable \hat{q} at each cross-section may be expressed as:

$$\hat{q}_n(z, \omega) = \sum_{m=1}^M A_{nm}^+(\omega) e^{-ik_{nm}z} + A_{nm}^-(\omega) e^{ik_{nm}z} . \quad (4.7)$$

The $2M$ complex wave amplitudes ($A_{nm}^{\pm}, A_{nm}^{\pm}$) may then be estimated from $2M$ measurements \hat{q}_j . To separate the waves that are travelling in positive and negative axial direction measurements should be performed at, at least, two different axial positions. The waves with different wavenumbers may be identified on the basis of measurements at different cross-sections, or on the basis of measurements of different physical variables (e.g. different components of wall acceleration, internal pressure, or axial strain [Halkyard 1993]). To estimate the wave amplitudes, the relation between the measured variables and the wave amplitudes (eq.4.4) may be best expressed in matrix form:

$$\{Q\} = [F] \{A\} , \quad (4.8)$$

where the measurements are collected in the vector $\{Q\}$ and the wave amplitudes in vector $\{A\}$. The coefficients of the matrix $[F]$ can be deduced from the wave propagation model, with the introduction of numerical values for geometrical (e.g. transducer positions) and material (e.g. wavenumbers) properties. The matrix equation may be solved provided that the matrix $[F]$ is not singular. This imposes limitations on the selection of transducers and transducer positions. The matrix condition number (see section 3.5.2) can be used as an indicator for a matrix that is close to singular.

This general description of the wave decomposition technique will become clearer when it is applied to specific waves. We saw in chapter 2 that the following groups of axial waves play a role in the low frequency range of interest:

- torsional waves in the pipe wall at $n=0$
- plane waves in the fluid and extensional waves in the pipe wall at $n=0$
- bending waves and evanescent bending waves at $n=1$
- lobar waves and evanescent lobar waves at $n=2$

Torsional waves can only be measured using the transverse acceleration of the pipe wall. At low frequencies axial wall acceleration dominates over radial acceleration for extensional waves and fluid waves and both waves can also be measured in the fluid

pressure. The acceleration of the pipe wall is predominantly radial for the higher order waves ($n > 0$).

For a certain circumferential mode the measured signal may be determined by either one, two, three or four waves, travelling in either positive or negative axial direction. The number of waves determines the size of the square matrix $[F]$ and thereby imposes the number of measurement 'channels' that are required for the wave decomposition. The 'one-channel method' will only apply to uncoupled waves in a semi-infinite pipe at positions sufficiently far from the excitation point and is therefore not very interesting for practical application. The 'two-channel method' is much more interesting because it applies to all uncoupled waves in pipes of finite length. This method has been developed for acoustic waves in a duct, resulting in the well-known *two-microphone method* [Chung & Blazer 1980; Bodén & Åbom 1986]. With respect to fluid-filled pipes, it always applies to torsional waves. It applies to propagating bending waves at positions far (e.g. more than half a wavelength) from discontinuities (like elbows or supports). Plane waves in the fluid and extensional waves in the wall are coupled via Poisson-contraction, the coupling being governed by the parameter $\tilde{\nu}\sigma$ (see eq.3.20 and eq.3.21). If $\tilde{\nu}\sigma \ll 1$ (i.e. if the wall is much less flexible than the fluid) both waves may be considered to be uncoupled and may be treated separately, so that the 'two-channel method' applies. The 'three-channel method' applies in the presence of a single nearfield (evanescent bending or lobar wave), that is, close to a discontinuity but sufficiently far from the next discontinuity in the pipe. Finally, the 'four-channel method' applies to coupled fluid waves and extensional waves in pipes with a significant Poisson-coupling or to bending and lobar waves in pipes that are short compared to the decay distance of the evanescent waves. 'Three-channel' and 'four-channel' decomposition methods for flexural waves in thin beams have been described by Taylor [1990] and Halkyard & Mace [1993]. In the next sections we will describe 'two-channel' and 'four-channel' methods for axial wave decomposition in fluid-filled pipes.

4.2.3 the two-channel method

We will follow Taylor [1990] to demonstrate the equivalence between the 'two-channel' axial wave decomposition method and well-known methods like the *two-microphone method* for acoustic waves in a duct and the cross-spectral methods for measuring structure-borne power flow on beams and pipes [Verheij 1980]. Under the conditions that have been discussed above, the two-channel method is applicable to all propagating waves in a fluid-filled pipe. The method involves a single two-channel FFT measurement for each wave type, which makes it an elegant method for practical application. A procedure for vibro-acoustic energy flow measurements on pipes has been developed on the basis of this method [de Jong, Verheij & Bakermans 1992] and will be presented below.

The matrix equation (4.5) for a two-channel method, that is based on the measurement of two equal variables at two different axial positions, can be written as:

$$\begin{pmatrix} \hat{q}_{nm}(z_1) \\ \hat{q}_{nm}(z_2) \end{pmatrix} = \begin{bmatrix} e^{-ik_{nm}z_1} & e^{ik_{nm}z_1} \\ e^{-ik_{nm}z_2} & e^{ik_{nm}z_2} \end{bmatrix} \begin{pmatrix} A_{nm}^+ \\ A_{nm}^- \end{pmatrix}. \quad (4.9)$$

The wave amplitudes may be obtained by matrix inversion, resulting in:

$$\begin{pmatrix} A_{nm}^+ \\ A_{nm}^- \end{pmatrix} = \frac{-1}{2i\omega^2 \sin(k_{nm}\Delta_{nm})} \begin{bmatrix} e^{ik_{nm}z_2} & -e^{ik_{nm}z_1} \\ -e^{-ik_{nm}z_2} & e^{-ik_{nm}z_1} \end{bmatrix} \begin{pmatrix} \hat{q}_{nm}(z_1) \\ \hat{q}_{nm}(z_2) \end{pmatrix}, \quad (4.10)$$

with $\Delta_{nm}=z_2-z_1$. The matrix inversion is subject to errors when the transducer spacing Δ_{nm} is close to zero or to an integral number of half-wavelengths. The accuracy with which the complex wave amplitudes are determined will depend on the accuracy of the measurements (amplitude and phase of \hat{q}_{nm}) and on the accuracy of the estimations of the wavenumber (k_{nm}) and the axial positions (z_1, z_2). We may generalize the main results of the extensive study of the influence of errors on the two-microphone method by Bodén & Åbom [1986] and state that the two-channel method will be least sensitive to errors if the condition is fulfilled that

$$0.1\pi \leq k_{nm}\Delta_{nm} \leq 0.8\pi. \quad (4.11)$$

Hence, the optimum transducer spacing will be different for waves with different wave numbers and for different frequency ranges.

All wave field descriptors may now be expressed in terms of the two complex wave amplitudes. However, for practical application it is advantageous to relate relevant descriptors, like the reflection coefficient and the vibro-acoustic energy flow, directly to the auto- and cross-power spectra that are obtained from two-channel FFT analysis:

$$\begin{aligned} G_{11}(\omega) &= \frac{1}{2} E \left(\hat{q}_{nm}^*(z_1, \omega) \cdot \hat{q}_{nm}(z_1, \omega) \right), \\ G_{12}(\omega) &= \frac{1}{2} E \left(\hat{q}_{nm}^*(z_1, \omega) \cdot \hat{q}_{nm}(z_2, \omega) \right), \end{aligned} \quad (4.12)$$

where the expected value $E(q)$ is determined by averaging over a number of spectra and q^* the complex conjugate of q .

The *reflection coefficient* R_{nm} is defined as the ratio of the amplitudes of incident and

reflected waves at a given pipe cross-section (axial position z_0). Its relationship to the measured two-channel frequency response function $H_{12}=G_{12}/G_{11}$ can be found from eqs.(4.6) and (4.9) as:

$$R_{nm}(z_0, \omega) = \frac{A_{nm}^- e^{ik_{nm}z_0}}{A_{nm}^+ e^{-ik_{nm}z_0}} = e^{2ik_{nm}(z_0-z_1)} \frac{H_{12}(\omega) - e^{-ik_{nm}\Delta_{12}}}{e^{ik_{nm}\Delta_{12}} - H_{12}(\omega)}. \quad (4.13)$$

This formula, which is well known from the two-microphone method for acoustic waves in a duct, appears to be valid for all uncoupled vibro-acoustic waves in a pipe.

In section 2.6.4 it has been shown that the time-average, fluid- and structure-borne, *vibro-acoustic energy flow* in each wave type is proportional to the difference of squared wave amplitudes:

$$P_{nm}(\omega) = C_{nm}(\omega) \frac{1}{2} \left(|A_{nm}^+|^2 - |A_{nm}^-|^2 \right), \quad (4.14)$$

where $C_{nm}(\omega)$ is a constant of proportionality that depends on the type of transducer that is used and on the specific impedance of the waves. The cross-spectral method for measuring vibro-acoustic intensity in beams and pipes [Verheij 1980] is based on the fact that this difference of squared amplitudes is directly proportional to the imaginary part of the measured cross-spectrum G_{12} . Substitution of eq.(4.6) into the definition of the cross-spectrum leads to the conclusion that the power spectrum of the time-averaged energy flow may be determined from

$$P_{nm}(\omega) = \frac{-C_{nm}(\omega)}{\sin(k_{nm}\Delta_{nm})} \text{Im} \left(G_{12}(\omega) \right). \quad (4.15)$$

Simplified expressions result for the measurement of vibro-acoustic energy flow in the five types of wave propagation that are responsible for noise transmission at frequencies below the cut-on frequency of $n=3$ waves in long, straight, fluid-filled pipes. The structure-borne energy flow measurement is performed by means of sets of accelerometers, the fluid-borne energy flow measurement by means of pressure transducers. The following expressions are found (these expressions are less approximate than the expressions that have been presented in [de Jong & Verheij 1992]) :

- pressure waves in the fluid:

$$P_F(\omega) \approx \frac{-A_f}{\rho_f c_F \sin(k_F \Delta_F)} \text{Im} \left(G_{12}(P_{F1}, P_{F2}) \right), \quad (4.16)$$

- longitudinal extensional waves:

$$P_E(\omega) \approx \frac{-A_s \rho_s c_S}{\omega^2 \sin(k_S \Delta_S)} \text{Im} \left(G_{12}(\ddot{u}_{S1}, \ddot{u}_{S2}) \right), \quad (4.17)$$

- torsional waves:

$$P_T(\omega) = \frac{-A_s \rho_s c_T}{\omega^2 \sin(k_T \Delta_T)} \frac{a^2}{b^2} \text{Im} \left(G_{12}(\ddot{v}_{T1}, \ddot{v}_{T2}) \right), \quad (4.18)$$

- bending waves:

$$P_B(\omega) \approx \frac{-2 m' c_B}{\omega^2 \sin(k_B \Delta_B)} \frac{(\check{c}_B/c_B)^4}{(1 + k_B^2 a^2)^3} \text{Im} \left(G_{12}(\ddot{w}_{B1}, \ddot{w}_{B2}) \right), \quad (4.19)$$

- n=2 lobar waves:

$$P_L(\omega) \approx \frac{-8 m' c_L}{\omega^2 \sin(k_L \Delta_L)} \frac{(\check{c}_B/c_L)^4}{(4 + k_L^2 a^2)^3} \text{Im} \left(G_{12}(\ddot{w}_{L1}, \ddot{w}_{L2}) \right), \quad (4.20)$$

In these equations the double dot denotes acceleration (the second time derivative of displacement). The wave velocities (c_F, c_E, c_T, c_B, c_L) and the corresponding wavenumbers ($k=\omega/c$) are the exact solutions of the dispersion equation, see section 2.4. Note that \check{c}_B equals the bending wave velocity according to the Euler/Bernoulli beam theory (eq.2.30). The equations for structure-borne energy flow in longitudinal, torsional and bending waves are comparable with the corresponding equations for energy flow in a beam by Verheij [1980]. However, Verheij's equations are based on simple beam theory and on a finite difference approximation. The above equations are based on shell theory and avoid finite difference errors, by applying the sine function instead of its approximation for a small argument: $\sin(k\Delta) \approx k\Delta$. The equation for torsional waves (eq.4.15) contains a correction factor because the transverse accelerations are measured at radius b (see fig.4.1). The correction factor in the expression for bending waves (eq.4.16) allows this equation to be used beyond the frequency range where simple beam bending is valid. The expression for n=2 lobar waves (eq.4.17) is equivalent to the equation for bending waves and can be

easily extended to the next few higher circumferential orders, with the help of eq.(2.47). Note, however, that the assumption that the structure-borne energy flow is governed by membrane stresses in the shell (see section 2.6.2) becomes less valid for higher order modes, so that it is preferable to use more elaborate energy flow expressions for higher order waves in a pipe, like those given by Fuller & Fahy [1982] or Pavić [1990].

Note: The two-channel equations for measuring structure-borne energy flow along pipes have been applied successfully in shipboard measurements, on a cooling water pipe of a diesel engine and on the propeller shaft (i.e. a thick-walled, air-filled pipe), see [de Jong, Verheij & Bakermans 1992; Verheij, Hopmans & Van Tol 1993].

4.2.4 non-intrusive measurement of pressure pulsations

It is of great practical interest to be able to determine pressure pulsations in a pipe from measurements at the outer surface of the pipe. Drilling holes in pipes to insert pressure transducers will in many situations be undesirable or even impossible. We have seen in chapter 2 that there is a direct relation between the internal wall pressure and the radial motion of the wall (eq.2.34). But we have also seen that the circumferential stiffness of the pipe is so high that the corresponding axial motion, due to Poisson contraction of the wall, predominates over the radial motion at low frequencies. Moreover, measurements of the $n=0$ radial acceleration will contain contributions of both fluid waves and extensional waves.

To investigate whether it is possible to separate the contributions of these two wave types in measurements of the wall motion, we will first consider one-directional propagation of coupled fluid waves and extensional waves in a semi-infinite pipe (see also [Pavić 1992; Pinnington & Briscoe 1992]). We can estimate the energy flow distribution for each wave by inserting the approximate wave velocities (eq.2.28&29) into the equations (2.34) and (2.43&44). It follows that the ratio of fluid-borne to structure-borne energy flow for the fluid wave is approximately equal to the inverse ratio for the extensional wave:

$$\frac{(\hat{P}_{zs})_F^\pm}{(\hat{P}_{zf})_F^\pm} \approx \frac{(\hat{P}_{zf})_E^\pm}{(\hat{P}_{zs})_E^\pm} \approx 4v^2 \frac{A_f \rho_f c_F^4}{A_s \rho_s c_E^4} \quad (4.21)$$

This ratio is generally small (for example: for a water-filled, steel pipe with $h/a=0.05$ the ratio equals 0.0016). Hence the energy flow in the fluid wave is mainly fluid-borne and the energy flow in the extensional wave is mainly structure-borne. The ratio of the wall displacement amplitudes corresponding to these waves depends on the ratio of the energies:

$$\frac{|W_E^\pm|^2}{|W_F^\pm|^2} \approx \frac{v^2}{4} \frac{A_s \rho_s c_E}{A_f \rho_f c_F} \frac{(\hat{P}_{zs})_E^\pm}{(\hat{P}_{zf})_F^\pm} \quad \text{and} \quad \frac{|U_F^\pm|^2}{|U_E^\pm|^2} \approx 4v^2 \frac{A_f \rho_f c_F^3}{A_s \rho_s c_E^3} \frac{(\hat{P}_{zf})_F^\pm}{(\hat{P}_{zs})_E^\pm}. \quad (4.22)$$

This implies that the fluid wave (F) predominates in the radial displacement and the extensional wave (E) predominates in the axial displacement if the energy flow distribution is even (for the above example the factors in eq.(4.19) are 0.079 and 0.0066, respectively). However, the ratio of radial amplitudes shows that an accurate measurement of the radial displacement amplitude W_F is only possible if the fluid-borne energy flow predominates over the structure-borne energy flow. The axial displacement amplitude U_E is less disturbed by the simultaneous presence of a fluid wave.

The measurement of the radial displacement amplitude by means of accelerometers has the extra difficulty of their inherent sensitivity to transverse accelerations. The ratio of axial to radial acceleration is approximately equal to

$$\frac{|W_F^\pm|^2}{|U_E^\pm|^2} \approx 4 \left(\frac{\omega a}{c_E} \right)^2 \frac{A_f \rho_f c_F}{A_s \rho_s c_S} \frac{(P_{zf})_F^\pm}{(P_{zs})_E^\pm}. \quad (4.23)$$

In the low frequency approximation that we have adopted here, the non-dimensional frequency $\omega a/c_E$ is very small. Considering that a transverse axis sensitivity of 3% is quite good for an accelerometer, it follows that the signal that is measured by a radially mounted accelerometer will only be related to the fluid wave if the energy flow in the extensional wave is negligibly small.

Note that the above considerations are based on one-directional propagating waves. In practice there will be partial standing wave patterns in pipes, due to reflections at discontinuities. This means that the ratios of wave amplitudes and wave energies will highly depend on the axial position relative to the wave field. It may be concluded that it is necessary to use a four-channel method for the decomposition of axial waves in a pipe that is filled with a heavy fluid. This method may be based on non-intrusive measurement of axial wall accelerations. It is recommended that the measurement of radial wall accelerations ($n=0$) is not adopted, since these measurements will very likely be hampered by the transverse axis sensitivity of the accelerometers. The application of a piezo-electric wire that measures circumferential strain [Pinnington & Briscoe 1992] might overcome this problem.

4.2.5 the four-channel method

We saw above that the vibro-acoustic behaviour of short pipes and of pipes with a significant Poisson-coupling is determined by groups of four coupled waves. The wave amplitudes may be obtained from four measurements, by solving eq.(4.5), where $[F]$ is a 4×4 matrix. We will illustrate this method by applying it to the experimental analysis of coupled axial waves ($n=0$) in fluid and pipe wall.

Let us first consider the application of four equal sets of transducers (e.g. pressure transducers, axially mounted accelerometers or circumferential piezoelectric wires) at four pipe cross-sections (z_1, z_2, z_3, z_4). The corresponding wave amplitudes are solved from the matrix equation

$$\begin{pmatrix} \hat{Q}_0(z_1) \\ \hat{Q}_0(z_2) \\ \hat{Q}_0(z_3) \\ \hat{Q}_0(z_4) \end{pmatrix} = \begin{bmatrix} e^{-ik_F z_1} & e^{ik_F z_1} & e^{-ik_E z_1} & e^{ik_E z_1} \\ e^{-ik_F z_2} & e^{ik_F z_2} & e^{-ik_E z_2} & e^{ik_E z_2} \\ e^{-ik_F z_3} & e^{ik_F z_3} & e^{-ik_E z_3} & e^{ik_E z_3} \\ e^{-ik_F z_4} & e^{ik_F z_4} & e^{-ik_E z_4} & e^{ik_E z_4} \end{bmatrix} \begin{pmatrix} A_F^+ \\ A_F^- \\ A_E^+ \\ A_E^- \end{pmatrix}. \quad (4.24)$$

The two axial wave types exhibit two different wave velocities (for a water-filled steel pipe with $h/a=0.05$: $c_F/c_E \approx 4.2$). Hence, on the basis of the error-sensitivity condition for the two-channel method (eq.4.8), it is suggested that the axial array of sensors should comprise two different spacings, that fulfil eq.(4.8) for both wave types. Figure 4.3 (page 74) shows the matrix condition number for a symmetrical (solid line) and an asymmetrical (dashed line) array, as a function of the array spacing in wavelengths. The ratio of the largest spacing to the shortest spacing is chosen to be equal to the ratio of the wavelengths (i.e. 4.2). A large value of the condition number indicates that the matrix is close to singular. The symmetrical array appears to be more useful, because it is better conditioned over a wider frequency range than the asymmetrical array. But still the inversion will only be reliable in limited ranges of the spacing to wavelength ratio.

The relative error in the norm of the vector of wave amplitudes will be smaller than the product of the matrix condition and the relative error in the norm of the measurement vector, see eq.(3.43). The absolute accuracy with which the four elements of the wave-number vector are determined is not equal, because they are not necessarily of equal magnitude, but rather depend on which wave type is predominant. The weaker amplitudes will become very inaccurate when they are of the same order of magnitude as the absolute error in the largest amplitude.

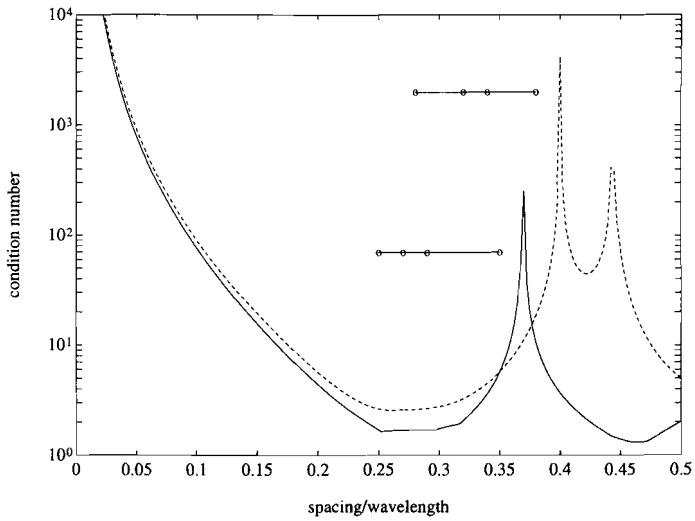


Figure 4.3: Matrix condition number for axial wave decomposition in a water-filled steel pipe ($h/a=0.05$), using a symmetrical (-) or an asymmetrical (--) array of four equal sets of transducers.

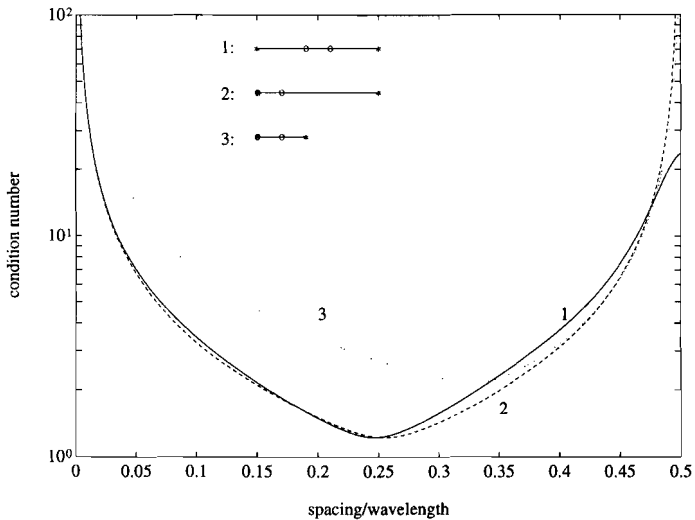


Figure 4.4: Matrix condition number for axial wave decomposition in a water filled steel pipe ($h/a=0.05$), using a hybrid array consisting of two sets of pressure transducers (o) and two sets of axial accelerometers (*): (1) symmetrical array, (2) asymmetrical array, (3) array of reduced length.

The accuracy of the decomposition may be improved by using a four-channel method, that is based on a hybrid array, for example on two axial acceleration measurements and two pressure measurements. Halkyard & Mace [1993] have shown that the same applies for bending wave decomposition on a beam. With this hybrid array the fluid wave will be characterized by a pressure and the extensional wave by an axial displacement of the wall. After scaling of the data ($\tilde{p}=p/\rho_f \check{c}_F \omega$, $\tilde{u}=-\dot{u}/\omega^2$, see eq.(3.18)), the equations of motion (2.48) lead to the following matrix equation:

$$\begin{pmatrix} \tilde{p}_0(z_1, \omega) \\ \tilde{p}_0(z_2, \omega) \\ \tilde{u}_0(z_3, \omega) \\ \tilde{u}_0(z_4, \omega) \end{pmatrix} = \begin{bmatrix} e^{-ik_F z_1} & e^{ik_F z_1} & \Psi_E e^{-ik_E z_1} & -\Psi_E e^{ik_E z_1} \\ e^{-ik_F z_2} & e^{ik_F z_2} & \Psi_E e^{-ik_E z_2} & -\Psi_E e^{ik_E z_2} \\ \Psi_F e^{-ik_F z_3} & -\Psi_F e^{ik_F z_3} & e^{-ik_E z_3} & e^{ik_E z_3} \\ \Psi_F e^{-ik_F z_4} & -\Psi_F e^{ik_F z_4} & e^{-ik_E z_4} & e^{ik_E z_4} \end{bmatrix} \begin{pmatrix} \tilde{p}_F^+ \\ \tilde{p}_F^- \\ \tilde{u}_E^+ \\ \tilde{u}_E^- \end{pmatrix}, \quad (4.25)$$

with

$$\Psi_F = \frac{\pm i \sigma \tilde{v} k_F \check{k}_F}{k_F^2 - \check{k}_E^2}, \quad \Psi_E = \frac{\mp i \tilde{v} \check{k}_F \check{k}_E^2}{k_E (k_E^2 - \check{k}_F^2)}. \quad (4.26)$$

The factors σ and \tilde{v} have been defined in eq.(3.20). The frequency-independent factors $\Psi_{F,E}$ contain both the exact solutions (k_F, k_E) of the dispersion equation (eq.3.19) and the approximate solutions (\check{k}_F, \check{k}_E) that are defined in eq.(2.28&29), because the latter are used to scale the data. Poisson coupling is responsible for the small difference between the two.

Figure 4.4 shows the condition number of the matrix for the hybrid array as a function of the spacing in wavelengths (for a water-filled steel pipe with $h/a=0.05$, i.e. $\Psi_F \approx 0.048i$ and $\Psi_E \approx -0.16i$). As in the above example the ratio of the smallest to the largest spacing is equal to the ratio of the wave velocities. The range of applicability appears to be much greater than for the array of equal sensors (fig.4.4). The matrix condition remains reasonably good, if the total length of the array is reduce to twice the fluid wave spacing. This is important for practical application, since it will not always be possible to measure on sufficiently long pipes. The symmetry appears to be unimportant for the matrix condition of the hybrid array.

Although the matrix condition number will give an indication of the frequency range in which the method is insensitive to input errors, it does not give direct information on the accuracy of the results, because this accuracy also depends on the accuracy of the measurements. The accuracy can best be evaluated by numerically disturbing the input data

with amplitude and phase errors of the same order of magnitude as the estimated input errors. The resulting variation in the wave amplitudes, or other wave field descriptors, will give a reliable indication of their accuracy. In chapter 5 we will show the application of the wave decomposition method with this accuracy estimation, applied to some laboratory experiments.

4.3 Inverse methods

We saw in chapter 3 that the vibro-acoustic transmission through each pipe system component (that behaves linearly) can be characterized by a 'passive' transfer matrix $[T]$ and, if it generates pulsations or vibrations, an additional 'active' source vector $\{Q_S\}$, so that the state vectors (eq.3.12) at its inlet and outlet are related as:

$$\{Q_o\} = [T]\{Q_i\} + \{Q_S\} . \quad (4.27)$$

Further, the boundary conditions for a fluid-filled pipe system may be expressed by means of an impedance matrix $[Z_b]$, that relates the generalized forces $\{F\}$ to the velocities $i\omega\{U\}$ (see eqs.(3.3) and (3.9)):

$$\{F_b\} = i\omega[Z_b]\{U_b\} , \quad (4.28)$$

where

$$\begin{aligned} \{F_b\} &= \{ p, F_z, F_x, M_y, F_y, M_x, M_z \}_b , \\ \{U_b\} &= \{ v, u_z, u_x, \phi_y, u_y, \phi_x, \phi_z \}_b . \end{aligned} \quad (4.29)$$

The wave decomposition method allows us to determine the state vectors $\{Q_i\}$, $\{Q_o\}$ and $\{F_b\}$ and $\{U_b\}$ from measurements in straight pipes at the inlet and outlet of a pipe system component or at the boundaries of the pipe system. The objective of the 'inverse' methods, that are considered here, is to determine the characteristic matrices and vector ($[T]$, $[Z_b]$ and $\{Q_S\}$) from these state vectors. Because the number of unknown variables (matrix and vector coefficients) is generally too large to be solved directly from eqs.(4.24) or (4.25), the inverse methods involve repeated measurements on different system configurations. The system configuration may be varied through variation of the excitation or by applying geometrical changes to the system.

To determine all elements of a 14×14 transfer matrix (or a 7×7 impedance matrix) requires at least 14 (or 7) different configurations. It is of great practical interest to establish the properties of symmetry and the absence of coupling between degrees of freedom, that

cause matrix coefficients to be equal or to vanish. A reduction of the number of unknown matrix coefficients may lead to an important reduction of the experimental effort.

NOTE: Frikha et al. [1990;1992] and Trollé et al. [1993] describe an 'inverse' method to determine boundary conditions and excitation forces in pipe systems, which is based on multiple measurements on a single piping configuration. However, no matter how many measurement points are available in the pipe system, one can only determine the state vectors at the system boundaries for this single configuration. This will only yield correct boundary conditions if there is no mutual coupling between degrees of freedom at the boundaries, i.e. if the boundary conditions can be described by a vector instead of a matrix with cross-coupling terms. This fact should be recognized as a serious limitation for application of their inverse method to practical pipe systems.

In chapter 6 we will show the application of an inverse method to characterize a centrifugal pump, with respect to the generation and transmission of fluid pulsations. A rigidly mounted pump is considered, so that the problem is reduced to the determination of 6 unknown coefficients: a 2x2 transfer matrix and 2 source vector coefficients. These coefficients can be determined from measurements on three different configurations.

Other examples of the application of inverse methods will be given in chapter 5. To illustrate the principle we will describe here the inverse method required to determine the mobility matrix that characterizes a system boundary at which pressure pulsations couple only to extensional wall vibrations. This may occur when a straight pipe is closed by means of an end plate (or a large mounting block as in the experiments that are described in chapter 5). In this case the two test configurations may be achieved by first exciting the fluid and then exciting the pipe wall in axial direction. In both configurations we can determine the state vector at the boundary, using the wave decomposition method (preferably with a hybrid array consisting of pressure transducers and axial accelerometers, see section 4.2.5). The results of measurements on the two configurations (A) and (B) can be expressed in the following matrix equation:

$$\begin{bmatrix} v^A & v^B \\ u_z^A & u_z^B \end{bmatrix} = \frac{1}{i\omega} \begin{bmatrix} Y_{vp} & Y_{vF} \\ Y_{up} & Y_{uF} \end{bmatrix} \begin{bmatrix} p^A & p^B \\ F_z^A & F_z^B \end{bmatrix}, \quad (4.30)$$

The mobility matrix [Y] may be derived from this equation as will be shown in section 5.2.3.

4.4 Conclusion

Because of the complex vibro-acoustic behaviour of fluid-filled pipe systems it is not easy to interpret the results of pressure or acceleration measurements in such systems. In this chapter we have described methods to extract useful information out of this type of measurements. It has been shown how the amplitudes of the individual waves that propagate simultaneously in the pipe can be determined on the basis of measurements with appropriate arrays of transducers. Further a description has been given of how one can determine the transfer matrix of a pipe system component, the mobility matrix at a pipe cross-section, or the source strength vector of a component that generates pulsations or vibrations, using an 'inverse' method on the basis of repeated measurements on different system configurations. Practical aspects of the methods that have been described here will be discussed further in the next chapters in relation to application of the methods to laboratory experiments.

5. VALIDATION EXPERIMENTS

5.1 Introduction

In the previous chapters methods have been developed to predict and to analyze theoretically and experimentally the coupled pulsations and vibrations in a fluid-filled pipe system. This chapter describes the results of a practical application of these methods.

To facilitate the interpretation of the results, it was decided to test the methods on some simple laboratory test arrangements. The aim of the experiments was both to validate the theoretical description of the vibro-acoustic behaviour of some pipe system components and to test the applicability of the measurement methods.

The first set of experiments validates the model for wave propagation in a straight pipe (section 5.2). It is shown that an inverse method can be applied to determine the boundary conditions. The next two sets of experiments were designed to verify the transfer matrix model for the elbow (section 5.3) and to measure the reflection and transmission characteristics of a rubber bellows (section 5.4).

5.2 A straight pipe

The axial wave decomposition techniques of section 4.2 rely on an appropriate model for the wave propagation in a straight fluid-filled pipe. Therefore this model can be validated by applying the wave decomposition technique to a set measurements on a straight pipe and comparing the results with the results of additional measurements.

5.2.1 test arrangement and instrumentation

Figure 5.1 shows a sketch of the first test arrangement. It consists of a 1.45 m long, stainless steel pipe with an outer diameter of 159 mm and a wall thickness of 4.5 mm, filled with water. Table 5.1 gives an overview of the material parameters that are used for this pipe and some relevant secondary parameters, like cut-on frequencies and wave velocities (see the List of Symbols). The accuracies in table 5.1 are based on the estimated accuracy of the primary parameters ($a_i, h, E_s, \rho_s, \nu, K_f, \rho_f$). The cut-on frequency for the $n=2$ lobar waves (f_{c2}) has been experimentally determined as 387 Hz ($\pm 0.6\%$), a value that deviates by only 3% from the above estimate. This indicates that the real accuracy is probably better than the estimates in table 5.1 suggest. Note that the approximate axial wave velocities (\tilde{c}_F and \tilde{c}_E) agree very well with the exact solutions of the equations of

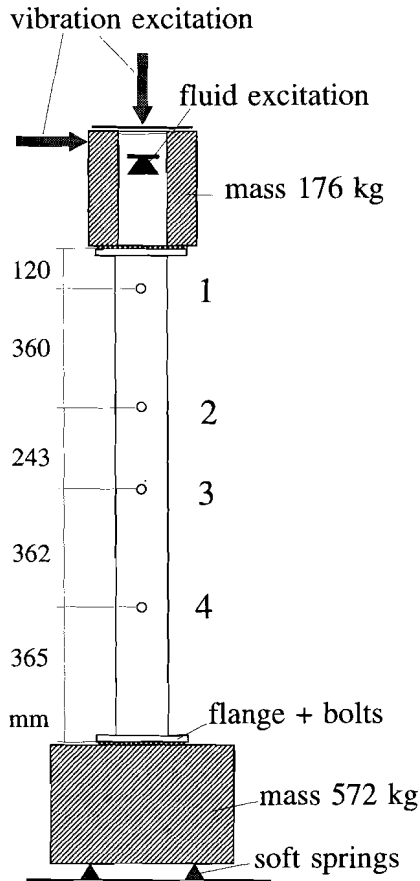


Figure 5.1: straight pipe test arrangement, see also the annotations in the text.

$a_i = 75 \text{ mm } (\pm 1\%)$	$E_s = 2.1 \cdot 10^{11} \text{ N/m}^2 (\pm 7\%)$	$K_f = 2.15 \cdot 10^9 \text{ N/m}^2 (\pm 2\%)$
$h = 4.5 \text{ mm } (\pm 2\%)$	$\rho_s = 7800 \text{ kg/m}^3 (\pm 1\%)$	$\rho_f = 1000 \text{ kg/m}^3 (\pm 0.1\%)$
$\beta^2 = 0.28 \cdot 10^{-3} (\pm 6\%)$	$\nu = 0.3 (\pm 3\%)$	
$f_{c2} = 374 \text{ Hz } (\pm 8\%)$	$c_p = 5439 \text{ m/s } (\pm 4\%)$	$c_a = 1466 \text{ m/s } (\pm 1\%)$
$f_{c3} = 1123 \text{ Hz } (\pm 8\%)$	$f_{\text{ring}} = 11.2 \text{ kHz } (\pm 5\%)$	$f_c = 5.7 \text{ kHz } (\pm 2\%)$
$\check{c}_F = 1271 \text{ m/s } (\pm 2\%)$	$\check{c}_E = 5189 \text{ m/s } (\pm 4\%)$	$\check{c}_B = 14.09\sqrt{\omega} \text{ m/s } (\pm 4\%)$
$c_F = 1259 \text{ m/s } (\pm 2\%)$	$c_E = 5259 \text{ m/s } (\pm 4\%)$	$c_B \approx 13.26\sqrt{\omega} \text{ m/s } (\pm 4\%)$

Table 5.1: parameters for the straight, water-filled, stainless steel pipe.

motion (c_F and c_E). The velocity of the propagating bending wave (c_B) is 6% lower than the Euler-Bernoulli beam bending wave velocity (\check{c}_B), which is due to effects of transverse shear and rotational inertia.

The pipe has been mounted vertically, to allow air to escape from the water. The presence of small air bubbles will considerably decrease the effective compressibility of the water, and hence have a significant influence on the acoustics of the system. In spite of the vertical arrangement it took about five days for the system to stabilize after filling it up with tap water. This problem might be overcome by pressurizing the system. The pipe is mounted on a mass-spring system to decouple its vibrations from the floor of the building. The resonance frequency of the system on the bottom springs is about 10 Hz so that it may be assumed that the bottom mass moves freely in the frequency range where the measurements have been performed (50-1000 Hz). In this frequency range the (steel) bottom mass behaves as a rigid body. Excitation takes place at the top of the system. The fluid is excited by an underwater loudspeaker (*Aquavox*). To avoid a direct excitation of the pipe wall by the hydrodynamic nearfield of the loudspeaker it is suspended in an annular mass (176 kg) for which the circumferential stiffness is 13 times larger than for the pipe. The fluid is free at the top surface. An electrodynamic shaker (*Derritron VP4*) is used to excite system vibrations in axial or transversal direction. The pipe is flanged at both ends and connected to the top and bottom masses by means of four bolts. The connections are sealed by rubber gaskets.

Pressure pulsations are measured by four piezo-electric pressure transducers (*Birchall DJB/M02/TA*), that are flush mounted in the pipe wall at four axial positions, as indicated in figure 5.1. A single pressure transducer has been used per cross-section. This means that the contributions of the different waves to the measured pressures cannot be distinguished. However, the selective excitation, that is either axial ($n=0$) or transversal ($n=1$) prevents problems in the interpretation. Pipe wall accelerations are measured by an array of four accelerometers (*B&K 4382*) per pipe cross-section. These accelerometers are mounted on the pipe wall in either axial or radial direction by means of aluminium studs, see fig.4.1, to perform the circumferential mode decomposition that has been described in section 4.2.1.

The sources are driven with a periodically swept sine signal (from 50 to 1000 Hz in 0.5 s) that is generated by a digital waveform generator (*Wavetek 95*). The signals of pressure transducers and accelerometers are recorded by a four channel FFT analyzer (*Scientific Atlanta SD380C*). Averaged auto- and cross-power spectra (400 lines, $\Delta f=2.5$ Hz, 100 averages, Flat top window) are determined. The spectra are transferred from the analyzer to a PC, where they are processed using *MATLAB* software. The software has been tested by application to data that were generated by the *PRESTO* computer program.

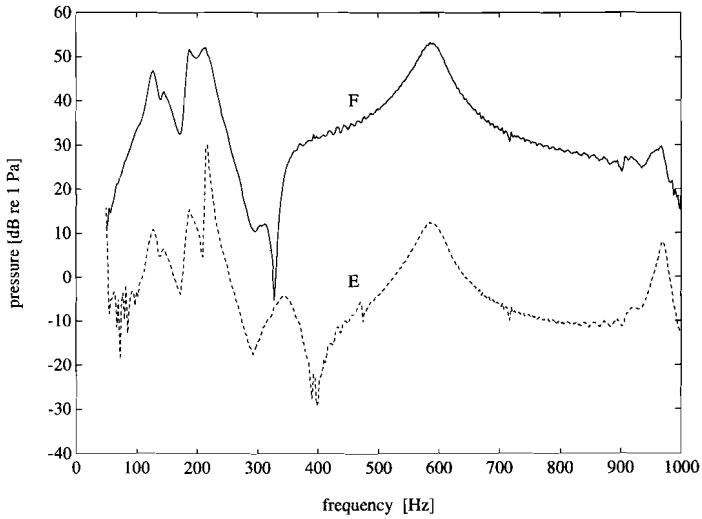


Figure 5.2a: spectra of the fluid (F) and extensional (E) wave contributions to the pressure at position '2' in the straight pipe, for fluid excitation.

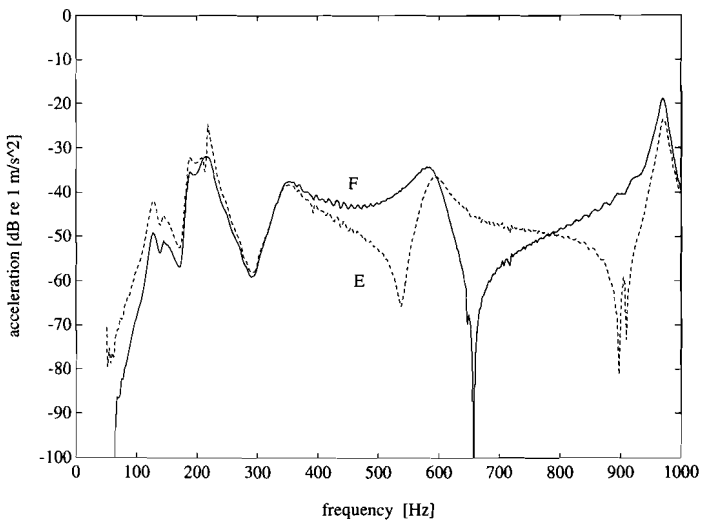


Figure 5.2b: spectra of the fluid (F) and extensional (E) wave contributions to the axial wall acceleration at position '2' on the straight pipe, for fluid excitation.

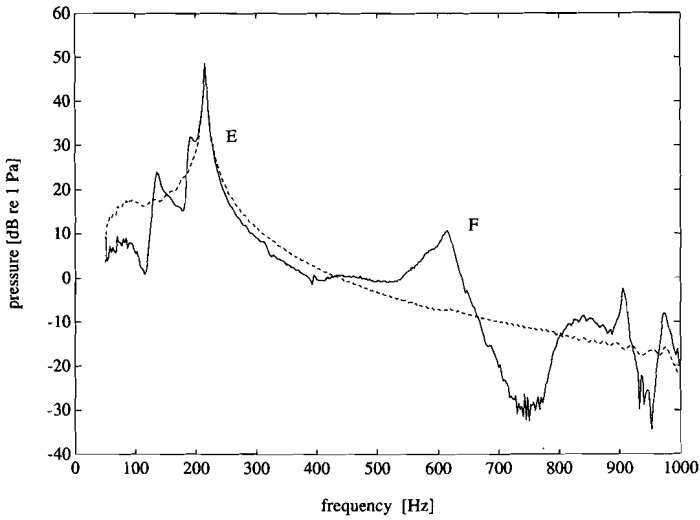


Figure 5.3a: spectra of the fluid (F) and extensional (E) wave contributions to the pressure at position '2' in the straight pipe, for axial vibration excitation.

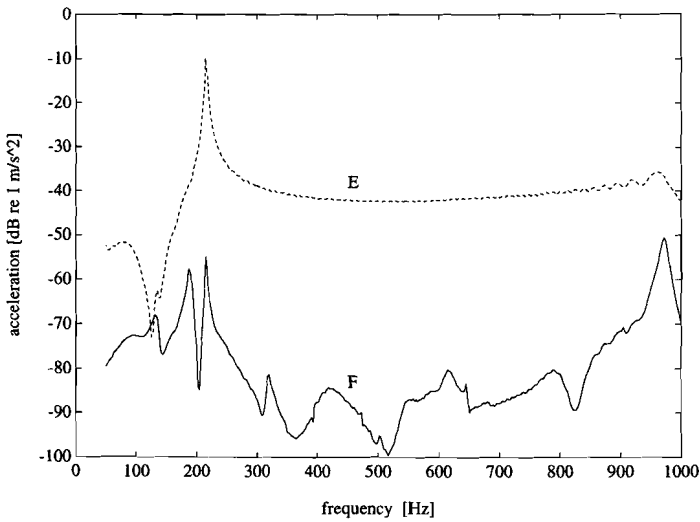


Figure 5.3b: spectra of the fluid (F) and extensional (E) wave contributions to the axial wall acceleration at position '2' on the straight pipe, for axial vibration excitation.

5.2.2 axial wave decomposition

The test arrangement exhibits two mechanisms of interaction between fluid pulsations and axial pipe wall vibrations: 'junction coupling' at the bottom mass and 'Poisson coupling' in the straight pipe. Consequently, fluid waves and extensional waves will propagate simultaneously in the pipe, both when the fluid is excited and when the wall is excited in axial direction. This situation is suitable for testing the four-channel method for axial wave decomposition that has been described in section 4.2.5.

Two successive measurements have been performed. First the system was excited by the underwater loudspeaker, then by the axial shaker. The axial waves have been decomposed by means of the hybrid four-channel method of eq.(4.21), using the pressure transducers at positions 1 and 3 and the axial accelerometers at positions 1 and 4 (see fig.5.1). A perturbation of 1% and 1° has been applied to the measured input data to investigate the error sensitivity of the method. The perturbed data caused a deviation of less than 5% in all four wave amplitudes.

Figures 5.2 and 5.3 show the results of the decomposition for the two measurements. These curves show the total contribution of both wave types to the pressure and the axial acceleration at position 2 in the pipe. The complex amplitudes of the corresponding waves that are propagating in positive and negative axial directions have been added to obtain these spectra. In section 5.2.6 the shape of the spectra will be discussed, here we consider the wave decomposition. It is clear that the wave type that is directly excited predominates, that is the fluid wave when the fluid is excited (fig.5.2a) and the extensional wave when the shaker is used (fig.5.3b). This means that these waves could be treated with a two-channel method. The indirectly excited spectra (fig.5.2b and 5.3a), however, show contributions of both wave types that are of the same order of magnitude. This means that, for the indirectly excited waves, the application of a two-channel method would lead to large errors in the interpretation. This experiment confirms that it is valuable to apply a four-channel method for axial wave decomposition if the excitation mechanism is not known a priori.

NOTE: the effect of Poisson coupling on the accuracy of the two-channel method for the experimental determination of vibro-acoustic energy flow in this experiment has been presented at the 4th international congress on intensity techniques in Senlis [de Jong & Verheij 1993]. It was concluded that the coupling will cause the measurement of the energy flow in the indirectly excited waves to be unreliable.

The quality of the model for the coupled axial wave propagation may best be tested by looking at the indirect excitation. The pressure at position 2 can be predicted from the wave decomposition, for the experiment with axial vibration excitation, by summation of the two wave contributions that are shown in figure 5.3a. This predicted pressure spectrum may be compared with the measured pressure spectrum, see figure 5.4. Note that the measured pressure p_2 has not been used in the wave decomposition. To show the importance of Poisson contraction the wave decomposition has been repeated while neglecting the Poisson coupling (using $\nu=0$). The pressure spectrum that is predicted on the basis of this assumption is given by the dash-dotted line in figure 5.4. It is clear that the predicted spectrum without Poisson coupling is less accurate than the result of the model that takes the Poisson coupling into account. The model with $\nu=0$ predicts a pressure cancellation near 500 Hz that is not seen in the direct measurement. The agreement between the directly measured spectrum and the prediction that includes the effect of Poisson coupling is good, at least up to 750 Hz. Apparently the low-frequency model loses its validity above 750 Hz. This shows that the model is still correct far above the cut-on frequency of $n=2$ waves ($f_{c2}=374$ Hz). This comparison demonstrates that the model gives a reliable description of the propagation and coupling of fluid waves and extensional waves in a straight pipe. Of course the effect of Poisson coupling will be smaller in practical pipe systems where junction coupling (e.g. in elbows) is more important. But even then Poisson coupling may be responsible for a coherent noise in single-channel or two-channel measurements, that can be suppressed by a four-channel method.

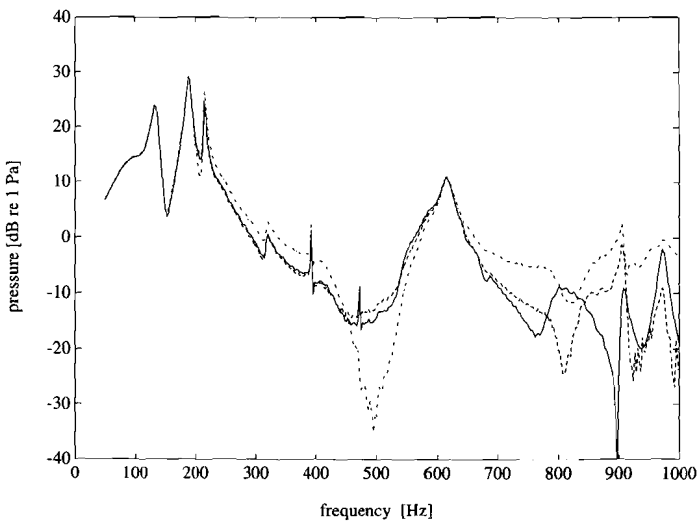


Figure 5.4: pressure spectrum at position '2', caused by axial vibration excitation, directly measured (-) and determined by wave decomposition, for $\nu=0.3$ (--) and $\nu=0.0$ (-.).

5.2.3 axial mobility matrix at the bottom mass

Fluid-structure interaction takes place by Poisson coupling in the straight pipe and by 'junction' coupling at the bottom mass. It has been shown above that the Poisson coupling is described accurately in the model on which the axial wave decomposition method is based. In this section the junction coupling is investigated. The boundary conditions at the interface ($z=0$) of a fluid-filled pipe and a massless endplate have been given in section 3.6.1. With introduction of a mass M in place of the end plate these boundary conditions become:

$$v(0) = u_z(0) , \quad A_f p(0) = F_z(0) + M\omega^2 u_z(0) . \quad (5.1)$$

The boundary conditions at the bottom mass are further complicated because the pipe is connected to the mass via a finite stiffness S . Here S denotes the axial stiffness of the bolts, which cannot be neglected in comparison with the axial stiffness of the pipe. Additionally, the rubber gaskets, which seal the connection, may expand under influence of the fluid pressure. This effect may be described by a 'distensibility' parameter D , which introduces an effectively increased compressibility of the fluid (see e.g. Lighthill [1978]). Neglecting the mass of the flange and the bolts, the following boundary condition matrix may be derived to describe the coupling effects at the bottom mass. It may be expressed as a mobility matrix $[Y_{BM}]$, that relates the axial velocities of fluid and wall to the axial force and fluid pressure.

$$\begin{pmatrix} v(0) \\ u_z(0) \end{pmatrix} = \frac{[Y_{BM}]}{i\omega} \begin{pmatrix} A_f p(0) \\ F_z(0) \end{pmatrix} \approx \begin{bmatrix} -\frac{1}{M\omega^2} - D & \frac{1}{M\omega^2} \\ -\frac{1}{M\omega^2} & \frac{1}{M\omega^2} - \frac{1}{S} \end{bmatrix} \begin{pmatrix} A_f p(0) \\ F_z(0) \end{pmatrix} . \quad (5.2)$$

It has been shown in section 4.3 that the mobility matrix $[Y_{BM}]$ can be determined from two measurements on two different configurations. These are available in form of the experiments with fluid excitation and axial vibration excitation that have been described in the previous section. Figure 5.5 shows the resulting spectra of the magnitude of the four matrix coefficients. These results may be compared with the simple model of eq.(5.2). As indicated by the model reciprocity requires that the cross-mobilities Y_{vF} and Y_{up} are equal. Figure 5.5 shows that this condition is fulfilled at frequencies below 550 Hz. Apparently the results are less accurate at highre frequencies. Below 150 Hz these cross-mobilities follow a mass curve (for a mass of 580 kg) as predicted by eq.(5.2). Above this frequency the mobility curves deviate from the simple model. In reality there may, for example, be cross-coupling due to Poisson contraction of the gasket, that is not included in the model. The fluid mobility Y_{vp} deviates from the cross-mobilities, which shows that there is indeed a distensibility effect. The structural mobility Y_{uF} shows a minimum at 400 Hz. Such a minimum will occur at the resonance frequency ($\omega^2=S/M$) of the mass-spring system in

eq.(5.2). Hence the axial stiffness of the bolted connection between pipe and bottom mass is about equal to $S \approx 3.7 \cdot 10^9$ N/m. This value is not far below the estimated axial stiffness $S \approx 5.5 \cdot 10^9$ N/m of the bolts (four steel rods of 30 mm length and 16 mm diameter).

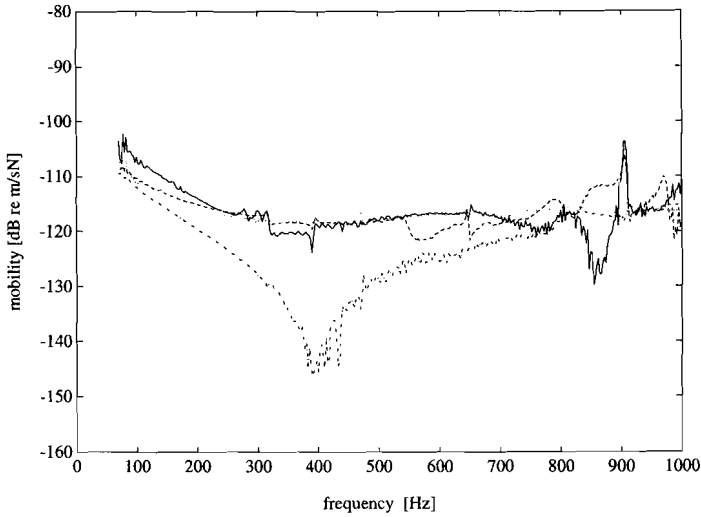


Figure 5.5: spectra of the four components of the experimentally determined mobility matrix $[Y_{BM}]$ for the bottom mass: Y_{vp} (-), Y_{vF} (--), Y_{up} (..) and Y_{uF} (-.).

This experiment clearly demonstrates that it is possible to determine a mobility matrix on the basis of experimental wave decomposition in a pipe using different configurations of the system, although further investigations are required to establish the accuracy of the method. This inverse method is a valuable tool for laboratory experiments, for example to characterize pipe system components. It remains to be shown whether such a method can be applied to determine larger mobility matrices, that describe system boundaries at which more degrees-of-freedom are coupled. For example, the mobility matrix of a pipe elbow will have to describe a coupling between axial and transverse motion.

5.2.4 transverse wave decomposition

The decomposition of bending waves and nearfields has been studied in a third experiment. The shaker has been moved to provide transverse excitation of the top mass. The underwater loudspeaker has been removed from the water. The $n=1$ accelerations are determined at four positions (see fig.5.1), in each case by taking the difference of the signals of two accelerometers that are radially mounted in the plane of excitation at opposite sides of the pipe (q_A and q_C in figure 4.2a). These four acceleration signals allow the amplitudes of the two propagating bending waves and the two bending nearfields in the pipe (see figure 5.6)

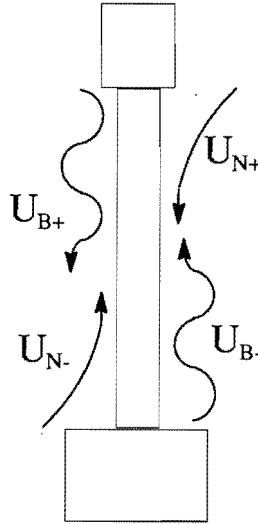


Figure 5.6: schematic representation of the four bending ($n=1$) waves in the straight pipe.

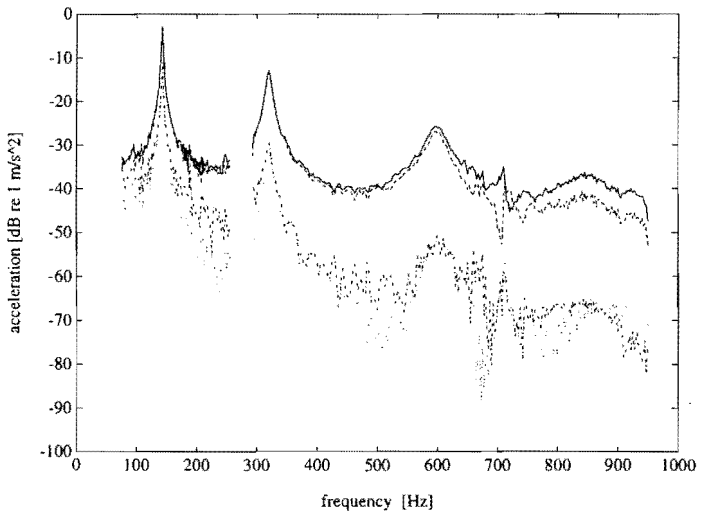


Figure 5.7: spectra of the four bending wave amplitudes at position '3' in the straight pipe: \ddot{U}_{B+} (-), \ddot{U}_{B-} (--), \ddot{U}_{N+} (..) and \ddot{U}_{N-} (-.).

to be determined, using a four-channel method. Figure 5.7 shows the resulting wave amplitudes, at position 3 in the pipe. No data are given between 250 and 290 Hz, because the measured spectra were disturbed by noise in this frequency range. The error sensitivity of the dominating wave amplitudes was found to be small. The perturbation of the input data with 1% and 1° resulted in a maximum error of 2% in the propagating wave amplitudes. The nearfield amplitudes show errors up to 35% at frequencies where they are much smaller than the bending wave amplitudes, but remain within 10% at other frequencies. As expected, the contribution of the nearfields to the wave field diminishes at higher frequencies. In the frequency range where the accelerometers are at least a half bending wavelength from the ends of the pipe the axial wave decomposition can also be performed by a two- or three-channel method.

5.2.5 internal wall pressure caused by transverse acceleration

Another interesting result of this experiment is the confirmation that transverse accelerations of the pipe generate pressure fluctuations at the pipe wall. Equation (2.36) states that the internal wall pressure for $n=1$ waves is caused by the inertance of the internal fluid. The wall pressure has been measured with pressure transducers that are positioned at 45° relative to the excitation direction. Hence these transducers measure a component of the fluid inertia force:

$$p_{n=1} = \rho_f \ddot{u}_x \sin(\pi/4) . \quad (5.3)$$

Figure 5.8 shows the comparison of the directly measured pressure spectrum and the pressure spectrum that is derived from the decomposed $n=1$ transverse acceleration, using eq.(5.3). Generally the agreement is seen to be good. The deviations at 175, 530 and 900 Hz are due to plane wave resonances in the fluid column, see section 5.2.6. Although the model of chapter 2 does not describe a coupling between the $n=1$ and $n=0$ pressure pulsations in a straight pipe, small irregularities in the test arrangement may be responsible for the observed excitation of plane waves.

Two important conclusions follow from this comparison. The first is that transverse vibrations of a fluid-filled pipe may contribute to the internal wall pressure that is measured with a flush mounted pressure transducer. This implies that it may be necessary to use more than one pressure transducer per pipe cross-section, to separate the contributions of pressure waves and pipe vibrations. This technique has been applied for the source characterization that is described in chapter 6. Another option is to use a hydrophone that is positioned at the centre of the pipe cross-section, but such a hydrophone would be difficult to position and it would disturb the flow in the pipe. Secondly it may be concluded that small irregularities in a pipe system will cause most resonant modes of a pipe system to be excited. This conclusion is illustrated by the presence of fluid column

resonances in the laboratory experiment, where they were not expected because the excitation was purely transverse.

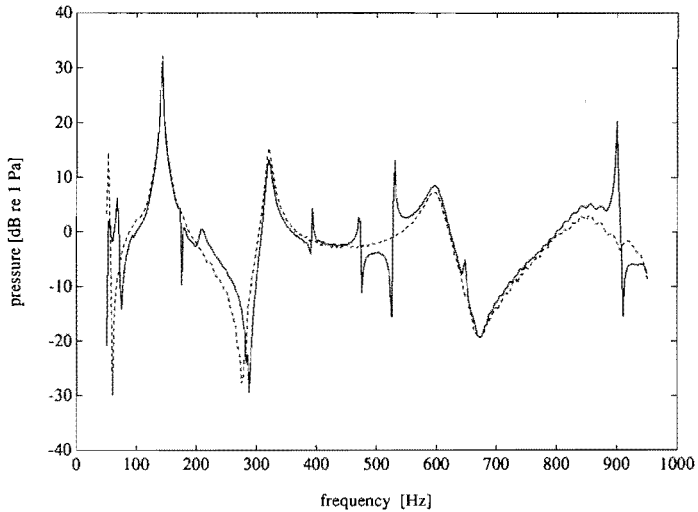


Figure 5.8: measured pressure spectrum at position '2' (-), caused by transverse excitation, compared with the predicted pressure (--) on the basis of the measured transverse acceleration spectrum, eq.(5.3).

5.2.6 comparison with *PRESTO* calculations

The program *PRESTO* has been used to determine the vibro-acoustic response of the test rig. The transfer matrix model consisted of the following components:

- an annular mass, modelled as a thick-walled, steel, fluid-filled pipe
- an in-line stiffness, representing the bolted connection of pipe and mass
- a flange, modelled as a short, thick-walled pipe
- the straight fluid-filled pipe
- a second flange, equal to the first
- a second in-line stiffness, equal to the first
- a bottom mass, with boundary conditions (eq.5.1) for the fluid

The fluid column has a free surface at the top ($p=0$). The bottom and top masses are assumed to be free to move. The rubber mounting blocks of the test rig are neglected, because the system response is determined in a frequency range (50-1000 Hz) that is far above the resonance frequency (10 Hz) of the system on these springs. The data for the

straight pipe are given in table 5.1. The internal radius of the steel top mass is somewhat smaller than the internal radius of the pipe ($a_1=70$ mm), its thickness is 90 mm and its length is 348 mm. The transfer matrix for the in-line stiffness contains the following coefficients that are estimated for the four steel bolts: an axial stiffness $S_z=5.5 \cdot 10^9$ N/m, a shear stiffness $S_t=0.9 \cdot 10^9$ N/m and a rotational stiffness $S_r=22 \cdot 10^6$ Nm, all with a loss factor 0.1. It also contains a fluid distensibility due to the rubber gasket $D=0.9 \cdot 10^{12}$ Pa/m. It is assumed that these values are independent of frequency. The steel flanges have a thickness of 65 mm and an axial length of 22 mm. The bottom mass (577 kg) has a transverse moment of inertia $I=17.1$ kg/m² and a polar moment of inertia $J=20.4$ kg/m². It is important to note that the input parameters for the *PRESTO* calculations are estimated a priori and that no attempt has been made to 'tune' the model on the basis of the experimental results.

Three calculations have been performed, with excitations that correspond with the three experiments that have been described in the previous sections. In the first calculation the underwater loudspeaker has been represented by an ideal, frequency-independent pressure source ($\Delta p=60$ Pa), that is positioned just below the free surface of the fluid. This assumption has to be taken for lack of information about the source-strength and the internal impedance of the loudspeaker. Consequently it is likely that the system response will not be predicted correctly. Figure 5.9 shows the measured and calculated pressure spectra at position 1 in the straight pipe. It is clear that the loudspeaker has a significant influence on the sound field. The most striking effect is the enormous overestimation of the pressure level at the resonances in the calculation. Obviously the loudspeaker exhibits a complex impedance that is responsible for a shift in the resonance frequencies and for a significant damping. In the calculation the fluid pulsations are only damped via coupling to mechanical vibrations, that are damped by a material loss factors of 0.002 for the pipe and 0.1 for the connections. The three resonance frequencies that are calculated are close to the lowest three eigen-frequencies of a fluid column with open-closed boundary conditions. The measurements show resonance frequencies that are 8 to 9% higher. Because the loudspeaker is mounted in a box that may contain some air, it can impose a free boundary condition at its surface. Then the effective length of the fluid column is smaller, which accounts for the increased resonance frequencies. The pressure spectrum shows minima at frequencies where the distance between the bottom mass and the measurement position is equal to one or three quarters of a wavelength of the fluid wave. These frequencies, that are independent of the source impedance, are shown to be predicted very accurately. This confirms that the deviation between the calculated and the measured spectra is due to the unknown source characteristics only. Figure 5.10 shows an indirect response: the axial acceleration spectrum at position 1 for fluid excitation. This indirect response is determined by the ratio of the contributions of fluid-borne and structure-borne waves.

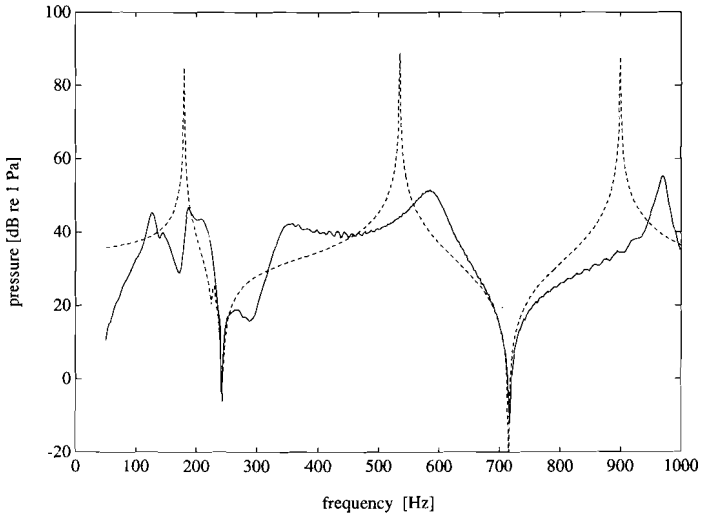


Figure 5.9: measured (-) and calculated (--) pressure spectra at position '1' in the straight pipe, for pressure excitation.

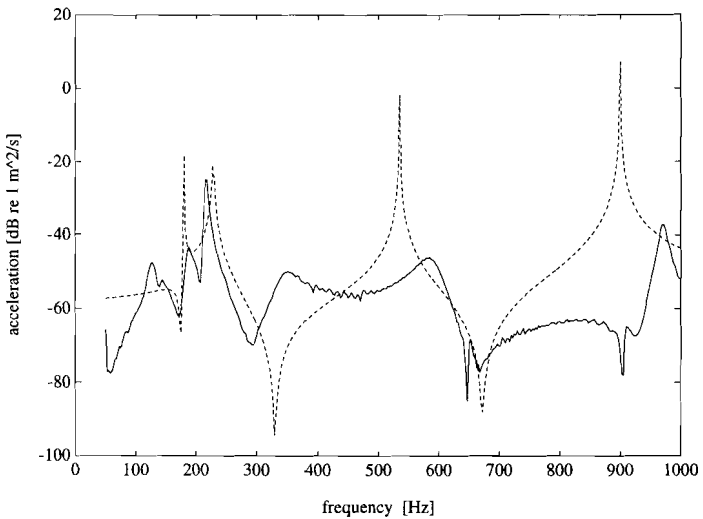


Figure 5.10: measured (-) and calculated (--) spectra of the axial acceleration at position '1' in the straight pipe, for pressure excitation.

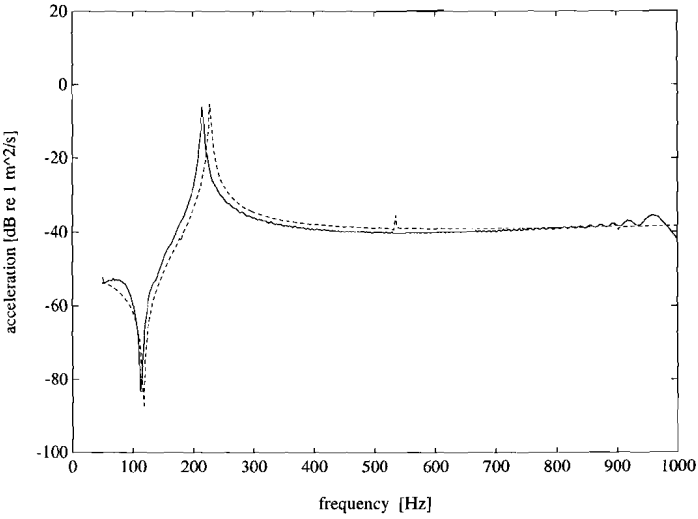


Figure 5.11: measured (-) and calculated (--) spectra of the axial acceleration at position '1' on the straight pipe, for axial vibration excitation.

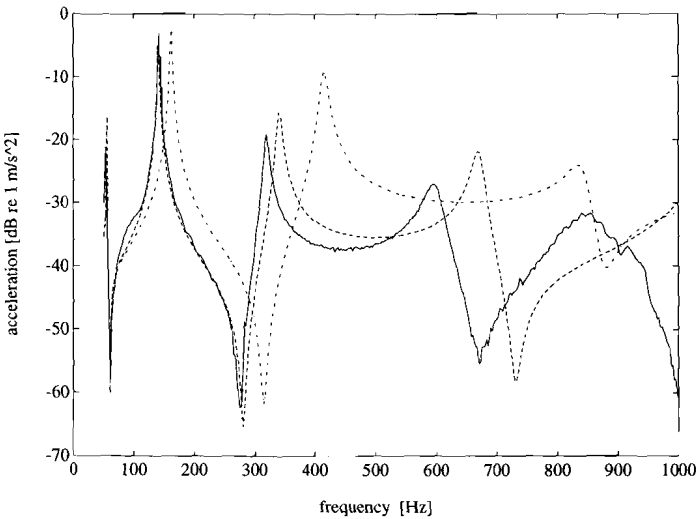


Figure 5.12: measured (-) spectrum of the transverse acceleration at position '1', for transverse excitation, compared with calculated spectra, for a pipe (--) and for a thin beam (Euler-Bernoulli) (-.).

The overestimation of the fluid pressures therefore leads to an overestimation of the acceleration levels. These results show that it is difficult to get an accurate estimation of the levels of vibration and pulsation in a pipe system if the boundary conditions cannot be determined accurately.

A second calculation has been performed with axial force excitation of the top mass. The input impedance of the shaker is negligibly small compared with the impedance of the system. The excitation force is nearly constant in the frequency range of excitation (50-1000 Hz). Figure 5.11 shows the measured and calculated acceleration spectra at position 1 for this configuration. The spectrum shows a single resonance just above 200 Hz. This lowest mode of the system may be described as the resonance of a mass-spring system, with the top mass as mass and the pipe as spring. The small difference between the measured and calculated resonance frequencies is probably due to the error in the estimated stiffness of the bolt connections. The minimum in the acceleration spectrum corresponds to the bottom mass vibrating on the stiffness of the pipe.

Finally the response of the system to transversal force excitation has been calculated. The result of this calculation is compared with the result of measurements in figure 5.12. The solid line shows the measured transverse acceleration spectrum at position 1. The dashed line gives the result of the *PRESTO* calculation at the same position. The calculated resonance frequencies are too high (about 6% at 320 Hz and about 12% at 600 Hz), but the shape of the spectrum is predicted well. The dash-dotted curve gives the result of a calculation with a thin beam model (Euler-Bernoulli) for the pipe. Its large deviation shows that it is necessary to include transverse shear and rotatory inertia for this pipe, because the ratio of length to diameter is only 10 and the wavelength is of the order of magnitude of the pipe length. Figure 5.13 shows the mode shapes that correspond to the resonance frequencies. Only the displacement and the deformation of the pipe and the two masses are shown, the flange connections are omitted from these plots. It can be seen that the rotational stiffness of the connection of the top mass to the pipe is very important for the highest mode. This increases the plausibility of the suggestion that the resonance frequency of this mode is overestimated due to an inaccurate estimate of this stiffness.

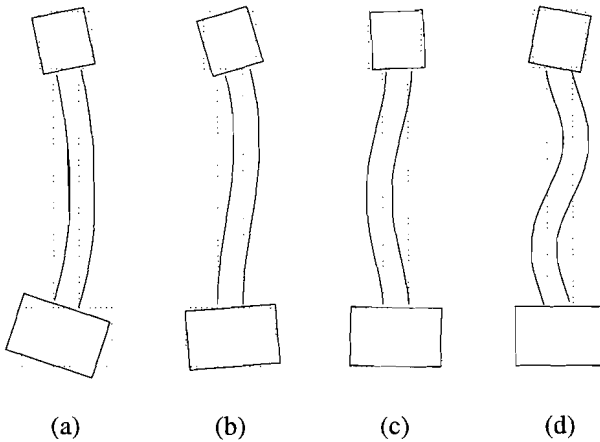


Figure 5.13: calculated mode shapes corresponding to the resonance frequencies in figure 5.12: (a) 55 Hz, (b) 140 Hz, (c) 340 Hz and (d) 670 Hz.

5.3 A pipe system with a 90° elbow

Following the straight pipe experiments, experiments have been performed on a pipe system with a 90° elbow. The objective of these experiments was to compare the results of *PRESTO* calculations with experimental observations.

5.3.1 test arrangement

The test arrangement consists of the components of the straight pipe arrangement studied above, extended with an extra, identical straight pipe and a 90° elbow, see figure 5.14. The system rests on three rubber isolators. One isolator is placed under the bottom mass, the other two isolators support the top mass. The rigid body resonance of the system on these isolators occurs below 1 Hz, so that they may be neglected in the calculations of the system response. The elbow has a radius of curvature $R=0.239$ m and it has a circular cross-section. It is flanged and connected to each pipe by means of 8 bolts. The connections are sealed with rubber gaskets. Four measurement positions are available, at which pressure pulsations and accelerations have been measured. As in the straight pipe experiment, measurements have been performed with a single pressure transducer and a set of four accelerometers per cross-section. The accelerometers have been mounted in different directions to determine axial, transverse and rotational acceleration of the pipe (see also

section 5.2.1). The structure has been excited by a shaker at the top mass, mounted in each of the three orthogonal directions. The excitation force was measured with a force transducer (*B&K 8200*). The excitation signal consisted of a periodically swept sine (20-600 Hz). Pressure and acceleration cross-power spectra (400 lines, $\Delta f=1.25$ Hz, 100 averages, flat top window) have been recorded, with the signal of the force transducer as a reference.

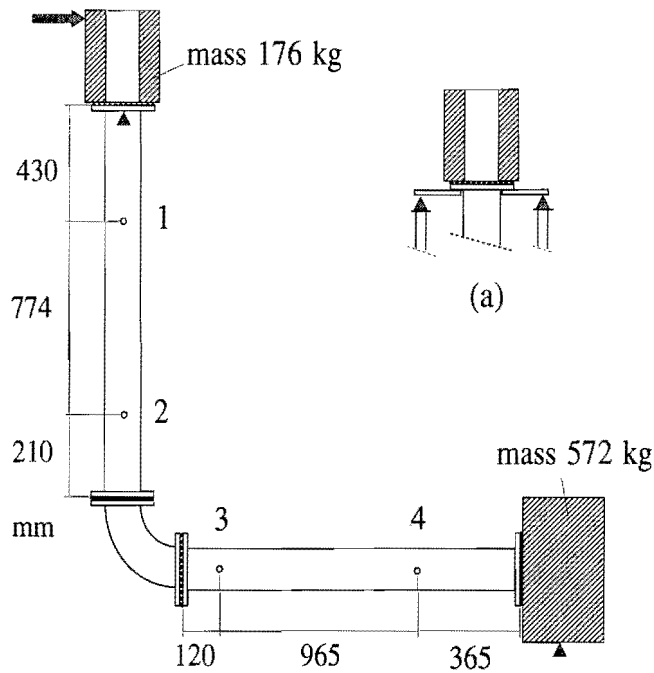


Figure 5.14: test arrangement with a 90° elbow, see also the annotations in the text. (a) the supports of the top mass, out of the plane of the elbow.

5.3.2 comparison with *PRESTO* calculations

The program *PRESTO* has been used to determine the vibro-acoustic response of the test rig. The transfer matrix model consists of the following components:

- an annular mass, modelled as a thick-walled, steel, fluid-filled pipe
- an in-line stiffness, representing the bolted connection of pipe and mass
- a flange, modelled as a short, thick-walled pipe
- a straight fluid-filled pipe

- a second flange, equal to the first
- a second in-line stiffness, equal to the first
- a third flange, equal to the first
- a 90° elbow
- a fourth flange, equal to the first
- a third in-line stiffness, equal to the first
- a fifth flange, equal to the first
- a straight pipe, equal to the first
- a sixth flange, equal to the first
- a fourth in-line stiffness, equal to the first
- a bottom mass, with boundary conditions (eq.5.1) for the fluid

The fluid column has a free surface at the top ($p=0$). The bottom and top masses are assumed to be free to move. The stiffness of the connection of the flanges at the elbow is assumed to be equal to the stiffness of the connections to the masses. The number of bolts at the elbow is twice the number of bolts at the masses, but this is compensated by the fact that the free length of the bolts is also twice as large. The parameters of most components have been discussed in section 5.2.6, only the elbow is new. Material, radius and wall thickness of the elbow are the same as for the straight pipe. Both the discrete and the continuous model have been used to calculate the system response. These models share the same flexibility factor to describe the reduced bending stiffness of the elbow. The flexibility factor is not very large because the flanges suppress ovalization of the elbow. The appropriate factor ($\beta=2.8$) is found from [ASME 1992].

As an example, figure 5.15 compares the measured and calculated response spectra at position 3 for transverse excitation of the top mass in the plane of the elbow. The four figures show the axial, transverse and rotational accelerations and the fluid pressure respectively. The rotational accelerations are measured at a radius b , see figure 4.1. The measured and calculated data are scaled with the measured excitation force. Both the response that has been obtained with the discrete model for the elbow (dashed lines) and the response for the continuous model (dash-dotted lines) are shown. The difference between the two elbow models appears to be small. On the basis of this experiment it cannot be decided which model is best. Apparently both simplified descriptions for the elbow are satisfactory. The calculated and measured spectra deviate at higher frequencies. This is not surprising since the straight pipe experiments showed a similar deviation, due to inaccurate modelling of the boundary conditions. Although the shape of the spectra is predicted correctly, the predicted vibration levels are significantly higher than the measured levels, especially at resonance frequencies. This means that the actual damping in the system is higher than assumed in the calculations. The predominant losses occur at the

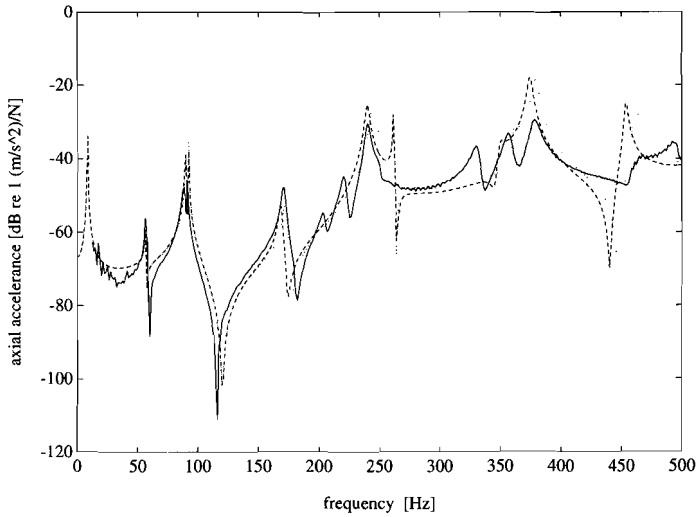


Figure 5.15a: axial acceleration at position '3' for transverse excitation in the plane of the elbow: measured (-) and calculated with the discrete model for the elbow (--) and with the continuous model (..).

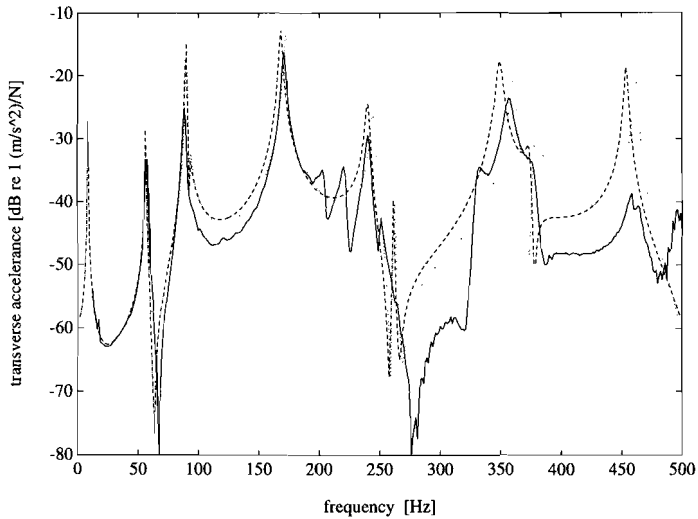


Figure 5.15b: transverse acceleration at position '3' for transverse excitation in the plane of the elbow: measured (-) and calculated with the discrete model for the elbow (--) and with the continuous model (..).

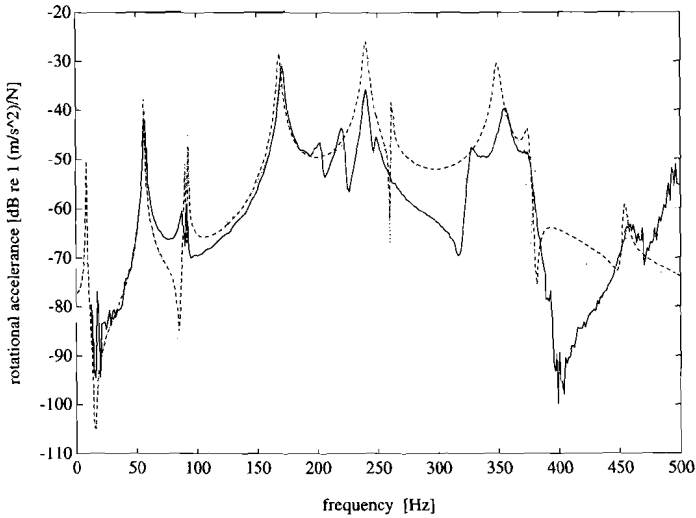


Figure 5.15c: rotational acceleration at position '3' for transverse excitation in the plane of the elbow: measured (-) and calculated with the discrete model for the elbow (--) and with the continuous model (..).

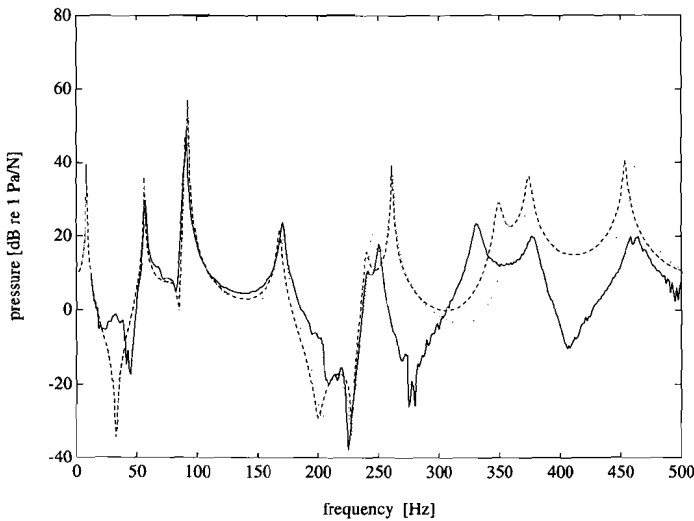


Figure 5.15d: normalized fluid pressure at position '3' for transverse excitation in the plane of the elbow: measured (-) and calculated with the discrete model for the elbow (--) and with the continuous model (..).

connections, by deformation of the rubber gaskets and by friction of the bolts. For lack of a better model, it has been assumed in the calculation that these connections can be described by a spring with 10% damping. A more accurate prediction of the pulsation and vibration levels can only be achieved on the basis of a more reliable description of the damping in the system.

The model calculations give direct access to the mode shapes of the test rig. Some structural mode shapes are shown in figure 5.16. The other predominant peaks in figure 5.15 correspond to fluid column resonances. Without coupling to the structure (but taking into account the lowering of the fluid wave speed due to the circumferential stiffness of the pipe wall) these resonances would occur at 87 Hz, 261 Hz and 435 Hz. The coupled model predicts these resonance frequencies at 93 Hz, 261 Hz and 454 Hz. Apparently, the model predicts that fluid resonances are not strongly influenced by coupling at the elbow. This is due to the fact that the resonances do not closely coincide with structural resonances. In reality the fluid resonances are measured at somewhat lower frequencies. This causes the second fluid mode to interact with the structural mode at 240 Hz. For these coinciding modes the mutual influence is much larger, as has been shown in section 3.6, which will introduce higher damping in the fluid mode, as seen in fig.5.15d.

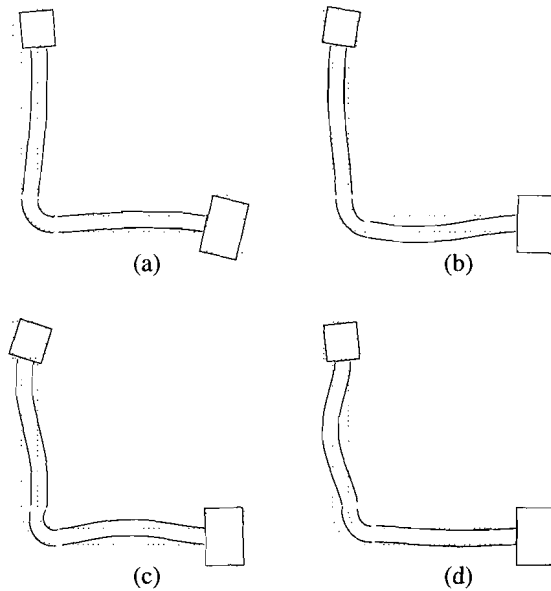


Figure 5.16: calculated structural mode shapes of the test rig at (a) 56 Hz, (b) 169 Hz, (c) 240 Hz, (d) 374 Hz.

5.4 Axial transmission through a rubber bellows

Flexible components, like bellows and hoses, are often introduced in pipe systems to compensate for misalignment and mechanical or thermal stresses. They are also used as resilient elements to reduce the transmission of vibrations and fluid pulsations into the system. To be able to select the appropriate compensator and to predict its effectiveness the designer needs a method to characterize these components.

The methods to characterize the vibro-acoustic transmission properties of fluid-filled bellows and hoses are much less established than, for instance, the methods to characterize flexible mounting elements for machines. Verheij [1982] describes how a test rig for measuring the transmission characteristics of flexible components can be modified to determine the 'blocked' transmission of structure-borne vibrations through fluid-filled hoses and bellows. The blocked transmission is sufficient to describe the element if its impedance is much smaller than the impedance of its seating. The applicability of this method is hampered by the fact that the impedance mismatch may be quite small in a practical situation and by the fact that the fluid-borne transmission cannot be handled. A transfer matrix description of the flexible components does not have these limitations. Veit [1976] describes measurements to determine the coefficients of the transfer matrix for axial fluid- and structure-borne waves through a bellows, neglecting fluid-structure interaction, but his measurement method has the disadvantage that the bellows cannot be pressurized. Oyadiji and Tomlinson [1985] have investigated the transfer matrix for structure-borne vibration transmission through reinforced rubber hoses. They take into account that the Young's modulus and the loss factor of the pipe wall material are essentially dependent on frequency and temperature. They have shown that a rubber pipe that is reinforced with fabric braids and a single helical spring wire may be treated as a pipe with a homogeneous isotropic wall material. However, they do not describe the important effect of the internal pressure on the dynamic stiffness (see e.g. [Kinns 1986]).

In an early stage of the research that is described in this thesis it was attempted to determine the axial fluid-borne and structure-borne transmission characteristics of a bellows from measurements in two straight pipes at its inlet and outlet, with application of circumferential and axial wave decomposition techniques. At that time the inverse methods (section 4.3) were not yet available. Unfortunately, the data that were obtained then are not sufficient to determine the bellows transfer matrix. Nevertheless, some interesting conclusions may be drawn from these data, which will be presented below.

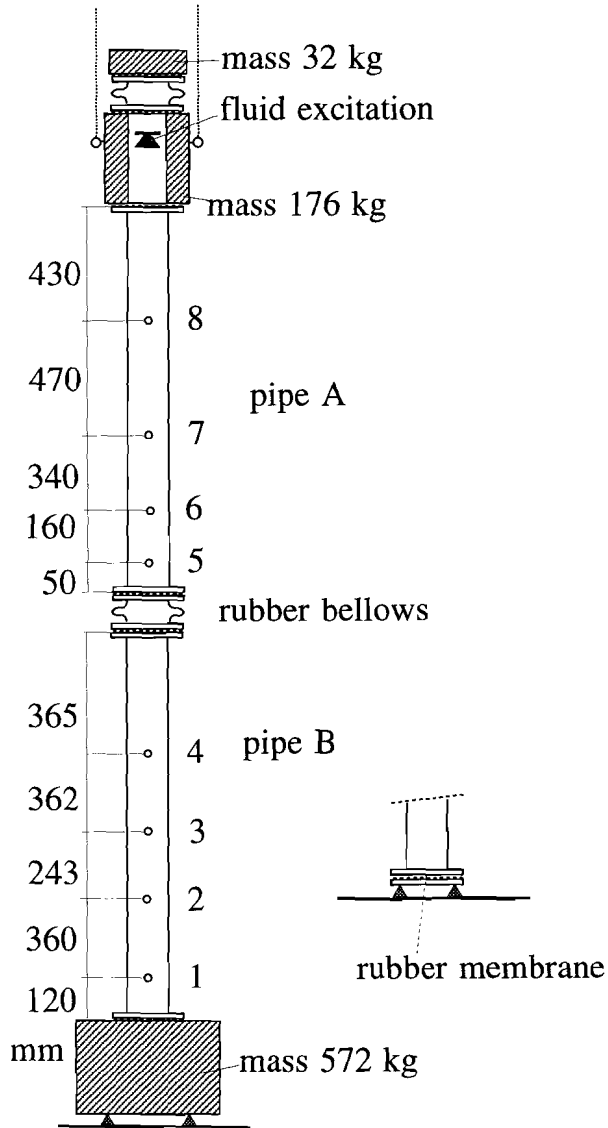


Figure 5.17: test arrangement with a rubber bellows, see also the annotations in the text.

5.4.1 test arrangement

The test arrangement with the bellows is shown in figure 5.17. The straight pipes and the bottom and top masses are the same as have been used in the 'straight pipe' and 'elbow' experiments. The bellows (*Elaflex EVR 150*) under investigation has been connected between the two pipes by means of bolts. A second bellows, equal to the first, is applied in combination with a 32 kg mass to close the system at the top without introducing a strong fluid-structure interaction. The fluid has been excited by an underwater loudspeaker (*Aquavox*) and the axial acceleration and the fluid pressure are measured at four positions in each pipe. A second experiment has been performed with the bottom mass replaced by a rubber membrane, to create a different fluid boundary condition. The bottom mass is mounted on soft rubber blocks and the top pipe is supported at the top mass by two ropes. The distance between the two flanges of the bellows is kept equal (120 mm) in both experiments.

5.4.2 measurement results

The wave amplitudes could be determined very well with the axial and circumferential decomposition methods. Figure 5.18 shows the resulting wave amplitudes for the fluid wave and the (quasi-longitudinal) extensional wave in the top and bottom pipes. The amplitudes of the upward and downward propagating waves are nearly equal. This implies that the bellows and the bottom mass form highly reflective terminations for both fluid-borne and structure-borne axial waves. As result, the vibration and pulsation levels in the bottom pipe are much smaller than the levels in the top pipe, where the source is located. The fluid waves in the top pipe show maxima close to the resonance frequencies of the fluid column between the bellows (for open-open boundary conditions these would occur at 350 Hz and 700 Hz). The amplitude of the upward propagating extensional waves in the top pipe is larger than the amplitude of the downward propagating waves. This shows that these waves are driven by coupling to the fluid waves at the bellows. They exhibit the fluid column resonances and a strong mechanical resonance at 550 Hz. The fluid waves in the bottom pipe show peaks at the fluid and mechanical resonance frequencies of the top pipe and at frequencies close to the resonance frequencies of the fluid column between bottom mass and bellows (for open-closed boundary conditions these would occur at 217 Hz and 652 Hz).

The experiment with the bottom mass replaced by a rubber membrane shows similar results, see figure 5.19. In this case the levels in the bottom pipe are even lower, because the membrane induces a weaker interaction of fluid pulsations and structural vibrations than the bottom mass. The amplitudes of the propagating waves in the top pipe (A) are hardly influenced by the change in boundary condition of the bottom pipe.

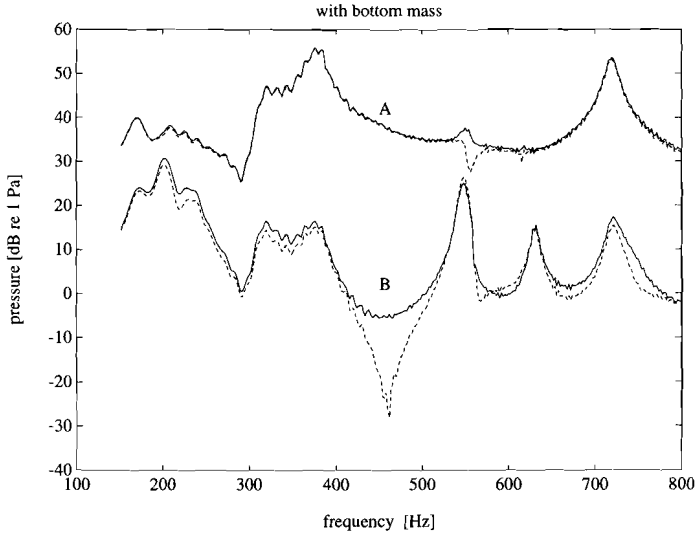


Figure 5.18a: wave amplitudes of the pressure waves in the top (A) and bottom (B) pipes for the geometry with the bottom mass, propagating away from the source (-) and reflected (--).

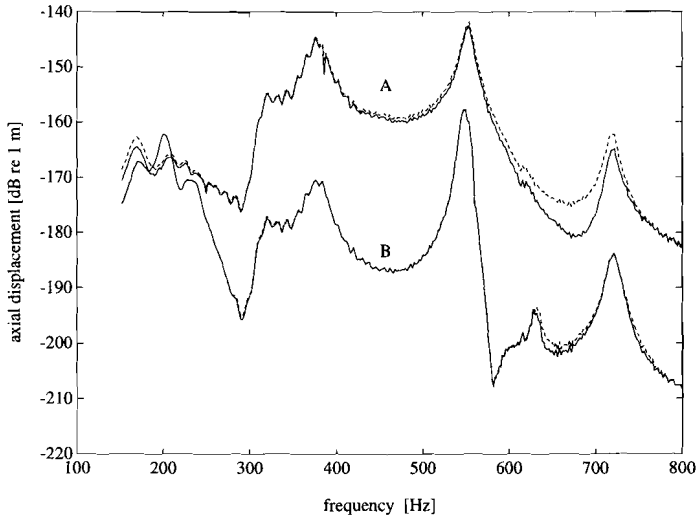


Figure 5.18b: wave amplitudes of the extensional waves in the top (A) and bottom (B) pipes for the geometry with the bottom mass, propagating away from the source (-) and reflected (--).

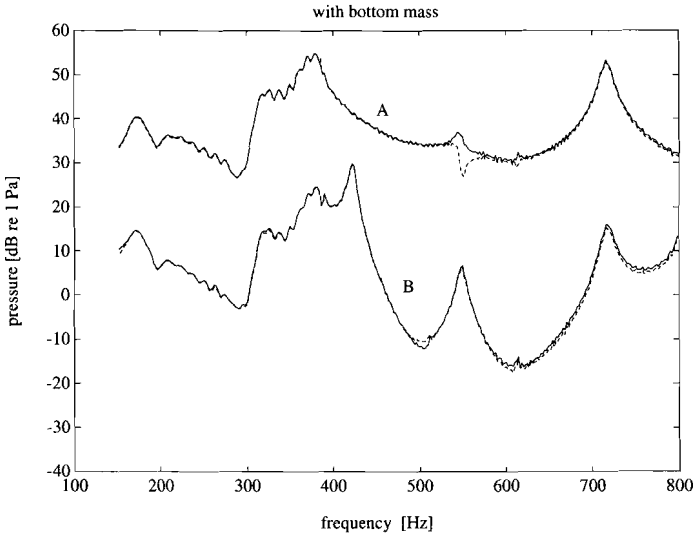


Figure 5.19a: wave amplitudes of the pressure waves in the top (A) and bottom (B) pipes, for the geometry with the rubber membrane at the bottom, propagating away from the source (-) and reflected (--).

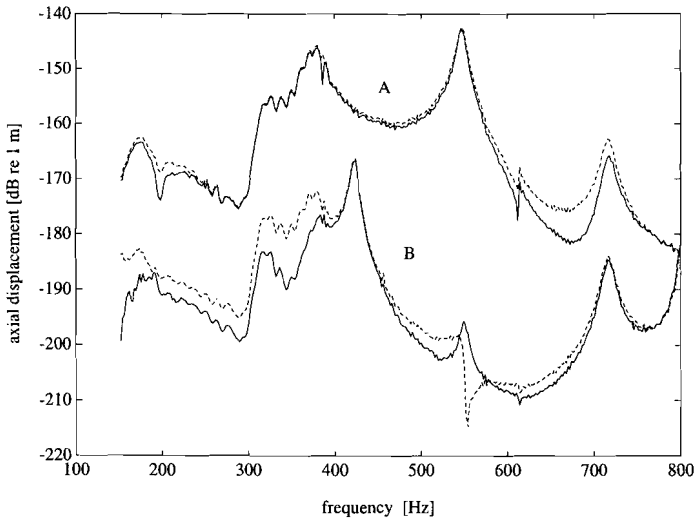


Figure 5.19b: wave amplitudes of the extensional waves in the top (A) and bottom (B) pipes for the geometry with the rubber membrane at the bottom, propagating away from the source (-) and reflected (--).

NOTE: Esparcieux [1986] found in his experiment that a rubber membrane at the end of a pipe (internal diameter 76 mm, filled with hydraulic oil) caused negligible reflections. However, our experiment (fig.5.19a) does not confirm this conclusion. It shows the high reflectivity that might be expected for such a pressure release boundary.

The measurements have been performed with fluid excitation at the top only. Although the measurements have been repeated for two different acoustic loads at the bottom, these two measurements are not sufficient to determine the 4x4 transfer matrix for the coupled fluid-borne and structure-borne waves through the bellows.

Purshouse [1986] has proposed describing the fluid pulsation transmission through a bellows by means of a frequency dependent distensibility parameter. This parameter accounts for the dynamic stiffness, the hysteretic losses and inertial effects. Although Purshouse recognizes the importance of the inertia of the fluid, he incorrectly neglects the pressure difference across the bellows that is caused by this inertia. Nevertheless, it is useful to investigate whether it is possible to represent a bellows by a lumped mass-spring model. A simple model for the fluid pulsation transmission describes the distensibility of the bellows as a stiffness K , located at its centre, and the fluid inertia by two masses M one on either side of this stiffness. This model leads to a transfer matrix:

$$\begin{pmatrix} p_B \\ v_B \end{pmatrix} = \begin{pmatrix} 1 - \frac{M\omega^2}{K} & \frac{M\omega^2}{A_f} \left(2 - \frac{M\omega^2}{K} \right) \\ -\frac{A_f}{K} & 1 - \frac{M\omega^2}{K} \end{pmatrix} \begin{pmatrix} p_A \\ v_A \end{pmatrix}, \quad (5.4)$$

where the subscripts A and B refer to the top and bottom sides of the bellows respectively. The input mobility ($\dot{v}_A/A_f p_A$) of the bellows is much larger than the input mobility of the bottom pipe, so that it is approximately equal to

$$\frac{\dot{v}_A}{A_f p_A} \approx \frac{i\omega}{K - M\omega^2}. \quad (5.5)$$

Figure 5.20 shows the magnitude of the input mobilities at the top side of the bellows, both for the experiment with the bottom mass and for the experiment with the membrane. The fluid mobilities at the top side of the bellows are nearly equal for these geometries, while they are found to be totally different at the bottom side. The shape of the spectrum agrees with the simple model of eq.(5.5), as shown by the dotted curves. The fluid mass that is involved is $M \approx 1.2$ kg, about half the mass of the fluid in the bellows. The stiffness is $K \approx 1.5 \cdot 10^6$ kg/s² with the bottom mass and $K \approx 1.2 \cdot 10^6$ kg/s² with the rubber membrane. As expected, the distensibility is somewhat lower if the axial mobility of the bottom pipe if

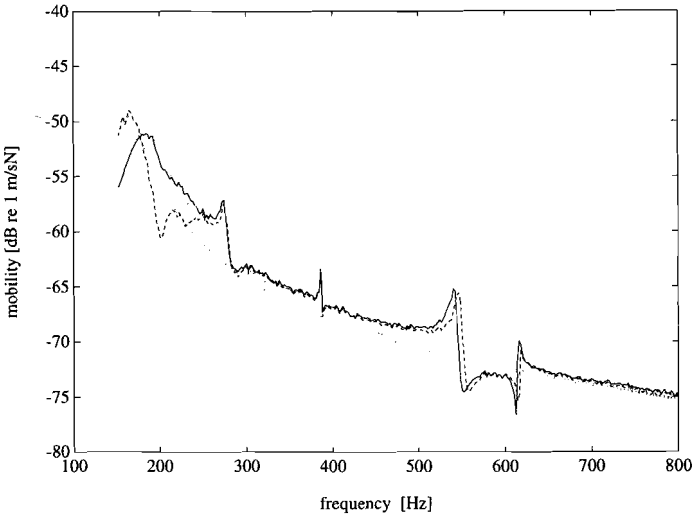


Figure 5.20: input mobility (\dot{v}/A_p) for the fluid at the top side of the bellows, for the experiments with the bottom mass (-) and with the rubber membrane at the bottom (--). The dotted lines show the model of eq.(5.5) for the two cases.

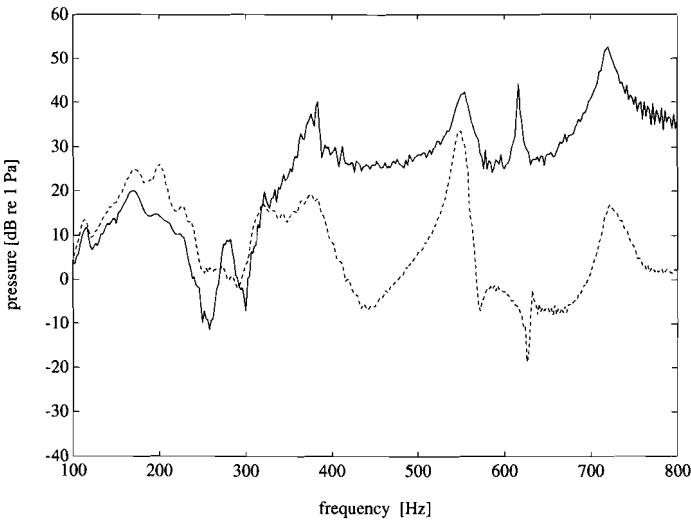


Figure 5.21: pressure at the bottom of the bellows, determined from measurements in pipe B (--) and from measurements in pipe A, using a lumped mass-stiffness model for the bellows (-).

increased. The bellows exhibits about 25% damping of the fluid pulsations, due to coupling with mechanical vibrations in the system and hysteretic losses in the bellows.

The lumped mass-stiffness model gives a good description of the reflection characteristics of the bellows. Now it is interesting to investigate whether the same model can be used to describe the transmission characteristics. The measured spectra of pressure p_A and fluid displacement v_A , for the experiment with the bottom mass, are inserted into equation 5.4. The resulting pressures p_B are compared with the measured pressure in figure 5.21. The comparison shows large differences. This implies that the fluid-structure interaction may not be neglected.

A more accurate prediction can only be given if the cross-mobilities, that relate pressure pulsations and axial pipe vibrations, are taken into account. These may be determined in a similar test arrangement, using an inverse method (section 4.3). This method involves measurements with pulsation excitation and experiments with vibration excitation. Geometrical variations at the bottom of the system, to create different acoustic loads, result in a badly conditioned inversion, because these changes hardly influence the excitation side of the bellows. Of course this is only true for the very soft, non-pressurized bellows that has been investigated here. In practice, bellows will often be stiffer, through their design or due to a high internal static pressure. It is therefore interesting to investigate whether the transfer matrix of a stiffer bellows can be determined by an inverse method.

5.5 Conclusion

A series of laboratory experiments has been performed to partially validate the models for wave propagation in fluid-filled pipes and to test the practicability of the experimental methods that have been developed in this study.

It has been shown that it is possible to decompose the different waves in a straight pipe by applying the appropriate combination of transducers. This lead also to the conclusion that the 'beam model' that lies at the basis of the compute program *PRESTO* gives a correct description of wave propagation in a straight fluid-filled pipe up to twice the cut-on frequency for $n=2$ lobar waves.

It has been shown that pressure measurements with a single pressure transducer mounted in the pipe wall are sensitive to transverse vibrations of the pipe, due to the inertia of the fluid in the pipe. This effect can be suppressed by applying two pressure transducers per cross-section, at opposite positions in the pipe wall.

A soft rubber bellows is shown to be a very good isolator for both structure-borne and fluid-borne waves. Its reflective properties may be characterized by a simple mass and stiffness. Its transmission characteristics are strongly influenced by fluid-structure interaction.

The results of *PRESTO* calculations have been compared with experimental data. Generally, the agreement is satisfactory. Like all deterministic calculation methods, the transfer matrix method will only give an accurate prediction of resonance frequencies and vibration and pulsation levels in a pipe system when the input parameters are estimated correctly. Especially boundary conditions and loss factors may be difficult to estimate. An accurate prediction of, for example, maximum stress levels in a pipe system, requires the input of actual measurement data or data that are based on experience with similar systems. Nevertheless, the calculation method is a valuable tool to investigate the vibro-acoustic behaviour of systems. It gives access to mode shapes and can be used to study the effect of modifications to the system.

6. ACOUSTIC CHARACTERIZATION OF A CENTRIFUGAL PUMP

6.1 Introduction

Centrifugal fluid pumps are widely used as machines for the transportation of fluids, heat or hydraulic power. Pumps may be responsible for both mechanical and hydraulic excitation of the piping, leading to excessive noise levels or to problems with reliability and control in the pumping circuit. The impact of such problems may be enormous. For example the lead unit of the Darlington Nuclear Generating Station has been shut down for a period of 18 months after serious damage to a fuel pipe bundle that appeared to be caused by pump-induced pulsations [Telfer 1993].

In a centrifugal pump the generation of fluid pulsations will be the main source of noise and vibrations [Mühle 1975]. We will limit ourselves to the characterization of a rigidly mounted pump with respect to the generation and the transmission of fluid pulsations. Different mechanisms may be responsible for the generation of pressure pulsations in a centrifugal pump (see e.g. [Guelich & Bolleter 1992; Makay *et al.* 1993]). One may distinguish volume fluctuations (monopole type sources) and fluctuating forces (dipole type sources). In a centrifugal pump the volume fluctuations will be mainly related to cavitation. Both the formation of vapour filled cavities when the local pressure drops below the vapour pressure of the fluid and the collapse of the bubbles when they are convected into regions of higher pressure are responsible for pulsations. The fluctuating forces will for example be caused by rotational unbalance of the pump shaft, by the interaction of the flow circulations around the rotating impeller blades and the fixed volute or diffuser blades and by the interaction of turbulent flow with the blades.

Apart from the examples given, other mechanisms of pulsation generation in centrifugal pumps have been recognised, such as rotating stall [Mongeau 1992] or rotor dynamic instability [Makay 1993]. There is very little information available about the pulsation source strength in relation with the different source mechanisms. Simpson *et al.* [1966-67] have investigated hydraulic noise generation both theoretically and experimentally. Their theoretical work considers unsteady forces at the blade passing frequency, caused by unsteady blade circulation and viscous wake effects. From experiments on 7 different centrifugal pumps they deduced a semi-empirical formula that correlates the sound pressure in the discharge pipe with the specific speed (a number that characterizes similar pumps [Stepanoff 1957]) and the power consumption of the pump. Mühle [1975] rewrote this

formula in international units. Although the experiments show only a ± 2 dB spread compared to the correlation formula, several objections can be made. Bartenwerfer [1980] argues that the variables in Simpson's formula are not independent so that 'dubious functional relationships' follow. Bartenwerfer suggests an acoustic similarity law for hydraulic noise production in pumps, in analogy to fans, but no experimental verification of this law has been given. The level of pressure pulsations measured in a pumping system is dependent on both the source strength of the pulsation generation in the pump and the response of the piping. It is not clear to what extent system response has influenced the measurements on which Simpson's correlation formula is based.

The aim of the research that is described in this chapter was to develop an experimental method that allows source and system response effects to be separated. The inverse method will lead to a characteristic transfer matrix and a source strength vector, see eq.(3.37), so that the centrifugal pump can be introduced into the calculation model for predicting pulsations and vibrations in fluid-filled pipe systems that was described in chapter 3. Note that the characteristic parameters will depend on the operating conditions of the pump and on specific geometrical details of the pump. The source characterization method can help to identify pulsation generating mechanisms and to study the effect of geometrical modifications. Hence the method is relevant for both pump designers and designers of pumping systems.

The experimental characterization of acoustic sources in pipe and duct systems has been studied since the early seventies, mainly with application to fan noise and engine exhaust noise. Overviews of these studies are given by Bodén [1989] and Prasad [1991]. Assuming that the source behaves as a linear, time-invariant system, it is modelled as a 'black box' with one or more inlet and outlet ports. The approach is limited to frequencies below the cut-on frequency of non-planar waves in the suction and discharge pipes. Then the acoustic state at the ports is described completely by two independent variables, like for example the travelling wave amplitudes p_+ and p_- [Bodén 1989]. To stay in agreement with the transfer matrix formalism of chapter 3 here the local pressure pulsation p and volume velocity fluctuation q are used.

The determination of the one-port source characteristics of fluid pumps is available as a British Standard Method [BS 6335: Part 1 1990]. This method is valid for positive displacement pumps, that have no significant acoustic coupling between inlet and outlet. For application to centrifugal pumps it requires that the piping attached to the inlet remains unchanged, so that it can be treated as a part of the source [Davidson 1977; Whitson & Benson 1993]. The centrifugal pump itself should be described as a two-port. Recently methods have been developed to determine the two-port source and transmission character-

istics of in-duct fans [Terao & Sekine 1992; Åbom *et al.* 1992; Lavrentjev *et al.* 1993]. Centrifugal pumps have received less attention. Experiments on the two-port transmission characteristics of a centrifugal pump have been reported by Ng & Brennen [1978] and by Stirnemann *et al.* [1987]. In these studies the generation of pulsations in the pump has been left out of consideration. The experimental characterization of centrifugal pumps has also been reported by Trollé *et al.* [1989], by Lauro & Trollat [1993] and by Jacob & Prenat [1993], but objections can be made against their source model, as will be explained in the next section.

This chapter gives a description of the two-port model for the centrifugal pump. An experimental source characterization method is presented. To investigate the applicability of this method, experiments have been performed on a single stage centrifugal pump in a laboratory test loop. The transmission and generation of fluid pulsations in this pump have been studied in relation to the operating condition.

6.2 A two-port model for the centrifugal pump

We are interested in the frequency range where only *plane waves* can propagate in the suction and discharge pipes of the centrifugal pump. It is assumed that the centrifugal pump behaves as a *linear, time-invariant* system [Bodén & Åbom 1990]. The results of the measurements will indicate to what extent these assumptions hold. The pump is modelled as an acoustic two-port. The active two-port is characterized, in the frequency domain, by a passive transfer matrix $[T]$ and two active source variables: a pressure source strength Δp and a volume velocity source strength Δq .

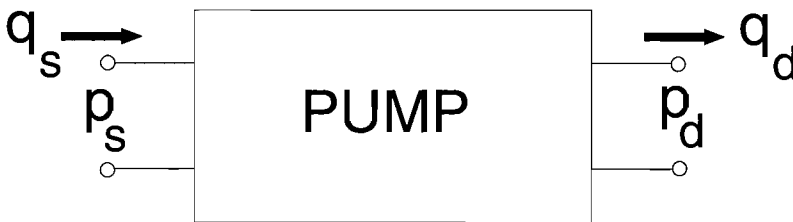


Figure 6.1: Schematic representation of the centrifugal pump as a two-port.

At a given angular frequency ω , the state vectors at the suction (subscript 's') and discharge (subscript 'd') ports, see figure 6.1, are related by:

$$\begin{pmatrix} p_d(\omega) \\ q_d(\omega) \end{pmatrix} = \begin{bmatrix} T_{11}(\omega) & T_{12}(\omega) \\ T_{21}(\omega) & T_{22}(\omega) \end{bmatrix} \begin{pmatrix} p_s(\omega) \\ q_s(\omega) \end{pmatrix} + \begin{pmatrix} \Delta p(\omega) \\ \Delta q(\omega) \end{pmatrix}. \quad (6.1)$$

The frequency spectra of the six complex parameters ($[T], \Delta p, \Delta q$) in this model give a complete description of the two-port.

The four elements of the transfer matrix $[T]$ describe the transmission of pressure waves between the inlet and outlet ports of the pump. The ports may be chosen at the suction and discharge flanges of the pump, but for reasons of interpretation it is advantageous to consider the suction and discharge channels in the pump as a part of the piping. All sources should, however, be located between the ports. The propagation of plane waves in these channels is described using the transfer matrix for a fluid column of length dz :

$$\begin{bmatrix} \cos(k_f dz) & -(i/Y_o) \sin(k_f dz) \\ -i Y_o \sin(k_f dz) & \cos(k_f dz) \end{bmatrix}, \quad (6.2)$$

where k_f is the wavenumber for plane waves and Y_o is the specific admittance ($Y_o = A_f / \rho_f c_f$). It is assumed that the viscous losses in these channels are negligibly small compared to the losses in the source region.

Stirnemann *et al.* [1987] (see also Bolleter *et al.* [1990,1993]) have shown that the coefficients of the passive transfer matrix can be fitted to a lumped parameter model in the low-frequency range. In this model the transfer matrix is described by analogy with a so-called π -equivalent electrical network, consisting of two parallel elements with admittances Y_1 and Y_3 and a series element with impedance Z_2 , see figure 6.2. The transfer matrix is then expressed as:

$$T = \begin{bmatrix} 1 + Y_1 Z_2 & -Z_2 \\ -Y_1 - Y_3 - Y_1 Z_2 Y_3 & 1 + Y_3 Z_2 \end{bmatrix} \quad (6.3)$$

The admittances Y_1 and Y_3 are dominated by the total compliance C inside the pump ($Y = +i\omega C$). This compliance is determined by the compressibility of the fluid and the flexibility of the pump casing. The compliance will increase dramatically when air or cavitation bubbles are present inside the pump. The series impedance Z_2 mainly represents the inertia L of the fluid in the pump in combination with a damping R : $Z_2 = R_2 + i\omega L_2$. Bolleter *et al.* [1990] attribute this damping to the quasi-steady resistance that is related to the gradient of the head-flow curve of the pump at the operating point, but the real part of Z_2 represents the effect of any kind of damping. More sophisticated models may be

developed to describe larger pumps at higher frequencies [Jacob & Prenat 1993; Tavernier *et al.* 1993], whereas a multi-stage pump can probably be modelled by a network consisting of a series of single stage models [Kläui 1993]. However, for the small single stage pump on which we performed our experiments the simple model of figure 6.2 does suffice.

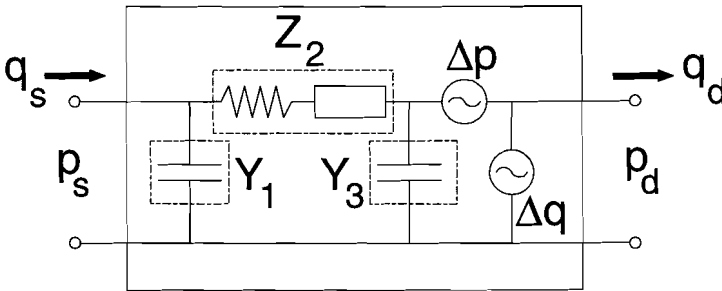


Figure 6.2: Lumped parameter model for the pump

The total effect of all pulsation generating, or absorbing, mechanisms in the pump is described by an equivalent source vector, consisting of a monopole Δq and a dipole Δp . The equivalent source vector will generate the same pressure field in the pipe system as the actual sources. Here we have chosen to locate the source vector at the outlet, see figure 6.2. It could equally be replaced by any combination of two independent source variables at either inlet or outlet (e.g. by a monopole at the inlet and a monopole at the outlet).

NOTE: A definition of two source vectors, one at the inlet and one at the outlet, as in the models by Trollé [1989] and Jacob [1993] introduces two dependent source variables. Although multiple sources may be present in the pump, the two-port model can only distinguish two independent equivalent sources. The approach of Trollé and Jacob is therefore not an improvement of the model presented here.

Without extra information it is not strictly possible to identify individual sources in the pump from the two-port model. However, different source mechanisms may sometimes be recognized from their frequency characteristics, see for instance Makay *et al.* [1993]. The ratio of the source vector elements Δp and Δq will give further information about the nature and or the location of the source mechanism in the pump.

6.3 Characterization method and procedure

This section describes the experimental method used to determine the frequency spectra of the transfer matrix [T] and the source vector ($\Delta p, \Delta q$) that characterize the centrifugal pump as a two-port (eq.6.1). The method is based on pressure measurements in the suction and discharge pipes. The volume velocities q are derived from these pressures using the 'two microphone' method, that has been described in section 4.3.1.

First the passive transfer matrix is determined from experiments with external fluid excitation. Assuming that *linearity* holds, the external source creates pressure pulsations that are not correlated with the pump source vector ($\Delta p, \Delta q$). Using coherence analysis with the excitation signal as a reference allows us to determine the passive transfer matrix while the pump is running, provided that the external source is sufficiently strong to dominate the pulsations that are generated in the pump. An extra advantage of this coherence analysis is that disturbing noise due to turbulent flow across the pressure transducers is suppressed. A 'two source-location' method, that has been introduced by Munjal and Doige [1990], is used to create the two different acoustical test states 'A' and 'B' that are needed for the determination of the transfer matrix. This method is valid under the condition of *reciprocity*. Strictly speaking, reciprocity is not valid for a pipe with flow [Munjal & Doige 1990], but at low Mach-numbers this condition is approximately fulfilled. The two test states are achieved by first applying fluid excitation at the suction side of the pump and next at the discharge side. The 'two source-location' method is preferable to the 'two-load' method, in which the source location is kept constant and the test state is varied by variation of the acoustic load the pump, because it produces independent states in any pipe system [Åbom 1992]. At both test states we determine the pressure and volume velocity spectra at the suction and discharge ports of the pump, using a 'two-microphone' method. The unknown two-port matrix [T] is then determined from the matrix equation:

$$\begin{bmatrix} p_d^A & p_d^B \\ q_d^A & q_d^B \end{bmatrix} = \begin{bmatrix} T_{11} & T_{12} \\ T_{21} & T_{22} \end{bmatrix} \begin{bmatrix} p_s^A & p_s^B \\ q_s^A & q_s^B \end{bmatrix} \quad (6.4)$$

At each frequency this equation is solved for [T] by Gaussian elimination. The accuracy with which [T] is determined depends on the condition number of the matrix of pressures and volume velocities that are measured at the suction side of the pump. The determinant of [T] indicates whether the assumption of reciprocity hold, because its magnitude should in this case be equal to one [Munjal & Doige 1990].

Once the passive transfer matrix [T] has been determined, the source vector follows from

pressure measurements in a single configuration with the pump running and without external fluid excitation. In this situation the pressure pulsations in the pipe system are generated by the pump. The source vector is then determined using equation (6.1).

Instead of directly using the experimentally determined transfer matrix for the determination of the source vector, the lumped parameter model of eq.(6.3) is used. The lumped parameters are obtained by fitting to the measured transfer matrix coefficients. This has the advantage that random errors in the transfer matrix are averaged, so that they do not contribute to the error in the source vector.

6.4 Description of the test facility and instrumentation

The validity of the two-port model and the inverse method for determining the model parameters has been tested in a laboratory test loop with a centrifugal pump.

6.4.1 the centrifugal pump

The experiments have been performed on a single stage, in-line, centrifugal pump (Grundfos LP100-125/134). Its nominal power is 7.5 kW and it has a nominal speed of $n=2870$ rpm (48 Hz), a nominal head of $H=18$ m H₂O (1.8 bar) and a nominal flow rate of 96 m³/h ($Q=0.027$ m³/s), hence its specific speed equals $n_s=nQ^{1/2}H^{-3/4}=54$ min⁻¹m^{3/4}s^{1/2}. The impeller has six blades and it has a diameter of 134 mm and a width at the outlet of 22 mm. The suction and discharge openings of the pump have a diameter of 10 cm. The operating condition of the pump can be changed by variation of the pump speed (continuously from zero to 2870 rpm) and by variation of the flow using valves in the test loop, downstream of the pump. The Reynolds number, based upon the impeller tip velocity V_{tip} , the impeller diameter D and the kinematic viscosity ν , is high:

$$Re_{tip} = \frac{V_{tip}D}{\nu} > 10^6 \quad (6.5)$$

The fluid dynamic performance of the pump is then governed by two non-dimensional parameters [Stepanoff 1957], the capacity coefficient Φ and the head coefficient Ψ :

$$\Phi = \frac{Q}{\pi D b V_{tip}}, \quad \Psi = \frac{\Delta P}{\frac{1}{2} \rho V_{tip}^2} \quad (6.6)$$

Here Q is the time averaged volume velocity in the pump and ΔP the time averaged pressure difference across the pump. b is the width of the impeller at the tip. Figure 6.3 shows the non-dimensional head-flow curve of the pump (ψ against Φ) as measured in the

test loop at two different pump speeds. This shows that the performance of the pump, including hydraulic losses, can indeed be described by a single non-dimensional curve.

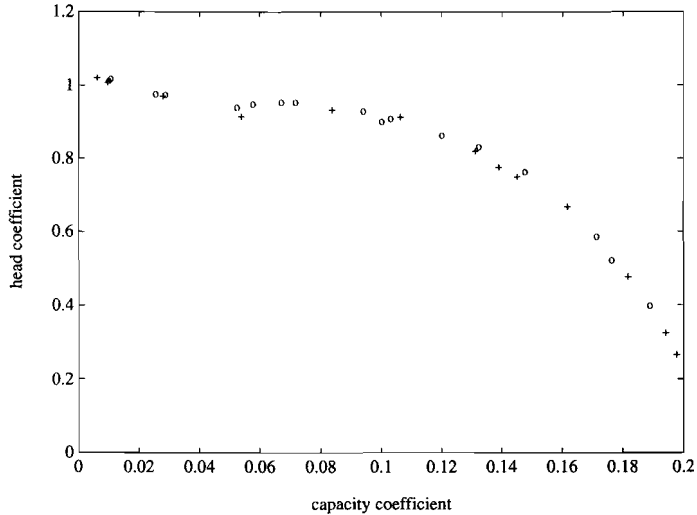


Figure 6.3: Non-dimensional head-flow curve of the pump, measured in the test loop at two different pump speeds (+: 1460 rpm, o: 2365 rpm)

6.4.2 the test loop

The laboratory test loop is shown schematically in figure 6.4. Water is circulated from the reverberant water tank of TNO-TPD (length \times width \times depth=12 \times 6 \times 5 m³). This tank guarantees a constant head of 5 m and the use of 'stable' water, which has been in the tank for several years ($T=20^{\circ}\text{C}$, $\rho_f=1000\text{ kg/m}^3$, $K_f=2.19\cdot 10^9\text{ Pa}$). Two membrane valves and one butterfly valve are installed in the discharge line, together with a constant flow resistance in the form of a nine hole restriction plate with a 50% opening. The piping has an internal diameter of 15 cm. The flow speed is measured, with an accuracy of $\pm 0.002\text{ m/s}$, using an electro-magnetic flow meter (*Altometer K380/0*). The static pressure is measured, relative to atmospheric pressure, at the suction and discharge flanges of the pump, using capacitive ceramic transducers (*Cerabar PMC 130 & 133*) with an accuracy of $\pm 0.01\text{ bar}$. The pump speed is determined at the pump shaft with an optical revolution counter (*Hioki 3402*, $\pm 0.01\text{ s}^{-1}$).

The pump is installed between two straight steel pipes, each of 3 m length with an internal diameter of 15 cm and a wall thickness of 4.5 mm ($\rho_s=7800\text{ kg/m}^3$, $E_s=2.1\cdot 10^{11}\text{ Pa}$, $\nu_s=0.31$). Short PVC contractions (length 43 mm) adapt the inlet and the outlet diameter of

the pump ($\phi=10$ cm) to the pipes. Both the pump and the T-joints at the end of these pipes have been bolted to heavy concrete masses, to minimize pipe vibrations.

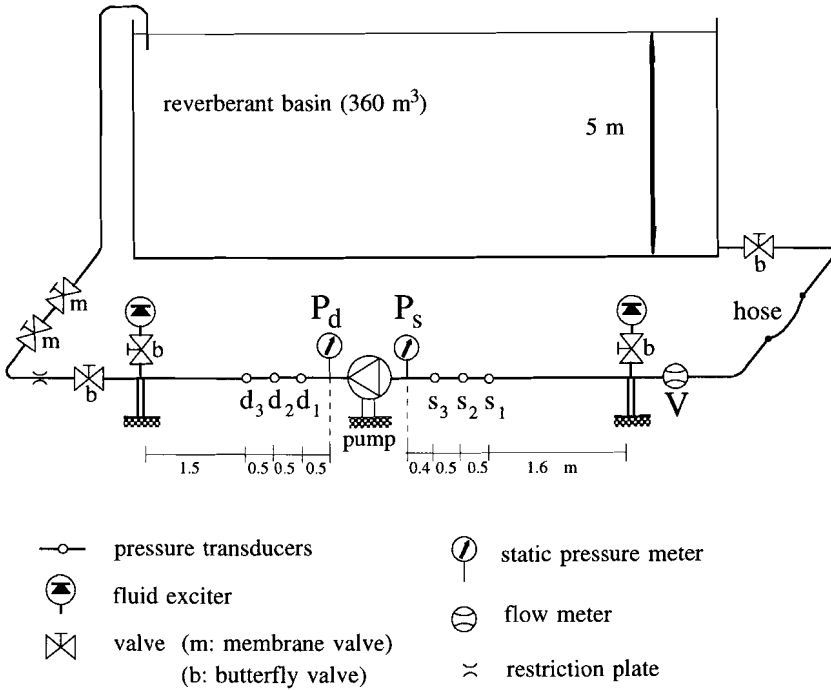


Figure 6.4: Schematic representation of the laboratory test loop

6.4.3 external excitation

For application of the two-source method for determination of the pulsation transfer matrix of the pump two external fluid exciters have been installed, see figure 6.4. They are connected to the pipe system via T-joints. They can be disconnected from the system by means of butterfly valves. Both exciters are driven by either single frequency sine waves or periodically swept sine signals that are generated by a digital waveform generator (*Wavetek 95*)

Two different types of excitation source are used. The source at the suction side of the pump is based on an existing electro-dynamic underwater loudspeaker (*Actran J11*), see figure 6.5. It has been bolted to a pipe flange. The hydrostatic pressure at the piston is compensated via a small diameter flexible hose that pressurises the air bag behind the piston. The acceleration of the piston is measured by a sealed accelerometer (*Endevco 226*). This excitation source has been used earlier to demonstrate the experimental source

characterization [de Jong 1993]. It appeared that the piston acceleration cannot be used to characterize the source strength, due to acoustic 'leakage' to the air bag, via the membrane, along the sides of the piston.

Figure 6.6 shows the fluid exciter that has been installed in the discharge pipe of the pump. It consists of a PVC piston that is mounted in a rubber bellows and excited by an electro-dynamic shaker (*Derritron VP-4*). The excitation force is measured by a force transducer (*B&K 8200*).

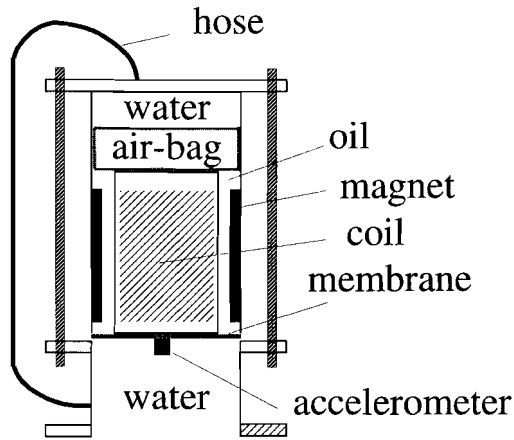


Figure 6.5: Underwater loudspeaker, adapted for use as a fluid exciter in the test loop.

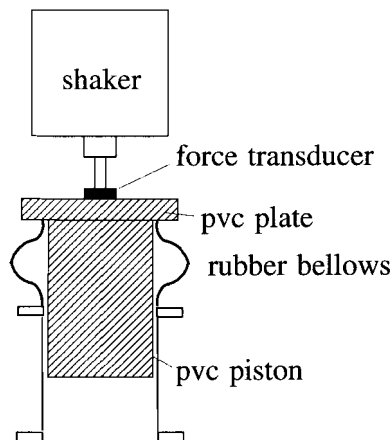


Figure 6.6: Fluid exciter, consisting of a rubber bellows, a PVC end plate, a PVC piston and a shaker.

6.4.4 pressure transducers, calibration and data processing

The pressure pulsations in the pipe are measured using piezo-electrical transducers (*PCB 116A02*), that are mounted flush in the pipe wall. Special adapter blocks have been used to guarantee that the transducers are mounted at the prescribed torque. The pressure transducers have been calibrated individually, while mounted in the adapter blocks, using a hydrophone calibrator (*B&K 4223*). This calibrator is provided with a chamber in which the pressure transducer is exposed to the same air pressure (63 Pa at 250 Hz) as a reference microphone (*B&K 4134*). The voltage signals of the transducers are fed into TPD-made source followers and amplifiers. In this configuration the sensitivity of the transducers is partly determined by the capacity of the cable between transducer and source follower. It has been ensured that cables of equal capacity ($\pm 1\%$) were used for all transducers. This calibration procedure allowed the sensitivity of the transducers to be determined to an accuracy of $\pm 2\%$. As the piezo-electrical transducers are operated far below their resonance frequency of 130 kHz, the accuracy of the phase relationship between the transducer signals is mainly determined by the amplifiers and the anti-aliasing filters of the analyzer. This phase relationship was calibrated by feeding equal electrical noise signals into the source followers. The phase between the channels is matched within 0.2° in the frequency range up to 1000 Hz. This is considered to be sufficiently accurate, so that no phase correction has been applied to the data. The transducers are compensated for acceleration in their axial direction with a resulting vibration sensitivity of about $1.4 \text{ Pa}/(\text{m/s}^2)$. Transverse vibration of the pipe may disturb the pressure pulsation measurement due to the inertia of the water in the pipe. Therefore the average is taken of the signals of two pressure transducers that are mounted at opposite sides in the pipe wall at each measurement position.

Data processing is performed using a four-channel FFT analyzer (*Scientific Atlanta SD380C*). The auto- and cross-power spectra are transferred from this analyzer to a PC, where they are processed using *MATLAB* software.

6.4.5 linearity, stability and accuracy

The reliability of the measurement method for source characterization depends on the linearity and the stability of the pulsations in the pipe system. These conditions may easily be violated when air bubbles are present in the fluid-filled pipe system. After filling the system it takes a few days, in which the pump is operated, before stable pressure measurements can be performed. The stability and the accuracy of the measurements have been checked regularly.

The linearity, or rather the homogeneity, of the transmission of pulsations in the system has been tested with the pump at standstill. The fluid was excited in the suction line, using

a periodically swept sine (40-400 Hz) at three different levels (ratios 1:1.5:2.5). The frequency averaged amplitude error between the spectra is $\pm 2\%$, the phase accuracy is $\pm 3^\circ$. The random error related to non-perfect coherence in the frequency response function H_{xy} for a two-channel pressure measurement may be estimated from the coherence function γ_{xy}^2 [Bendat & Piersol 1980]:

$$\varepsilon [|H_{xy}(f)|] \approx \sqrt{\frac{1 - \gamma_{xy}^2}{2\gamma_{xy}^2 N_{avg}}} \quad (6.7)$$

where N_{avg} is the number of averages. For the three frequency response functions the frequency averaged random error is $\pm 0.6\%$. Hence the variance in the linearity check cannot be attributed to random errors only. However, the variance is sufficiently small to accept the linear approach.

The stability of the pulsation transmission in the pipe system has been checked. As an example the frequency response function between the pressures at the positions d1 and d2 in the discharge pipe, due to excitation in the suction line, as measured on two occasions (66 days apart) is shown in figure 6.7. During these measurements the pump was running at 24 Hz close to its best efficiency (design) point. The frequency response functions have been measured with the external source signal as a reference. It appears that the measurement is stable within about 5% in magnitude and 5° in phase. During the source strength measurements the stability of the pump-generated pulsations has been checked regularly. The shaft rotation frequency showed a maximum variation of 0.2% during a single experiment, while the pressure fluctuations at equal load were stable to within 10%. The linearity of the pulsation generation in the pump will be discussed in section 6.6.

As said before, two pressure transducers have been used at opposite positions at each pipe cross-section to suppress measurement errors due to transverse vibration of the pipe. The average value of the signals of these transducers gives the $n=0$ fluid pressure, whereas the difference of the signals gives the fluid pressure due to transverse vibrations of the pipe. A comparison of the sum and the difference of the signals of two transducers at the same cross-section showed that the apparent pressure pulsations due to transverse vibration are at least 30 dB lower than the actual plane wave pressure pulsations. The effect of transverse vibrations on the sum of the pressure transducer signals will therefore be negligible. Note that the low level of vibration is achieved through a purposefully rigid design of the test loop. In a common, less rigid, pipe system the suppression of transverse vibrations will be essential for reliable pressure measurements.

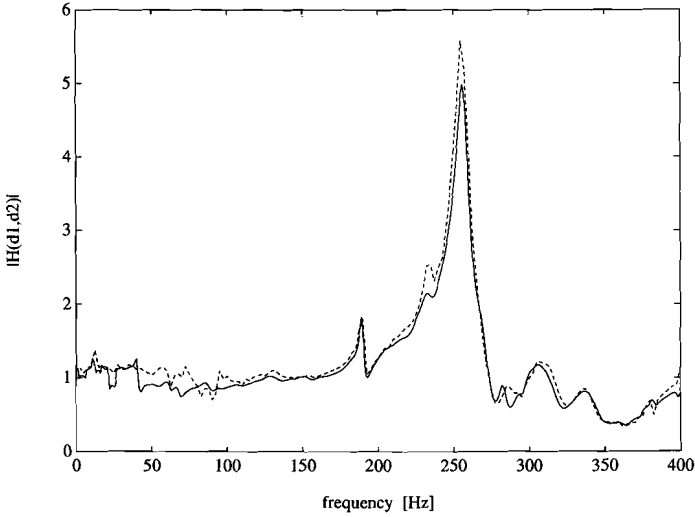


Figure 6.7a: Amplitude spectrum of the frequency response function between the pressures at positions d1 and d2, with excitation in the suction line and the pump running at 24 rps. The dashed line has been measured 66 days later than the solid line.

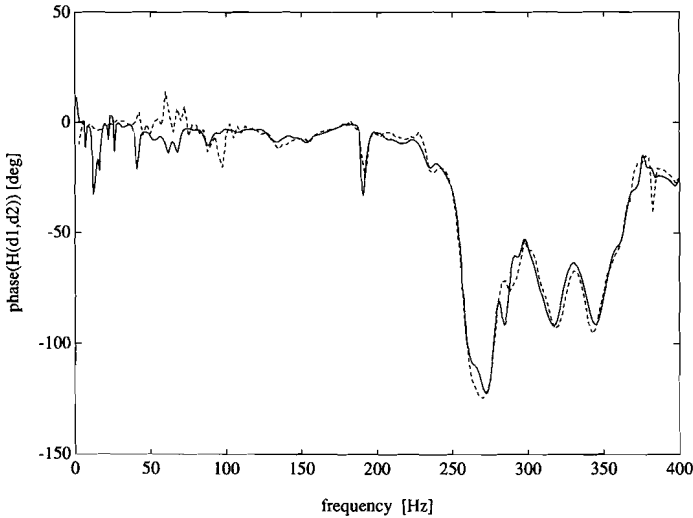


Figure 6.7b: Phase spectrum of the frequency response function between the pressures at positions d1 and d2, with excitation in the suction line and the pump running at 24 rps. The dashed line has been measured 66 days later than the solid line.

6.5 Experimental determination of the passive transfer matrix

The passive transfer matrix of the pump has been determined experimentally using the 'two source-location' method. The two-microphone method [Chung & Blaser 1980] (see also section 4.3.1) is applied to determine the acoustic pressure and volume velocities at the suction and discharge ports of the pump. Plane wave propagation through the contractions at the inlet and outlet flanges of the pump and in the suction and discharge channels in the pump (respectively 30 and 20 cm long) are taken into account by transfer matrix multiplication (eq.6.2). The pressure pulsations are measured at three equidistant positions ($\Delta z=0.5$ m) in both the suction and the discharge pipe, see fig.6.4. The wavespeed c is calculated from geometrical and material properties using eq.(2.28), which results in $c=1260$ m/s. This prediction has been verified using the three transducer method that is given in the appendix C 4.2 of the British Standard [BS 6335 Part I 1990]. Repeated measurements in both suction and discharge pipes result in $c=1265$ m/s ($\pm 3\%$). The calculated wavespeed is considered to be sufficiently accurate for the data processing. According to Bodén & Åbom [1986] the two-microphone method is only convergent with regard to errors in the input data when $0.1\pi < k\Delta z < 0.8\pi$. Hence the shortest separation ($\Delta z=0.5$ m) is applicable in the frequency range between 126 and 1008 Hz, the largest separation ($\Delta z=1.0$ m) between 63 and 504 Hz. The excitation signal was a periodically swept sine (40 to 400 Hz in 0.5 s). The maximum pressure amplitude in the system was about 1.5% of the static pressure. A 400 line FFT was taken of the signals of the pressure transducers with a resolution of 1 Hz. A flat top window was applied to the data and 200 averages were taken.

6.5.1 pump at standstill

At standstill the pump will behave as a passive element, which influences the pulsation transmission in the circuit. The transfer matrix of the pump at standstill is considered to be the reference against which the influence of the operation condition of the pump to the pulsation transmission has been investigated.

The lumped admittances Y_1 and Y_3 and impedance Z_2 of the model of eq.(6.3) are derived from the experimentally determined transfer matrix coefficients: $Y_1=(1-H_{11})/H_{12}$, $Y_3=(1-H_{22})/H_{12}$ and $Z_2=-H_{12}$. A linear least squares fit is used to determine the inductance L_2 and the compliances C_1 and C_3 from the imaginary parts of Z_2 , Y_1 and Y_3 . In the fit only those frequency lines are considered where the coherence function of all measured pressures is greater than 0.95 and where the two-microphone method is insensitive to errors. The fit yields $C_1=4.0\cdot 10^{-12}$ m³/Pa ($\pm 18\%$), $C_3=2.4\cdot 10^{-12}$ m³/Pa ($\pm 50\%$) and $L_2=58\cdot 10^3$ kg/m⁴ ($\pm 23\%$). The inaccuracies given have been derived from the standard deviation of the data in the fitting procedure. Figure 6.8 shows the real and imaginary parts

of the four coefficients of the transfer matrix. The lumped parameter model appears to give a reasonably good approximate description of the transfer matrix. However, a frequency independent resistance term R_2 does not seem to give a realistic model for the damping in the pump. The real part of Z_2 shows an increase near 225 Hz and 375 Hz. This effect might indicate the excitation of mechanical resonances in the pump. This experiment, however, does not give information about the nature of these resonances.

The determinant of the transfer matrix indicates the reliability of the description of the pump as a reciprocal element. The spectrum of the determinant, which is given in figure 6.9, shows a scatter of $\pm 10\%$ around 0.95. Given the accuracy of the results, this implies that the linear description is useful. The accuracy of the results has been investigated by means of a study of the sensitivity to errors in the measured pressure spectra. The analysis has been repeated while one by one each of the measured pressure spectra has been disturbed numerically with an error of $+5\%$ and $+5^\circ$. This disturbance will cause a maximum error in C_1 of $+23\%$, in C_3 of $+42\%$ and in L_2 of -18% . These errors agree with the bounds that were indicated by the fitting procedure. Note that the influence of experimental errors might be reduced by creating more than two independent test states. This overdetermination can be achieved by changing the system impedance [Bolleter *et al.* 1990] or by driving both external sources simultaneously by coherent electrical signals, with a phase delay applied to one of them [Åbom 1992].

The experimentally determined parameter values may be compared to estimations on the basis of the pump geometry and material parameters. The volume of the pump is estimated to be roughly equal to $3 \cdot 10^{-3} \text{ m}^3$. The compliance of an equivalent volume of water at 18°C is $1.4 \cdot 10^{-12} \text{ m}^3/\text{Pa}$. This is substantially smaller than the sum of the experimentally determined compliances $C_1 + C_3 \approx 6.4 \cdot 10^{-12} \text{ m}^3/\text{Pa}$. The difference is too big to be explained from the elasticity of the cast iron pump casing. Since the pump is operating at a low static pressure ($< 2.5 \text{ bar}$), it is more likely caused by the presence of an air pocket in the vertical casing of the pump. A similar effect has been observed in the experiment of France & Bilyk [1993]. The equivalent air volume that corresponds to the measured compliance is $0.7 \cdot 10^{-6} \text{ m}^3$, about 0.02% of the total volume. The inertance L_2 is estimated from $L = \rho V / A^2$, where ρ is the density of the fluid, V is the volume of the pump and A is the area of the inlet and outlet of the pump. This leads to $L_2 = 49 \cdot 10^3 \text{ kg/m}^4$, which agrees with the $56 \cdot 10^3 \text{ kg/m}^4$ ($\pm 21\%$) that has been derived from the measurements.

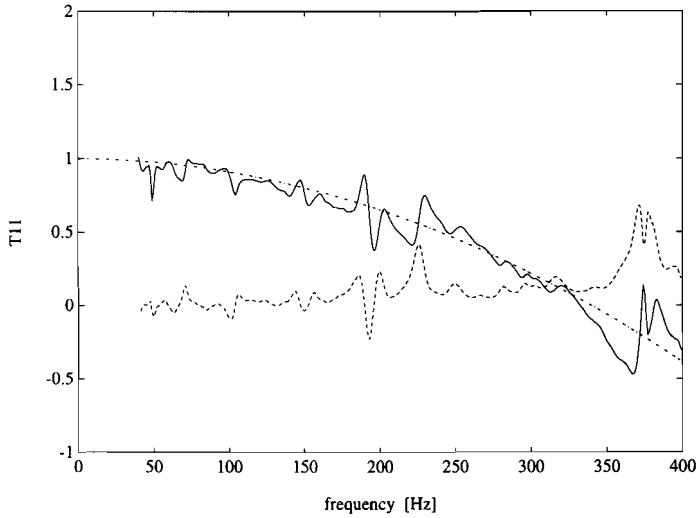


Figure 6.8a: frequency spectrum of coefficient T_{11} of the transfer matrix of the pump at standstill, measured (real part (-), imaginary part (--)) and determined by fitting a lumped parameter model to the measured data (-.).

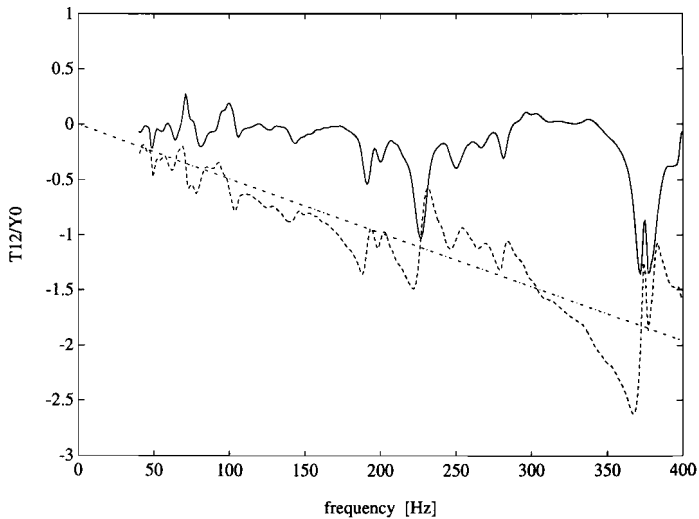


Figure 6.8b: frequency spectrum of coefficient T_{12}/Y_0 of the transfer matrix of the pump at standstill, measured (real part(-), imaginary part (--)) and determined by fitting a lumped parameter model to the measured data (-.).

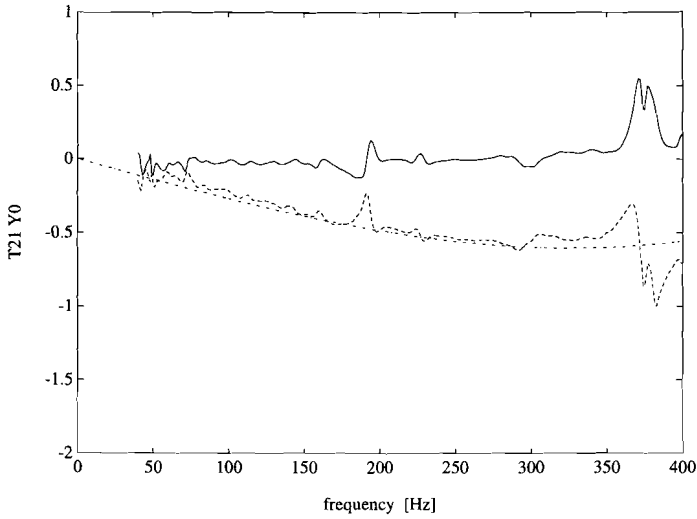


Figure 6.8c: frequency spectrum of coefficient $T_{21}Y_0$ of the transfer matrix of the pump at standstill, measured (real part (-), imaginary part (--)) and determined by fitting a lumped parameter model to the measured data (-.).

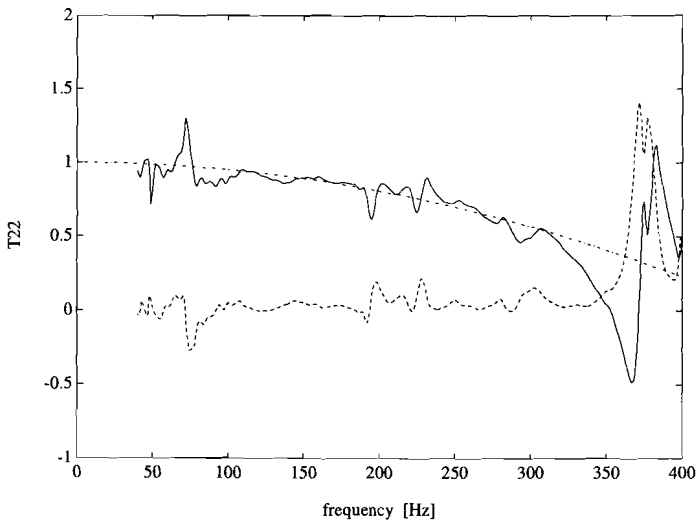


Figure 6.8d: frequency spectrum of coefficient T_{22} of the transfer matrix of the pump at standstill, measured (real part (-), imaginary part (--)) and determined by fitting a lumped parameter model to the measured data (-.).

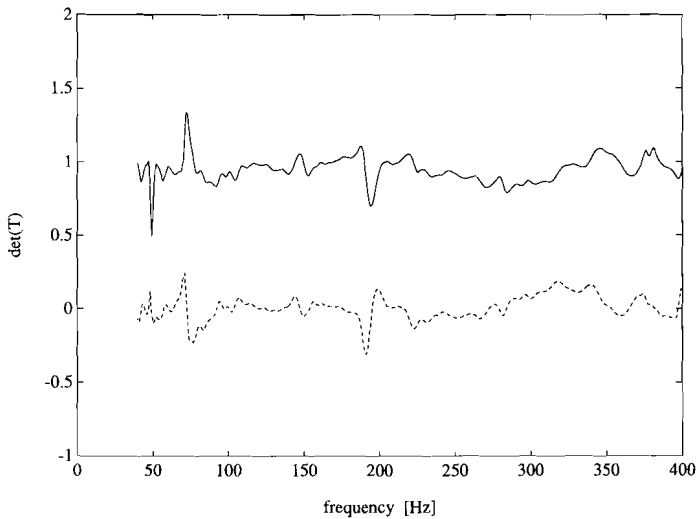


Figure 6.9: real (-) and imaginary (--) frequency spectra of the determinant of the the passive transfer matrix for the pump at standstill.

pump operating

When operating, the pump will act as an active element in the test loop. The pulsation source strength will be discussed in section 6.6. Here we consider the influence of the operating condition of the pump on the passive transfer matrix. In this experiment pump induced pulsations are suppressed by coherence analysis with the external source signal as a reference. Our aim is to identify significant changes in the transfer model parameters that would influence the determination of the source strength vector. Measurements have been performed at three different operating points of the pump at speed $n \approx 24 \text{ s}^{-1}$: close to the pump's best efficiency point ($\Phi=0.14$) and at a low ($\Phi=0.01$) and a high ($\Phi=0.20$) flow rate. Table 6.1 shows the flow data and the lumped parameters that are derived from these measurements. Note that the frequencies at which strong tonal pulsations are generated in the pump (e.g. blade passing frequency, see section 6.6) are rejected in the fitting procedure.

Table 6.1 shows that there is no significant change of the lumped parameters with increasing flow rate. This has been confirmed by measurements at other pump speeds. Even the real part of the series impedance (i.e. the damping) appears to be practically independent of the operation of the pump, the above mentioned 'resonances' at 225 and 375 Hz appear at all four operating points, see figure 6.10.

Φ	$Q \cdot 10^3$ [m ³ /s]	ΔP [bar]	$C_1 \cdot 10^{12}$ [m ³ /Pa]	$C_3 \cdot 10^{12}$ [m ³ /Pa]	$L_2 \cdot 10^{-3}$ [kg/m ⁴]
0	0	0	4.0 ($\pm 18\%$)	2.4 ($\pm 50\%$)	58 ($\pm 23\%$)
0.01	0.58	0.54	3.8 ($\pm 17\%$)	2.1 ($\pm 36\%$)	58 ($\pm 22\%$)
0.14	13	0.40	3.9 ($\pm 16\%$)	2.3 ($\pm 28\%$)	53 ($\pm 22\%$)
0.20	19	0.14	3.7 ($\pm 17\%$)	2.2 ($\pm 30\%$)	53 ($\pm 23\%$)

Table 6.1: lumped compliances C_1 and C_3 and inertance L_2 of the pump at four different operating points (flow rate Φ , actual volume flow Q and pressure difference ΔP).

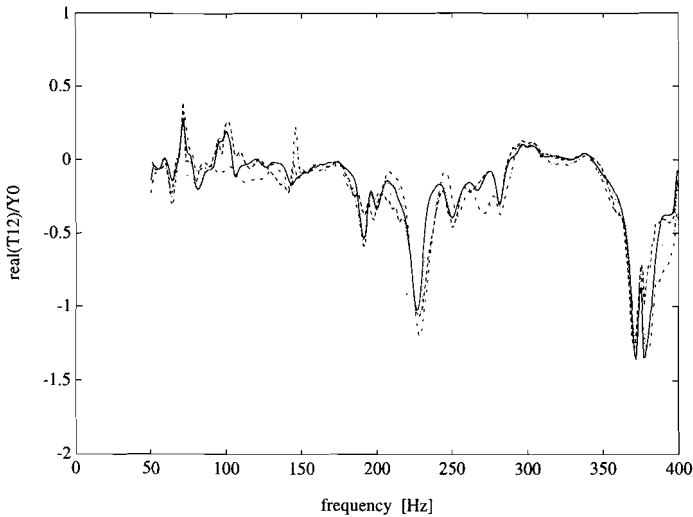


Figure 6.10: real part of T_{12}/Y_0 at four different flow rates: $\Phi=0$ (-), $\Phi=0.01$ (--), $\Phi=0.14$ (..) and $\Phi=0.20$ (-.).

We may conclude from the experimental results that the transmission of low-frequency pulsations through this pump is governed by a transfer matrix that is approximately independent of the operating condition. The matrix coefficients can be described by two compliances C_1 and C_3 and an inertance L_2 . We will use the modelled matrix for the determination of the source strength vector. This has the advantage that the transfer matrix determination does not have to be repeated for all pump operating points. The real part of the series impedance is ignored in the model. Consequently the damping will be reflected in the measurements as a negative pulsation source strength (a sink) in the pump.

6.6 Experimental determination of the fluid pulsation source strength

Once the passive transfer matrix for the pump is known, the pulsation source strength of the pump can be determined. With the external sources switched off, the source strength vector is derived from pressures and volume velocities at the suction and discharge ports, using eq.(6.1).

Let us first consider a typical pressure spectrum as it is measured in the discharge pipe of the pump. Figure 6.11 shows the auto-power spectrum of the pressures at the measurement position 'd1' in the discharge pipe and 's3' in the suction pipe (see fig.6.4). The spectra are dominated by strong tonals at the blade passing frequency (145 Hz) and its first harmonic (290 Hz). They further show much weaker tonals at harmonics of the pump speed and a broad-band noise spectrum. The influence of resonances in the pipe system on the spectrum can be seen in the minimum near 210 Hz, that indicates a local node in the pressure. Both the tone and the broadband noise near the blade passing frequency appear to be enhanced by a resonance.

The use of an inverse method to determine the source strength vector requires a high coherence of the measured pressures. Non-perfect coherence may be caused by disturbing noise in the measurements, for example caused by the turbulent flow across the surface of the pressure transducers. It may also indicate that more than one, incoherent, source mechanism is responsible for noise generation in the pump [Åbom *et al.* 1992; Okamoto 1993] or that the source mechanism is not linear, which is not unlikely for flow-induced noise. Figure 6.11 shows both the coherent part ($\gamma_{xy}^2 G_{yy}$) and the incoherent part ($(1 - \gamma_{xy}^2) G_{yy}$) of the pressure. The acceleration of the piston of the external source in the suction pipe (fig.6.5) has been used as a reference signal. When the source is turned off the piston follows the pressure pulsations in the fluid and it is not disturbed by flow noise. The coherence function between the piston acceleration and the pressure in the suction pipe appeared to be higher than the coherence function between pressures across the pump. The higher level of incoherent pressure fluctuations in the discharge pipe might be caused by a more disturbed flow after passing through the pump. However, the dominant tonals and the broadband noise around the blade passing frequency are coherent across the pump. This means that the source strength will be determined correctly at these frequencies. The coherence function gives no significant evidence of multiple incoherent source mechanisms or non-linearities at these frequencies.

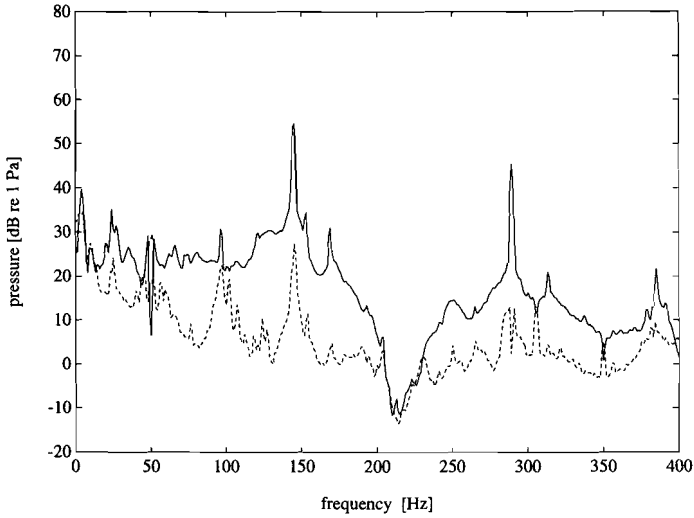


Figure 6.11a: coherent (-) and incoherent (--) auto-power spectra of the pressure at position 's3', with the pump running ($n=24.14$ rps; $Q=0.013$ m³/s; $\Delta P=0.40$ bar; $\Delta f=1$ Hz).

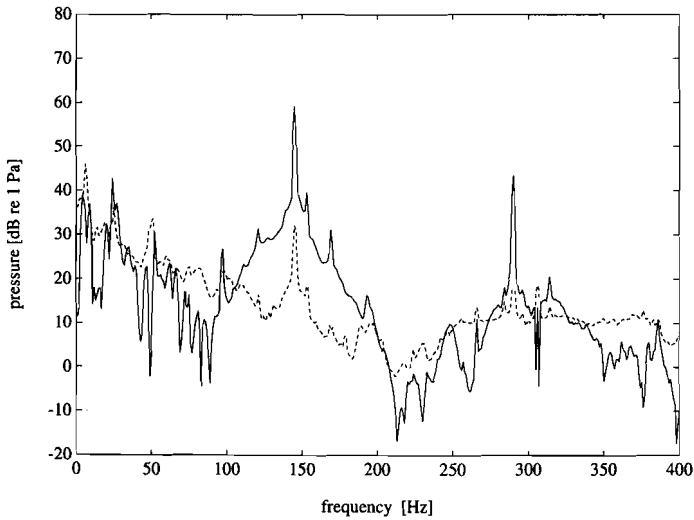


Figure 6.11b: coherent (-) and incoherent (--) auto-power spectra of the pressure at position 'd1', with the pump running ($n=24.14$ rps; $Q=0.013$ m³/s; $\Delta P=0.40$ bar; $\Delta f=1$ Hz).

The magnitudes of the two components of the source strength vector are shown in figure 6.12. They give a much clearer picture of the tonal phenomena that are generated by the pump. Compared to the directly measured pressure spectra of figure 6.11 more harmonics of the shaft rotation frequency can be recognised. They are indicated by their order number in fig.6.12. In the pressure source strength, the first harmonic of the blade passing frequency (order 12) displays sidebands (indicated by '*') at ± 6 Hz. These might be caused by a low frequency whirl motion of the pump shaft, which seems to be supported by the presence of a peak at 6 Hz. Near the harmonics of the blade passing frequency (orders 6 and 12) one can observe an extra tonal phenomenon (indicated by '+'), which is most clear in the volume velocity source strength. There is no integer relationship between the frequency of this phenomenon and the shaft rotation frequency, but it is closely related to the harmonics of the blade passing frequency. It occurs at 1.055 times these frequencies. It is not clear what mechanism is responsible for these particular peaks.

The source mechanism can be investigated by comparing the non-dimensional ratio $Y_0 \Delta q / \Delta p$ of the monopole (Δq) and dipole (Δp) components of the source vector, where Y_0 ($=A_p / \rho_f c_f$) is the specific admittance for plane waves in the suction and discharge pipes. In an infinitely long pipe the monopole and dipole sources will generate travelling waves with equal amplitudes if this non-dimensional ratio is equal to one. The ratio depends not only on the source mechanisms, but also on the transfer from the actual source position in the pump to the position of the equivalent source vector at the outlet port. In the worst case the actual source may be located at the inlet port. Equation (6.1) can be rewritten for this case:

$$\begin{pmatrix} p_d(\omega) \\ q_d(\omega) \end{pmatrix} = \begin{bmatrix} H_{11}(\omega) & H_{12}(\omega) \\ H_{21}(\omega) & H_{22}(\omega) \end{bmatrix} \begin{pmatrix} p_s(\omega) + \Delta p_{\text{inlet}}(\omega) \\ q_s(\omega) + \Delta q_{\text{inlet}}(\omega) \end{pmatrix} \quad (6.8)$$

Hence, the inlet source vector can easily be derived from the outlet source vector:

$$\begin{pmatrix} \Delta p_{\text{inlet}} \\ \Delta q_{\text{inlet}} \end{pmatrix} = [H]^{-1} \begin{pmatrix} \Delta p \\ \Delta q \end{pmatrix} \quad (6.9)$$

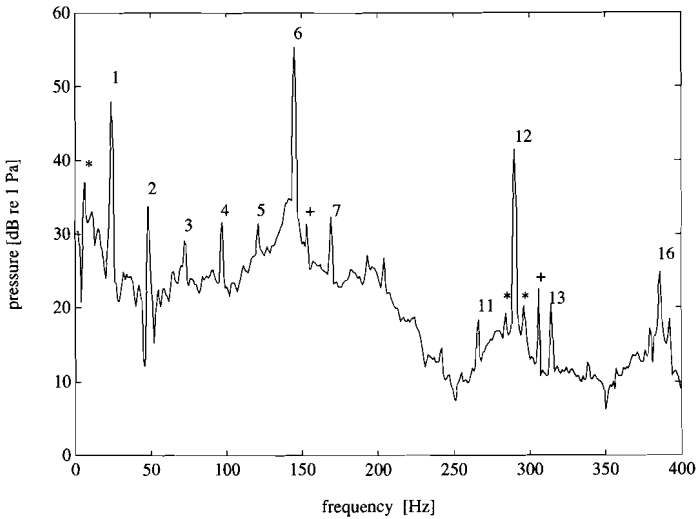


Figure 6.12a: auto-power spectrum of the pressure source strength for the pump operated at its design point ($n=24.14$ rps; $Q=0.013$ m³/s; $\Delta P=0.40$ bar; $\Delta f=1$ Hz). The numbers refer to orders of the shaft rotation frequency (see the text for the symbols + and *).

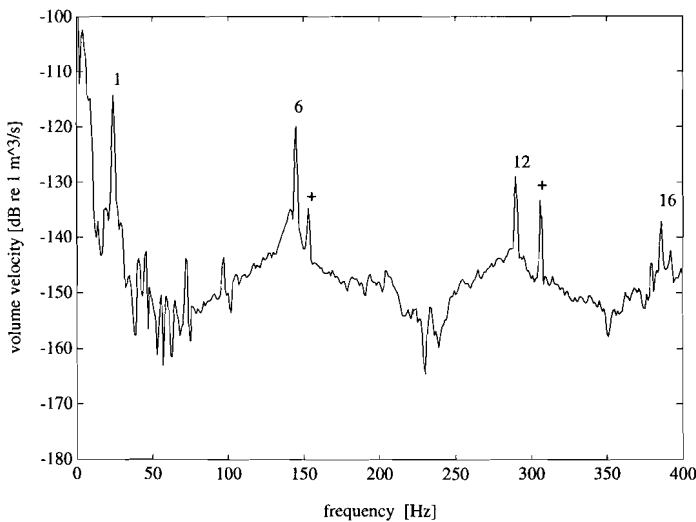


Figure 6.12b: auto-power spectrum of the volume velocity source strength for the pump operated at its design point. The numbers refer to orders of the shaft rotation frequency (see the text for the symbol +).

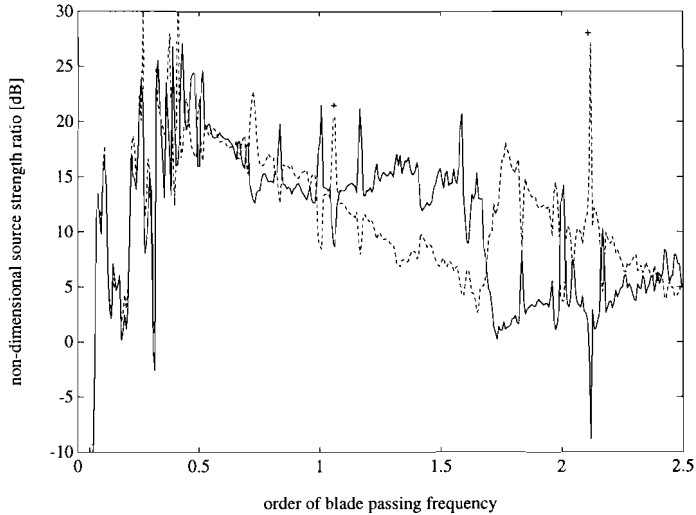


Figure 6.13: non-dimensional ratio $Y_o|\Delta p/\Delta q|$ of the source vector components, for sources located at the outlet (-) or at the inlet (--) of the pump, using eq.(6.8).

Figure 6.13 shows the non-dimensional ratio of the source vector amplitudes for both the outlet and the inlet source vector. The predominant source mechanisms appear to be fluctuating forces (dipole type).

Note: This finding contradicts the results of Chatel et al. [1993], who conclude from a reciprocity experiment that the dipole type source mechanism has a negligible contribution to the noise that is transmitted in the outlet pipe of the pump. However, this reciprocity experiment is based upon an incorrect model in which the fluctuating force with which the impeller acts on the fluid is represented by an acoustic dipole in front of an impeller blade, instead of the pressure difference across the impeller.

The dipole source strength at the tonals at harmonics of the shaft rotation frequency is largest for the outlet source vector, which suggests that these tones are generated near the outlet port. This supports the idea that the interaction of the flow around the impeller blades with the fixed volute tongue is the main source of pressure pulsations in the centrifugal pump (see e.g. [Guelich & Bolleter 1992]). On the other hand, the above mentioned phenomenon related to the blade passing frequency (indicated by '+') seems to be of dipole type and generated near the inlet port. Based on the available information it is not possible to identify the generating mechanism. Since the objective of the experiments was only to show the practicability of the source characterization method, we have not further investigated this phenomenon.

The error sensitivity of the results has been tested by applying numerical errors to the input data. The random errors due to non-perfect coherence in the measured pressures are estimated on the basis of the coherence function [Bendat & Piersol 1980]. These errors result in a maximum error of 5% in the magnitude of the source vector. The pressure source strength is not very sensitive to errors in the lumped parameters for the transfer matrix model. A 20% error in C_1 or L_2 or a 50% error in C_3 results in a maximum error of 20% in Δp . The maximum error in $\Delta q/Y_0$, that is small compared to Δp , is 50%. Using the actually measured transfer matrix instead of the lumped parameter model matrix results in similar errors. The linearity of the source strength has been tested by repeating the measurements at a different acoustic load of the pump. For this purpose the butterfly valve in front of the discharge source (see fig.6.4) has been opened in the second measurement, while it was closed during the first. Opening this valve mainly affects the system resonance near 140 Hz. Therefore we only compare the levels at the blade passing frequency. The magnitude at the peak has been estimated with the help of a Hanning-window based interpolation technique [Burgess 1975]. The rms-pressure levels ($|p_s|$ and $|p_d|$) at the suction and discharge ports respectively and the pressure source strength ($|\Delta p|$) at the two loads are:

- valve closed:	$ p_s =169$ Pa;	$ p_d =741$ Pa;	$ \Delta p =590$ Pa
- valve open:	$ p_s =168$ Pa;	$ p_d =229$ Pa;	$ \Delta p =504$ Pa

Opening the valve causes the outlet pressure to decrease by a factor 3.2. This shows again that the system response has a large influence on the pressure levels in the pipes. The resulting pressure source strength Δp shows only a 17% difference. This difference is of the same order of magnitude as the 20% error that might be expected on the basis of the error sensitivity. An accuracy of 20% (1.6 dB) for the dominant component of the source vector is considered to be sufficiently small to accept the method that is presented here as a means to achieve a useful estimate of the source strength of the pump.

6.6.1 source strength at different operating conditions

Now the source characterization method can be used to investigate the source strength at different operating conditions of the pump. A detailed study of the pulsation generation in the centrifugal pump falls beyond the scope of this thesis, but we will show some trends and investigate the scaling of the pulsation source strength. The operating conditions are varied through independent variation of the pump speed and the flow resistance using a valve in the discharge line (see fig.6.4). To facilitate the comparison we will scale the source pressure and volume velocity with a dynamic pressure, based on the circumferential impeller velocity V_{tip} :

$$\Delta \hat{p} = \frac{\Delta p}{\frac{1}{2} \rho V_{tip}^2}, \quad \Delta \hat{q} = \frac{\Delta q}{\frac{1}{2} \rho V_{tip}^2 Y_o} \quad (6.10)$$

First we will compare the source strength at the pump's best efficiency point, as determined above, to the source strength at two extreme operating conditions. Figure 6.14 shows the non-dimensional pressure source strength for the pump operating near its best efficiency point ($\Phi=0.14$, solid line), at partial flow ($\Phi=0.01$, dashed line) and at large flow ($\Phi=0.20$, dotted line). Both extreme operating conditions show an increased source strength. Especially at partial flow, flow separation and recirculation in the impeller [Guelich & Bolleter 1992] cause a strong increase of the broadband noise level.

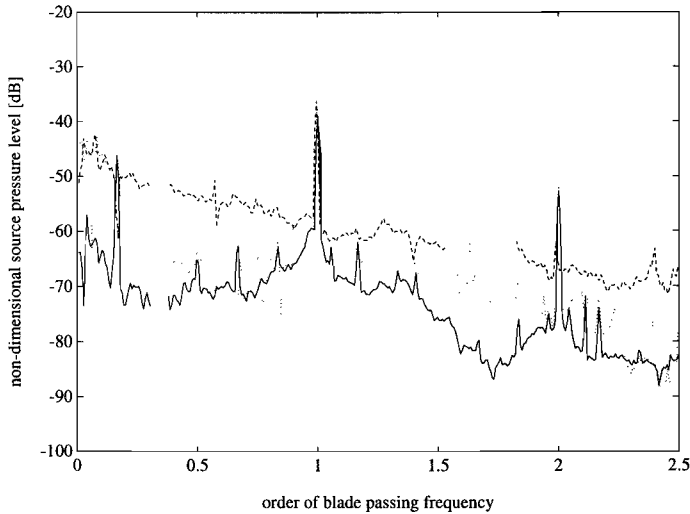


Figure 6.14: non-dimensional spectrum of the pressure source strength, scaled with $\frac{1}{2}\rho V_{tip}^2$, versus the order of the blade passing frequency, for the pump operating at three different conditions: $\Phi=0.14$ (-), $\Phi=0.01$ (--) and $\Phi=0.20$ (..), at pump speed $n=24$ rps ($\Delta f=1$ Hz).

The source level at the blade passing frequency ($f/n=6$) has been determined at a range of flow rates at shaft rotation frequency $n=24$ Hz. Figure 6.15 shows the non-dimensional pressure and volume velocity source strengths as a function of the flow rate Φ (eq.6.6). The comparison of $\Delta \hat{p}$ and $\Delta \hat{q}$ (see eq.5.10) confirms that the source mechanism is of the dipole type. The source level shows a maximum variation of 9 dB. The minimum source strength is found at a flow rate ($\Phi \approx 0.05$) far below nominal flow ($\Phi=0.14$). This effect has also been observed by Tourret *et al.* [1985] for a pump that was installed between

anechoic terminations to reduce the effect of system resonances. It contradicts Bartenwerfer's [1980] assumption that the source strength is minimal at the best efficiency point Φ_{BEP} and approximately increases proportional to $(\Phi - \Phi_{\text{BEP}})^2$ away from this point. Bartenwerfer's assumption seems to be supported by statistical data on pressure pulsations of 36 pumps in different loops [Guelich & Bolleter 1992], but it is not clear to what extent these data are influenced by the system response.

Figure 6.16 shows the source strength at a constant flow rate ($\Phi \approx 0.13$) as a function of the rotating speed. The shaft rotation frequency n has been scaled with a reference frequency $n_0 = 50$ Hz. Again the pressure source strength is dominant over the volume velocity source strength. The non-dimensional pressure source strength shows nearly 20 dB variation. Note however that the volume velocity source strength is found to be rather high at the minimum pressure source strength.

It is interesting to compare the measured source strength levels to predictions based on the only prediction model that is currently available: the correlation formula by Simpson *et al.* [1966-67]. This formula predicts the pressure level at the blade passing frequency for operation at the pump's design point:

$$L_p = 35 \log(\Delta P) + 10 \log(Q) - 40 \log(n) - 20 \log((D/2)^2 b) - 116 \quad (6.11)$$

with:

L_p = source pressure at blade passing frequency [dB re 1 Pa]

ΔP = pressure rise across the pump [Pa]

Q = volume flow through the pump [m^3/s]

n = shaft rotation frequency [Hz]

D = outer diameter of the impeller [m]

b = width of the impeller at the outlet [m]

This formula predicts that the source pressure will vary in proportion to n^2 at a constant non-dimensional flow rate Φ [Bartenwerfer 1980], hence that the non-dimensional source pressure $\Delta p / \frac{1}{2} \rho V_{\text{tip}}^2$ will be independent of n . At $\Phi = 0.13$ equation (6.11) predicts a non-dimensional source pressure level of -43 dB. This value agrees very well with the measured source pressure for n/n_0 in the range of 0.68 to 0.85 (see fig.6.16), but the measured data outside this range show significant deviations from the predicted source strength.

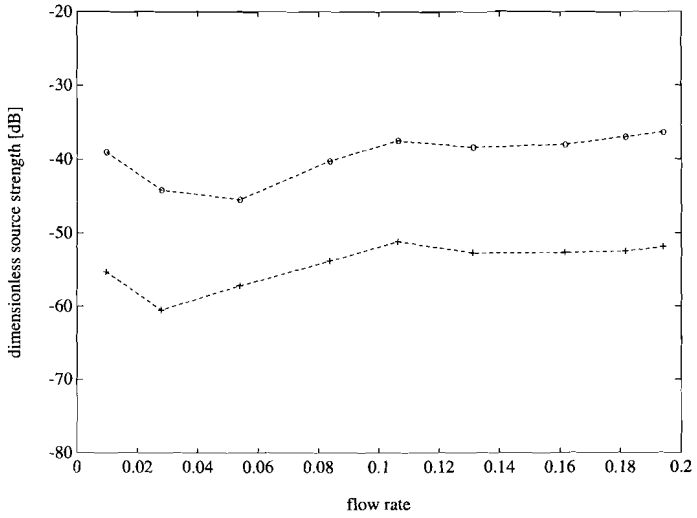


Figure 6.15: non-dimensional source strength vector components Δp (o) and $\Delta q/Y_0$ (+) at the blade passing frequency, versus flow rate Φ , at pump speed $n=24$ rps.

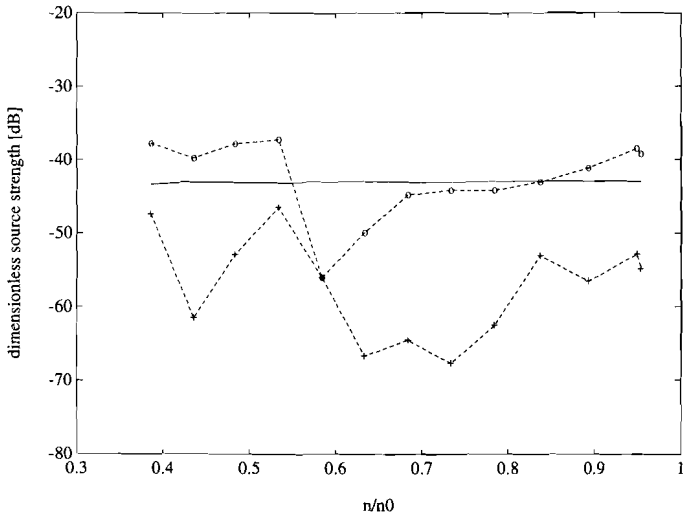


Figure 6.16: non-dimensional source strength vector components Δp (o) and $\Delta q/Y_0$ (+) at the blade passing frequency, versus shaft rotation frequency n/n_0 ($n_0=50$), at flow rate $\Phi=0.13$. The solid line shows the predicted level according to eq.(6.11)

6.7 Conclusion

In this chapter we have presented the application of an experimental inverse method to characterize a centrifugal pump as a source and a transmission path of fluid pulsations. A test loop has been designed in which this method has been tested on a single stage pump.

Pressure pulsations have been measured in the suction and discharge pipes, using two acceleration compensated, flush mounted, piezo-electric pressure transducers per pipe cross-section. This configuration the disturbing effect of transverse vibrations of the pipes on the pressure measurements.

The measured pressure signals have been shown to be sufficiently stable to be able to rely on successively measured data for the inverse measurement method. The linearity of the pulsations in the system and the accuracy of the measurement method have been investigated.

It has been shown that the transmission of pulsations through a centrifugal pump can be characterized by a linear transfer matrix. For the pump under investigation this frequency-dependent matrix appears to be approximately independent of the operating condition. As shown before by Stirnemann *et al.* [1978], the coefficients of this matrix can be related to the lumped compliances and inertance of a simple lumped network model, at low frequencies. The inertance appears to agree with the value that may be estimated on the basis of the pump geometry. The experimentally determined compliance is nearly five times larger than expected, probably due to the presence of a small air pocket in the pump.

The generation of pulsations in the pump has been characterized by an equivalent source vector, consisting of a monopole and a dipole source strength. The spectra of the source strengths give a much clearer picture of the pulsations that are generated in the pump than the pressure spectra that are measured in the suction and discharge pipes. The results of experiments on a single stage centrifugal pump confirm that fluctuating forces (dipole type sources) form the dominating source mechanism in the pump, if no cavitation occurs. We have been able to determine the source strength with an accuracy of about 20%. It is shown that the source strength depends on the operating condition of the pump. Simpson's correlation formula [Simpson *et al.* 1966-67], the only tool that is presently available for estimation of the source strength of centrifugal pumps, appears to give a reasonable first approximation for the source strength at the blade passing frequency when the pump is operating at its design point. However, it does not give information on the source strength at other frequencies and operating conditions. The results of the experimental method show that, for off-design conditions, the actual source strength deviates by up to 13 dB from the

predicted value.

Of course measurements on a single pump in a single test loop do not allow general conclusions. The practicability of the method that is presented here will have to be proved by further application. It promises to be an interesting tool for investigation of pulsation generation in centrifugal pumps. In combination with detailed measurements or calculations of the complex flow field in the pump it can help to identify quantitative relationships between the flow field in the pump and the generation of pressure waves in the piping.

7. EVALUATION

In the literature there is only limited information available on the mechanisms which are responsible for the generation and transmission of fluid pulsations and mechanical vibrations in pipe systems. This thesis presents some useful tools for the analysis of these mechanisms.

While fluid pulsations and mechanical vibrations in gas-filled pipes can usually be treated separately, a strong coupling can occur in flexible pipe systems filled with a fluid for which the mass per unit pipe length is of the same order of magnitude as that of the pipe. This coupling requires a simultaneous analysis of fluid pulsations and pipe vibrations. At higher frequencies the coupled behaviour will generally be so complex that it can only be described in terms of spatial and temporal averaged quantities, using a statistical method, like SEA [Lyon 1975]. However, many practical problems occur at lower frequencies where strong tonal phenomena (e.g. blade passage tones of a centrifugal pump) may excite resonant modes of the pipe system. For this type of problem a deterministic method is more appropriate. The methods that have been developed in this study aim primarily at a deterministic analysis of the coupled, linear elastic, dynamic behaviour of pipe systems filled with a heavy, homogeneous fluid (e.g. water or oil).

Prediction method for the dynamic behaviour of a pipe system

The linear dynamic behaviour of fluid-filled pipe systems can now be predicted, using the computer program *PRESTO*, that is based on the transfer matrix method (TMM). Unlike the few TMM models for pipe systems that have been described in the literature, it is based on a detailed study of the propagation of fluid-borne and structure-borne waves in fluid-filled cylindrical shells. Analytical expressions have been obtained for the transfer matrix coefficients of several pipe system components (straight pipes, elbows, pipe supports, etc.). The sensitivity of the method to input errors has been evaluated and a method has been described to control the convergence of the program with respect to numerical round-off errors. Numerical examples confirm that the interaction of pulsations and vibrations has significant effects on the resonance frequencies and pulsation and vibration levels at resonance when normal modes of fluid and structure closely coincide.

The TMM is a useful tool to investigate coupled pulsations and vibrations in pipe systems of not too complex geometry. It is particularly suited for treating systems that can be modelled as a linear cascade of components. The modelling of branched systems and systems with pipe loops requires further investigation. One of the main advantages of the TMM is that the transfer matrix coefficients of pipe system components can be obtained

by different methods. Where possible, analytical expressions should be used (as derived for straight and curved pipes). The transfer matrices of components that cannot be described analytically can be derived experimentally. However, the introduction of experimentally determined transfer matrices in the TMM model may seriously influence the accuracy of the results. This problem requires further investigations. Another option is to use the Finite Element Method to determine the transfer matrix of components for which no analytical expressions are available. It would be an interesting extension of the present study to investigate this option.

Validation experiments have been performed on two simple pipe systems: a straight pipe and a system consisting of two straight pipes connected by an elbow. These experiments contribute to the limited experimental data that are available in literature, where the experiments of Davidson *et al.* [1969;1972] are still used as a benchmark. Predictions of the dynamic behaviour of these systems (using the TMM) appeared to agree reasonably well with the results of measurements. As for all calculation methods, the major difficulty is to obtain accurate input data, especially for the boundary conditions and the damping in the system. The accuracy of the calculated response might be improved by using measured data to establish correct input data. Nevertheless, the results of the calculations provide insight into the dynamic behaviour of a pipe system that cannot be obtained as easily from measurements. Calculations can be performed in the design stage, so that problems can be identified and modifications to the design can be evaluated before the construction of the system. Model calculations can also be used to evaluate experimental methods with respect to their applicability and accuracy.

Experimental methods

An important achievement of the experimental methods that are described in this study is the correct decomposition of the measured signals into wave amplitudes, using the signals of multiple transducers (accelerometers, pressure transducers). This decomposition is essential for the interpretation of measurements on a pipe, because each measured signal may consist of contributions of several types of waves. Once this wave decomposition has been performed, the wave amplitudes give information on, for example, the amount of vibro-acoustic energy that is transmitted in each wave. Using this method, it is possible to identify sources and predominant transmission paths of pulsations and vibrations.

The vibro-acoustic source strength and transmission characteristics of pipe system components can only be derived in a well-defined pipe system. In-situ measurements are always influenced by the response of the pipe system. In this thesis the effects of system response are removed by means of an 'inverse' method. Such a method involves a series of measurements on different system configurations. Different configurations can be

obtained by geometrical changes, e.g. by opening valves or disconnecting pipes or pipe supports from the system, (i.e. the 'two-load method', as suggested by Kathurija & Munjal [1976]) or by artificial excitation of the system (i.e. the 'two-source-location method', as suggested by Munjal & Doige [1990]).

Two examples of the application of an inverse method have been presented in this thesis: the determination of the 2×2 axial mobility matrix of a mass at the end of a straight pipe (section 5.2.3) and the determination of the 2×2 fluid pulsation transfer matrix of a centrifugal pump and the source vector to match (sections 6.5 and 6.6). These examples demonstrate that such a method can indeed be used. Further investigations are required to investigate whether it is possible to use an inverse method to determine a larger matrix or the source vector of a source which excites mechanical vibrations in more than one degree of freedom. To determine more matrix or vector coefficients will require measurements on more system configurations. It would be interesting to establish what the limitations are (with respect to matrix size, maximum frequency, measurement accuracy, etc.) to the applicability of the inverse method.

It has been shown that an inverse method can be applied to investigate the generation of fluid pulsations in a centrifugal pump as a function of its operating condition. This experiment gives evidence that a centrifugal pump, in the absence of cavitation, imposes fluctuating forces on the fluid at harmonics of its blade passing frequency. This implies that the pump may be modelled as a dipole source of pulsations. As far as the author knows, experimental evidence for this has not been published before (see [Bolleter 1993]). The characterization method may be of interest for the design of pumps, to investigate experimentally the influence of modifications in the design on the generation of fluid pulsations. The method might also be used for condition monitoring of pumps. Further investigations should reveal which relationships exist between the acoustic source strength and specific defects in the pump. Finally the quantitative information on the source and transmission characteristics of the pump can be used directly as input to the *PRESTO* program, to predict the vibrational response of the circuit in which the pump will be installed.

APPENDIX A: Numerical solution of the dispersion equation

Following Pavić [1990] the dispersion equation (eq.2.22) is solved numerically, using the series expansion for the Bessel functions in the dimensionless wavenumber $\kappa=k_{mn}a$:

$$FL = \Omega^2 \frac{\rho_f a_i^2}{\rho_s a h} \frac{\sum_{j=0}^{\infty} C1_{nj} (\Psi \Omega^2 - \kappa^2)^j}{\sum_{j=0}^{\infty} (2j+n) C1_{nj} (\Psi \Omega^2 - \kappa^2)^j}, \quad \text{with} \quad C1_{nj} = \frac{(-1/4)^j}{j!(n+j)!}. \quad (\text{A.1})$$

Eq.(2.20) has been used to eliminate the radial wavenumbers γ_{mn} . The dimensionless parameter Ψ is defined as the ratio of the plate wave speed c_p in the pipe wall and the free wave speed in the fluid c_o squared: $\Psi=(c_p/c_o)^2$ and the superscript "i" referring to the internal fluid has been omitted.

Equation (A.1) can be rewritten in the form:

$$FL = \Omega^2 \frac{\rho_f a_i^2}{\rho_s a h} \frac{\sum_{k=0}^{\infty} C2_{nk} (\kappa^2)^k}{\sum_{k=0}^{\infty} C3_{nk} (\kappa^2)^k}, \quad (\text{A.2})$$

with:

$$C2_{nk} = (-1)^k \sum_{j=k}^{\infty} \binom{j}{k} (\Psi \Omega^2)^{j-k} C1_{nj}, \quad (\text{A.3})$$

$$C3_{nk} = (-1)^k \sum_{j=k}^{\infty} \binom{j}{k} (\Psi \Omega^2)^{j-k} (2j+n) C1_{nj}.$$

The dispersion equation can be expanded in κ^2 :

$$\sum_{j=0}^4 C4_{nj} (\kappa^2)^j = FL \sum_{j=0}^2 C5_{nj} (\kappa^2)^j, \quad (\text{A.4})$$

where the factors $C4_{nj}$ and $C5_{nj}$ can be derived from the matrix elements L , eq.(2.24), for each set of shell equations.

Without fluid-loading ($FL=0$) the dispersion equation reduces to an eighth order poly-

nomial equation in κ^2 . For fluid-filled pipes substitution of eq.(A.2) into eq.(A.4) results in a polynomial equation of infinite order:

$$\sum_{k=0}^{\infty} \left\{ \sum_{j=0}^4 C4_{nj} C3_{n(k-j)} - \Omega^2 \frac{\rho_f a_i^2}{\rho_s a h} \sum_{j=0}^2 C5_{nj} C2_{n(k-j)} \right\} (\kappa^2)^k, \quad (\text{A.5})$$

where the coefficients $C3_{n(k-j)}$ and $C3_{n(k-j)}$ are equal to zero for $k < j$.

It can be shown that a truncation of the series expansion in equation (A.4) after 20 terms leads to sufficiently accurate wavenumbers for $\Omega < 1$. The resulting polynomial equation has been solved numerically, using the companion matrix method. Pavić [1990] gives the results of a similar numerical solution method for determining the dispersion equation, based on the Flügge equations. Our computer program, that can be used for any set of shell equations, has been tested by the reproduction of Pavić's results.

APPENDIX B: Derivation of the beam model for a straight fluid-filled pipe

State variables

The state variables for a quasi one-dimensional model of the straight fluid-filled pipe are obtained by integration of the local shell and fluid variables over the pipe cross-section. At low frequencies membrane stresses are predominant so that the local bending and radial shear stiffness of the shell may be neglected. Figure 2.3 shows the orientation of the local and averaged variables, which are related through:

$$\bar{u}_x = \frac{1}{2\pi} \int_0^{2\pi} (w \cos\theta - v \sin\theta) d\theta \quad , \quad \bar{F}_x = - \int_0^{2\pi} N_{z\theta} \sin\theta a d\theta \quad , \quad (\text{B.1})$$

$$\bar{u}_y = \frac{1}{2\pi} \int_0^{2\pi} (w \sin\theta + v \cos\theta) d\theta \quad , \quad \bar{F}_y = \int_0^{2\pi} N_{z\theta} \cos\theta a d\theta \quad , \quad (\text{B.2})$$

$$\bar{u}_z = \frac{1}{2\pi} \int_0^{2\pi} u d\theta \quad , \quad \bar{F}_z = \int_0^{2\pi} N_z a d\theta \quad , \quad (\text{B.3})$$

$$\bar{\phi}_x = \frac{1}{2\pi} \int_0^{2\pi} \frac{u}{a \sin\theta} d\theta \quad , \quad \bar{M}_x = \int_0^{2\pi} N_z a^2 \sin\theta d\theta \quad , \quad (\text{B.4})$$

$$\bar{\phi}_y = - \frac{1}{2\pi} \int_0^{2\pi} \frac{u}{a \cos\theta} d\theta \quad , \quad \bar{M}_y = - \int_0^{2\pi} N_z a^2 \cos\theta d\theta \quad , \quad (\text{B.5})$$

$$\bar{\phi}_z = \frac{1}{2\pi} \int_0^{2\pi} \frac{v}{a} d\theta \quad , \quad \bar{M}_z = \int_0^{2\pi} N_{z\theta} a^2 d\theta \quad , \quad (\text{B.6})$$

$$\bar{v}_f = \frac{1}{\pi a_1} \int_0^{2\pi} \int_0^{a_1} \xi_z r dr d\theta \quad , \quad \bar{p} = \frac{1}{\pi a_1} \int_0^{2\pi} \int_0^{a_1} p r dr d\theta \quad . \quad (\text{B.7})$$

The dependence on r and θ is suppressed in the integration process. Substitution of the circumferential mode expansion (eq.2.15) into the equations (B.1-7) yields:

$$\begin{aligned}
\bar{u}_x &= \frac{1}{2}(\hat{w}_1 - i\hat{v}_1), & \bar{u}_y &= \frac{1}{2}(i\hat{w}_1 + \hat{v}_1), & \bar{u}_z &= \hat{u}_0, \\
\bar{F}_x &= -i\pi a(\hat{N}_{z\theta})_1, & \bar{F}_y &= \pi a(\hat{N}_{z\theta})_1, & \bar{F}_z &= 2\pi a(\hat{N}_z)_0, \\
\bar{\phi}_x &= i\hat{u}_1/a, & \bar{\phi}_y &= -\hat{u}_1/a, & \bar{\phi}_z &= \hat{v}_0/a, \\
\bar{M}_x &= i\pi a^2(\hat{N}_z)_1, & \bar{M}_y &= -\pi a^2(\hat{N}_z)_1, & \bar{M}_z &= 2\pi a^2(\hat{N}_{z\theta})_0, \\
\bar{p} &\approx \hat{p}_0, & \bar{v}_f &\approx \xi_0.
\end{aligned} \tag{B.8}$$

As expected, the contributions of all modes $n>1$ disappear in the integration.

Equations of motion:

Neglecting bending stiffness, the stress-strain equations (eq.2.3) yield:

$$\begin{aligned}
(\hat{N}_z)_0 &= \frac{E_s}{1-\nu^2} \left(\frac{\partial \hat{u}_0}{\partial z} + \nu \frac{\hat{w}_0}{a} \right), & (\hat{N}_z)_1 &= \frac{E_s}{1-\nu^2} \left(\frac{\partial \hat{u}_1}{\partial z} + \nu \frac{i\hat{v}_0 + \hat{w}_0}{a} \right), \\
(\hat{N}_{z\theta})_0 &= \frac{E_s}{2(1+\nu)} \frac{\partial \hat{v}_0}{\partial z}, & (\hat{N}_{z\theta})_1 &= \frac{E_s}{2(1+\nu)} \left(\frac{\partial \hat{v}_1}{\partial z} + i \frac{\hat{u}_1}{a} \right).
\end{aligned} \tag{B.9}$$

And the equations of motion (eq.2.8) yield:

$$\begin{aligned}
\frac{\partial (\hat{N}_z)_0}{\partial z} &= -\rho_s h \omega^2 \hat{u}_0, & \frac{\partial (\hat{N}_z)_1}{\partial z} + i \frac{(\hat{N}_{z\theta})_1}{a} &= -\rho_s h \omega^2 \hat{u}_1, \\
\frac{\partial (\hat{N}_{z\theta})_0}{\partial z} &= -\rho_s h \hat{v}_0, & \frac{\partial (\hat{N}_{z\theta})_1}{\partial z} &= -\rho_s h \omega^2 (\hat{v}_1 + i\hat{w}_1) - i \frac{a_i}{a} \hat{p}_1(a_i), \\
\frac{a_i}{a} \hat{p}_0(a_i) &= \frac{E_s}{1-\nu^2} \frac{h}{a} \left(\frac{\hat{w}_0}{a} + \nu \frac{\partial \hat{u}_0}{\partial z} \right) - \rho_s h \omega^2 \hat{w}_0.
\end{aligned} \tag{B.10}$$

The fluid equations (2.9-11) result in:

$$\frac{\partial \hat{p}_0}{\partial z} = \rho_f \omega^2 \xi_{z0}, \quad \frac{\partial \xi_{z0}}{\partial z} = -\frac{\hat{p}_0}{K_f} - \frac{1}{\rho_f \omega^2 r} \frac{\partial}{\partial r} \left(r \frac{\partial \hat{p}_0}{\partial r} \right). \tag{B.11}$$

And the equation of compatibility, eq.(2.13), yields:

$$\frac{\partial \hat{p}_0(a_i)}{\partial r} = \rho_f \omega^2 \hat{w}_0, \quad \frac{\partial \hat{p}_1(a_i)}{\partial r} = \rho_f \omega^2 \hat{w}_1. \quad (\text{B.12})$$

Using the Bessel function approximation for a small argument γa_i leads to

$$\hat{p}_0(a_i) \approx \bar{p}_0, \quad \hat{p}_1(a_i) \approx a_i \rho_f \omega^2 \hat{w}_1 \quad (\text{B.13})$$

and the integration (eq.B.7) of the fluid equations (B.11) over the fluid area results in:

$$\frac{\partial \bar{p}}{\partial z} = \rho_f \omega^2 \bar{v}_f, \quad \frac{\partial \bar{v}_f}{\partial z} = -\frac{\bar{p}}{K_f} - \frac{2 \hat{w}_0}{a_i}. \quad (\text{B.14})$$

Beam equations

The quasi one-dimensional model for the straight fluid-filled pipe may now be found by elimination of the shell variables from the equations (B.8-14). After some manipulation these will lead to a set of 14 first order differential equations. The resulting equations are given in section 2.7.

NOMENCLATURE

Roman undercast:

a	mean radius
a_i	internal radius
a_e	external radius
b	width of pump impeller at the outlet
c	wave velocity
\check{c}	approximate wave velocity (defined in section 2.4)
c_a	velocity of sound in the unconfined fluid
c_p	plate wave velocity in the pipe wall $(E_s/\rho_s(1-\nu^2))^{1/2}$
$cond()$	matrix condition number
$det()$	matrix determinant
f	frequency
f_c	cut-on frequency of $n=1$ waves in the fluid
f_{en}	cut-on frequency of $n=n$ waves in the shell
ff	elbow flexibility factor
h	wall thickness
i	$(-1)^{1/2}$
k	wavenumber (ω/c)
n,m	mode numbers
n	pump speed
n_s	specific pump speed $(nQ^{1/2}H^{-3/4})$
m'	mass per unit length of pipe and fluid
p	dynamic pressure
q	dynamic fluid volume velocity
$\{r,\theta,z\}$	cylindrical coordinates
t	time
$\{u,v,w\}$	shell displacement vector in cylindrical coordinates
$\{u_x,u_y,u_z\}$	shell displacement vector in Cartesian coordinates
$v_f v$	axial fluid displacement
$\{x,y,z\}$	Cartesian coordinates

Roman capital:

A_f, A_s	cross-sectional area of fluid, pipe wall
A_{nm}	wave amplitude
[B]	boundary condition matrix
C	compliance
D	distensibility parameter or pump impeller diameter

$E(\)$	ensemble average
E_s	Young's modulus of elasticity
FL	fluid loading parameter
$\{F_x, F_y, F_z\}$	force vector in Cartesian coordinates
G_{xx}	auto-power spectrum
G_{xy}	cross-power spectrum
G_s	shear modulus of elasticity ($E_s/2(1+\nu)$)
H	pump head
H_n	Hankel function
H_{xy}	frequency response function
[I]	identity matrix
$Im(\)$	imaginary part
I_s	second moment of inertia
J_n	Bessel function
J_s	polar moment of inertia
K	stiffness
K_f	fluid bulk modulus of elasticity
L	length or inertance
[L]	non-dimensional shell equations of motion matrix
L_p	pressure level
M	mass
$\{M_x, M_y, M_z\}$	moment vector in Cartesian coordinates
$\{M_z, M_\theta, M_{z\theta}\}$	thin shell moment resultants
N_{avg}	number of averages
$\{N_z, N_\theta, N_{z\theta}, Q_z, Q_\theta\}$	thin shell force resultants
P_{nm}	complex amplitude of modal pressure
P_{zf}, P_{zs}	fluid- and structure-borne axial energy flow
Q	state vector or pump flow rate
R	radius of curvature or resistance
R_{nm}	reflection coefficient
Re	Reynolds number
$Re\{ \}$	real part
S	stiffness
[T]	transfer matrix
$\{U_{nm}, V_{nm}, W_{nm}\}$	complex amplitudes of modal shell displacement
Y	admittance or mobility ($1/Z$)
Y_o	specific admittance
Z	impedance

Greek undercast:

α	rotation angle
β^2	wall thickness parameter ($h^2/12a^2$)
γ	bend angle
γ_{nm}	radial wavenumber
γ_{xy}^2	coherence function
$\{\varepsilon_z, \varepsilon_\theta, \gamma_{z\theta}\}$	strain components
$\varepsilon[]$	relative error
ζ	see eq.(3.24)
η	loss factor
κ	non-dimensional wavenumber (ka)
κ_s	shear coefficient ($2(1+\nu)/(4+3\nu)$)
λ_m	eigen-value
μ	mass ratio ($\rho_f A_f / \rho_s A_s$)
ν	Poisson's ratio or kinematic viscosity
ρ_f, ρ_s	density of fluid, shell
σ	see eq.(3.20)
$\{\sigma_z, \sigma_\theta, \tau_{z\theta}\}$	stress components
$\{\phi_x, \phi_y, \phi_z\}$	rotation vector in Cartesian coordinates
$\{\xi_z, \xi_\theta, \xi_r\}$	fluid displacement vector in cylindrical coordinates
χ	see eq.(3.24)
ω	angular frequency

Greek capital:

Δ_{nm}	axial transducer spacing
$\{\Delta p, \Delta q\}$	pump source vector
ΔP	static pressure difference across the pump
Φ	pump capacity coefficient, see eq.(6.6)
Ψ	pump head coefficient, see eq.(6.6)
Ω	non-dimensional frequency ($\omega a / c_p$)

super- and subscripts

d	discharge
e	external
f	fluid
i	internal or input or imaginary part
n,m	mode number
o	output or shell middle surface
r	radial or real part

s	shell or suction
z	axial
θ	tangential
+,-	propagating in positive,negative z-direction

B	bending wave
E	extensional wave
F	fluid wave
K	known
N	bending nearfield
S	source
T	torsional wave
U	unknown

other symbols:

\hat{x}	Fourier transform
x^*	complex conjugate
\tilde{x}	scaled (see eq.(3.18))
\bar{x}	averaged over a pipe cross-section
$\langle x \rangle_t$	time averaged
$\ x\ $	norm of vector or matrix
$\{x\}$	vector
$[x]$	matrix

REFERENCES

- ÅBOM, M. 1989 Modal decomposition in ducts based on transfer function measurements between microphone pairs. *Journal of Sound and Vibration* **135**(1): 95-114
- ÅBOM, M. 1990 Measurement of the scattering-matrix of acoustical two-ports. Proc. *Internoise'90*: 537-540
- ÅBOM, M., H. BODÉN & J. LAVRENTJEV 1992 Source characterization of fans using acoustic 2-port models. Proc. INCE symposium fan noise, Senlis (France): 359-364
- ÅBOM, M. 1992 A note on the experimental determination of acoustical two-port matrices. *Journal of Sound and Vibration* **155**(1): 185-188
- ABRAMOWITZ, M. & I.A. STEGUN 1972 *Handbook of mathematical functions*. Dover Publications, New York
- ASME BOILER + PRESSURE VESSEL CODE 1992 Section III: Rules for construction of nuclear power plant components. Division I, Subsection NB: Class I components, NB-3686 flexibility factors
- BADIE, R. 1993 *Analysis of unsteady flows in centrifugal pumps: analytical and finite element calculations in a centrifugal volute pump*. PhD Thesis, University of Twente, Enschede
- BARTENWERFER, M. 1980 On hydraulic noise of centrifugal pumps. Proc. *Internoise'80*, Miami (USA): 223-228
- BENDAT, J.S. & A.G. PIERSOL 1980 *Engineering applications of correlation and spectral analysis*. Wiley & Sons, New York
- BISTAFA, S.R., G.C. LAUCHLE & G. REETHOF 1989 Noise generated by cavitation in orifice plates. *ASME Journal of Fluids Engineering* **111**: 278-289
- BLEVINS, R.D. 1977 *Flow-induced vibration*. Van Nostrand Reinhold, New York
- BOBROVNITSKII, Y.I. 1992 On the energy flow in evanescent waves. *Journal of Sound and Vibration* **152**(1): 175-176
- BODÉN, H. & M. ÅBOM 1986 Influence of errors on the two-microphone method for measuring acoustic properties in ducts. *Journal of the Acoustical Society of America* **79**(2): 541-549
- BODÉN, H. 1988 Error analysis for the two-load method used to measure the source characteristics of fluid machines. *Journal of Sound and Vibration* **126**(1): 173-177
- BODÉN, H. 1989 *Characterization of fluid machines as sources of fluid borne noise*. PhD Thesis, report TRITA-TAK-8906, Royal Institute of Technology, Stockholm
- BODÉN, H. & M. ÅBOM 1990 Characterization of acoustic two-port sources. Proc. *Internoise'90*: 541-544
- BOLLETER, U., A. STIRNEMAN, J. EBERL & T. MCCLOSKEY 1990 The dynamic transfer matrix of a pump and its use in pumping system design. Proc. ISROMAC-3 on Transport Phenomena & Dynamics of Rotating Machinery, Honolulu: 493-504

- BOLLETER, U. 1993 Interaction of pumps and piping systems with regard to pressure pulsations. Proc. SHF 1st international congress on pump noise and vibration, Clamart (France): 3-10
- BOURGET, S. & F.J. FAHY 1993 Vibrational power flow measurement along thin cylindrical pipe. Proc. CETIM 4th international congress on intensity techniques, Senlis (France): 153-157
- BOVEN, J.F.M. VAN 1993 Sound and vibration transfer through a pipe elbow: a comparison between an analytical model and a finite element model. TNO-TPD report TPD-HAG-RPT-93-050
- BOVEN, J.F.M. VAN 1994 Further development and evaluation of a model for noise and mechanical vibrations of fluid-filled pipe systems. TNO-TPD report TPD-HAG-RPT-94-0058 (Master's thesis, Eindhoven University of Technology)
- BRÉVART, B.J. & C.R. FULLER 1992 Effects of internal flow on energy distributions in fluid-filled elastic pipes. Proc. Internoise'92, Toronto: 527-532
- BRÉVART, B.J. & C.R. FULLER 1993 Active control of coupled wave propagation in fluid-filled elastic cylindrical shells. *Journal of the Acoustical Society of America* **94**(3): 1467-1475
- BRITISH STANDARD INSTITUTION 1990 Methods for determining pressure ripple level generated in hydraulic fluid power systems and components. Part 1. Secondary source methods for pumps. (BS 6335: Part I: 1990)
- BROWN, F.T. 1967 A unified approach to the analysis of uniform one-dimensional distributed systems. *ASME Journal of Basic Engineering* **89**(2): 423-432
- BRUGGEMAN, J.C. 1987 *Flow induced pulsations in pipe systems*. PhD Thesis, Eindhoven University of Technology
- BURGESS, J.C. 1975 On digital spectrum analysis of periodic signals. *Journal of the Acoustical Society of America* **58**(3): 556-567
- CHATEL, G., J.F. LAURO & C. TROLLAT 1993 Experimental analysis of noise generation mechanism in a centrifugal pump. Proc. SHF 1st international congress on pump noise and vibration, Clamart (France): 137-143
- CHU, S., R. DONG & J. KATZ 1994 The effect of blade-tongue interactions on the flow structure, pressure fluctuations and noise within a centrifugal pump. Proc. SHF 1st international congress on pump noise and vibration, Clamart (France): 13-34
- CHUNG, J.Y. & D.A. BLASER 1980 Transfer function method of measuring in-duct acoustic properties. I.Theory, II.Experiment. *Journal of the Acoustical Society of America* **68**: 907-921
- CRAGGS, A. & D.C. STREDULINSKY 1990 Analysis of acoustic wave transmission in a piping network. *Journal of the Acoustical Society of America* **88**(1): 542-547
- CREMER, L., M. HECKL & E.E. UNGAR 1988 *Structure-borne sound*. Springer Verlag, New York

- CUSHIERI, J.M. 1988 Excitation and response of piping systems. *Journal of the Acoustical Society of America* **83**(2): 641-646
- DAVIDSON, L.C. & J.E. SMITH 1969 Liquid-structure coupling in curved pipes. *The Shock and Vibration Bulletin* **40**(4): 197-207
- DAVIDSON, L.C. & D.R. SAMSURY 1972 Liquid-structure coupling in curved pipes II. *The Shock and Vibration Bulletin* **42**(1): 123-136
- DAVIDSON, L.C. 1977 The internal impedance of centrifugal and positive displacement pumps. Proc. ASME noise and fluids engineering winter meeting, Atlanta: 225-231
- D'SOUZA, A.F. & R. OLDENBURGER 1964 Dynamic response of fluid lines. *ASME Journal of Basic Engineering* **86**(3): 589-598
- EL-RAHEB, M. 1981 Vibrations of three-dimensional pipe systems with acoustic coupling. *Journal of Sound and Vibration* **78**(1): 39-67
- EL-RAHEB, M. & P. WAGNER 1985 Harmonic response of cylindrical and toroidal shells to an internal acoustic field. Part I: Theory & Part II: Results. *Journal of the Acoustical Society of America* **78**(2): 738-757
- ESPARCIEUX, P. 1986 *Measurement of vibrational wave characteristics of beams and pipes with and without discontinuity*. PhD Thesis, Institute of Sound and Vibration Research, University of Southampton, UK
- EVERSTINE, G.C. 1986 Dynamic analysis of fluid-filled piping systems using finite element techniques. *ASME Journal of Pressure Vessel Technology* **108**: 57-61
- FAHY, F.J. 1977 Measurement of the acoustic intensity using the cross-spectral density of two microphone signals. *Journal of the Acoustical Society of America* **62**: 1057-1059
- FAHY, F.J. 1985 *Sound and structural vibration*. Academic Press, London
- FIRTH, D. 1981 *The influence of circular bends on acoustic and structural waves in pipes*. PhD Thesis, Institute of Sound and Vibration Research, University of Southampton, UK
- FIRTH, D. & F.J. FAHY 1984 Acoustic characteristics of circular bends in pipes. *Journal of Sound and Vibration* **97**(2): 287-303
- FRANCE, D. & D.W. BILYK 1993 The measurement of pump dynamic impedance for use in piping system dynamic analysis. Proc. SHF 1st international congress on pump noise and vibration, Clamart (France): 251-261
- FRIKHA, S., G. COFFIGNAL, J.L. TROLLE & T.H. CHAU 1990 Analyse des sollicitations dynamiques appliquées sur une structure. *Mécanique Matériaux Électricité* **435**: 6-9
- FRIKHA, S. 1992 *Analyse expérimentale des sollicitations dynamiques appliquées à une portion de structure en service modélisable par la théorie des poutres*. PhD Thesis, Laboratoire de Mécanique des Structures, ENSAM, Paris
- FULLER, C.R. 1981 The effects of wall discontinuities on the propagation of flexural waves in cylindrical shells. *Journal of Sound and Vibration* **75**(2): 207-228
- FULLER, C.R. & F.J. FAHY 1982 Characteristics of wave propagation and energy distribution in cylindrical elastic shells filled with fluid. *Journal of Sound and Vibration* **81**(4): 501-

518

- FULLER, C.R. 1983 The input mobility of an infinite circular cylindrical elastic shell filled with fluid. *Journal of Sound and Vibration* **87**(3): 409-427
- FULLER, C.R. 1984 Monopole excitation of vibrations in an infinite cylindrical elastic shell filled with fluid. *Journal of Sound and Vibration* **96**(1): 101-110
- GUELICH, J.F. & U. BOLLETER 1992 Pressure pulsations in centrifugal pumps. *ASME Journal of Vibration and Acoustics* **114**: 272-279
- HALKYARD, C.R. & B.R. MACE 1993 a wave component approach to structural intensity in beams. Proc. CETIM 4th international congress on intensity techniques, Senlis (France): 183-190
- HAM, A.A. 1981 *On the dynamics of hydraulic lines supplying servosystems*. PhD Thesis. Delft University of Technology
- HORNER, J.L. & R.G. WHITE 1991 Prediction of vibrational power transmission through bends and joints in beam-like structures. *Journal of Sound and Vibration* **147**: 87-103
- JACOB, T. & J.-E. PRENAT 1993 Modelisation de la transmission de perturbations hydro-acoustiques a travers une pompe centrifuge. Proc. SHF 1st international congress on pump noise and vibration, Clamart (France): 243-250
- JONG, C.A.F. DE & J.W. VERHEIJ 1992 Measurement of energy flow along pipes. Proc. 2nd international congress on recent developments in air- & structure-borne sound and vibration, Auburn (USA): 577-584
- JONG, C.A.F. DE, J.W. VERHEIJ & M.H.J. BAKERMANS 1992 Measurement of vibroacoustical energy flow through straight pipes. *Journal of the Netherlands Acoustic Society (NAG Journaal)* **113**: 41-52
- JONG, C.A.F. DE 1992 Een experimentele methode voor het karakteriseren van vloeistof-geluidbronnen in vloeistofge vulde pijpen. TNO-TPD report (in Dutch) TPD-HAG-RPT-92-0241
- JONG, C.A.F. DE, P.C. KRIESELS, J.C. BRUGGEMAN & E. VAN BOKHORST 1993 Measurement of the characteristics of a centrifugal pump as a source of pressure pulsations. Proc. SHF 1st international congress on pump noise and vibration, Clamart (France): 167-174
- JONG, C.A.F. DE & J.W. VERHEIJ 1993 Measurement of vibrational energy flow in straight fluid-filled pipes: a study of the effect of fluid-structure interaction. Proc. CETIM 4th international congress on intensity techniques, Senlis (France): 111-117
- JUNGER, M.C. & D. FEIT 1986 *Sound, structures and their interaction*. MIT Press, Cambridge
- KÁRMÁN, T. VON 1911 Ueber die Formänderung dünnwandiger Rohre, insbesondere federnder Ausgleichrohre. *Zeitschrift des Vereines Deutscher Ingenieure* **55**(45): 1889-1895
- KATHURIYA, M.L. & M.L. MUNJAL 1976 A method for the experimental evaluation of the acoustic characteristics of an engine exhaust system in the presence of mean flow. *Journal of the Acoustical Society of America* **60**(3): 745-751
- KELLOGG COMPANY, THE M.W. 1964 *Design of Piping Systems*. John Wiley & Sons, New

York

- KINNS, R. 1986 Some observations on the achievable properties of diesel isolation systems. Proc. ISSA'86, TNO-TPD, Delft: 265-278
- KLÄUI, E. 1993 A simulation study on the attenuation of fluid borne noise of centrifugal pumps by influencing the acoustic impedance of the pump. Proc. SHF 1st international congress on pump noise and vibration, Clamart (France): 509-514
- KRUISBRINK, A.C.H. & A.G.T.J. HEINSBROEK 1992 Fluid-structure interaction in non-rigid pipeline systems - large scale validation tests. Proc. BHR international conference on pipeline systems, Manchester; Kluwer Academic Publishers, Dordrecht: 151-164
- KUIKEN, G.D.C 1984 Wave propagation in a thin-walled liquid-filled initially stressed tube. *Journal of Fluid Mechanics* **141**: 289-308
- KURTZ, P. 1990 Structure borne intensity in straight and curved bars. Proc. CETIM 3rd International congress on intensity techniques, Senlis (France): 45-51
- LAURO, J.F. & C. TROLLAT 1993 Modelisation hydro-acoustique des pompes centrifuges. Proc. SHF 1st international congress on pump noise and vibration, Clamart (France): 145-152
- LAURENTJEV, J., M. ÅBOM & H. BODÉN 1993 A measurement method to determine the source data of acoustic two-port sources. report TRITA-FKT-9318, Royal Institute of Technology, Stockholm
- LEISSA, A.W. 1973 *Vibration of shells*. NASA technical report SP-288, Washington
- LESMEZ, M.W. 1989 *Modal analysis of vibrations in liquid-filled piping systems*. PhD Thesis, Michigan state university, USA
- LESMEZ, M.W., D.C. WIGGERT & F.J. HATFIELD 1990 Modal analysis of vibrations in liquid-filled piping systems. *ASME Journal of Fluids Engineering* **112**: 311-318
- LIGHTHILL, M.J. 1978 *Waves in fluids*. Cambridge University Press
- LYON, R.H. 1975 *Statistical Energy Analysis of dynamical systems: theory and applications*. MIT Press, Cambridge
- MAKAY, E., J.HOGAN & W. GATES 1993 Be aware of acoustic resonances in pump vane/impeller problems. *Power*, February 1993: 55-58
- MAST, T.D. 1993 *Physical theory of narrow-band sounds associated with intracranial aneurysms*. PhD Thesis, Pennsylvania State University, USA
- MATLAB 1990 *MATLAB 3.5 User's Guide*. The MathWorks Inc., South Natick, USA
- MICHALKE, A. 1989 On the propagation of sound generated in a pipe of circular cross-section with uniform mean flow. *Journal of Sound and Vibration* **134**(2): 203-234
- MONGEAU, L. 1992 *Experimental study of the mechanism of sound generation by rotating stall in centrifugal turbomachines*. PhD Thesis, Pennsylvania State University, USA
- MONTUSSAINT, D. DE, J.L. TROLLE 1992 CIRCUS, code de calcul des vibrations de tuyauteries induites par les écoulements. Proc. SHF 1st international congress on pump noise and vibration, Clamart (France): 329-336

- MÖSER, M., M. HECKL & K.-H. GINTERS 1986 Zur Schallausbreitung in flüssigkeitsgefüllten kreiszylindrischen Rohren. *Acustica* **60**: 34-44
- MORSE, P.M. & K.U. INGARD 1968 *Theoretical acoustics*. 1986 reprint, Princeton University Press, Princeton
- MÜHLE, C. 1975 Schallentstehung bei pumpen. In: *Taschenbuch der technischen Akustik*. ed. M. HECKL & H.A. MÜLLER, Springer Verlag, Berlin
- MUNJAL, M.L. 1987 *Acoustics of ducts and mufflers with application to exhaust and ventilation system design*. John Wiley & Sons, New York
- MUNJAL, M.L. & A.G. DOIGE 1990 Symmetry of one-dimensional dynamical systems in terms of transfer matrix parameters. *Journal of Sound and Vibration* **136**(3), 467-475
- MUNJAL, M.L. & A.G. DOIGE 1990 Theory of a two source-location method for direct experimental evaluation of the four-pole parameters of an aeroacoustic element. *Journal of Sound and Vibration* **141**(2): 323-333
- NANAYAKKARA, S. & N. DUKE PERREIRA 1986 Wave propagation and attenuation in piping systems. *ASME Journal of Vibration, Acoustics, Stress and Reliability in Design*. **108**: 441-446
- NG, S.L. & C. BRENNEN 1978 Experiments on the dynamic behavior of cavitating pumps. *ASME Journal of fluids engineering* **100**: 166-176
- NOISEUX, D.U. Measurement of power flow in uniform beams and plates. *Journal of the Acoustical Society of America* **47**(1.2): 238:247
- OKAMOTO, Y. 1993 A note on the relationship between coherence and acoustic source structure in ducts. report TRITA-FKT-9324, Royal Institute of Technology, Stockholm
- OYADJI, S.O. & G.R. TOMLINSON 1985 Vibration transmission characteristics of reinforced viscoelastic pipes employing complex moduli master curves. *Journal of Sound and Vibration* **102**(3): 347-367
- PAVIĆ, G. 1976 Measurement of structure-borne wave intensity, Part I: Formulation of the methods. *Journal of Sound and Vibration* **49**(2): 221-230
- PAVIĆ, G. 1977 Measurement of sound intensity. *Journal of Sound and Vibration* **51**(4): 533-545
- PAVIĆ, G. 1990 Vibrational energy flow in elastic circular cylindrical shells. *Journal of Sound and Vibration* **142**(2): 293-310
- PAVIĆ, G. 1992 Vibroacoustical energy flow through straight pipes. *Journal of Sound and Vibration* **143**(3): 411-429
- PAVIĆ, G., K. TRDAK & A. BADIE-CASSAGNET 1993 Vibroacoustical characteristics of, and energy flow in fluid-filled pipes. SHF 1st international congress on pump noise and vibration, Clamart (France): 225-232
- PESTEL, E.C. & F.A. LECKIE 1963 *Matrix methods in elastomechanics*. McGraw-Hill, New York
- PETERS, M.C.A.M. 1993 *Aeroacoustic sources in internal flows*. PhD Thesis, Eindhoven

University of Technology

- PETERSSON, B.A.T. 1993 Structural acoustic power transmission by point moment and force excitation, Part I: beam- and frame-like structures. *Journal of Sound and Vibration* **160**(1):43-66
- PINNINGTON, R.J. & R.G. WHITE 1981 Power flow through machine isolators to resonant and non-resonant beams. *Journal of Sound and Vibration* **75**(2): 179-197
- PINNINGTON, R.J. & A. BRISCOE 1992 Using a circumferential transducer to measure internal pressures within a pipe. 2nd international congress on recent developments in air- and structure-borne sound and vibration, Auburn (USA): 829-836
- PINNINGTON, R.J. & A. BRISCOE 1994 Externally applied sensor for axisymmetric waves in a fluid filled pipe. *Journal of Sound and Vibration* **173**(4): 503-516
- PRASAD, M.G. 1991 Characterization of acoustical sources in duct systems - progress and future trends. Proc. Noise-Con'91, Tarrytown, New York: 213-220
- PURSHOUSE, M. 1986 Underwater noise radiation due to transmission through the cooling water system of a marine Diesel engine. Proc. ISSA'86, TNO-TPD, Delft: 155-175
- SEYBERT, A.F. 1988 Two-sensor methods for the measurement of sound intensity and acoustic properties in ducts. *Journal of the Acoustical Society of America* **83**(6): 2233-2239
- SIMPSON, H.C., R. MACASKILL & T.A. CLARK 1966-67 Generation of hydraulic noise in centrifugal pumps. Proc. Inst. Mech. Eng. **181**(3A): 84-108
- SIMPSON, H.C., T.A. CLARK & G.A. WEIR 1967 A theoretical investigation of hydraulic noise in pumps. *Journal of Sound and Vibration* **5**(3): 456-488
- SMEULERS, J.P.M. 1988 Simulation of flow dynamics in pipe systems. Proc. IMechE seminar on gas and liquid pulsations in piping systems, London: 97-109
- SNOWDON, J.C. 1971 Mechanical four-pole parameters and their application. *Journal of Sound and Vibration* **15**(3): 307-323
- SOEDEL, W. 1981 *Vibrations of shells and plates*. Marcel Dekker, New York
- STAHL, B. 1987 Experimentelle Untersuchung zur Schallerzeugung durch die Turbulenz in einer Rohrströmung hinter einer un stetigen Querschnittserweiterung. *Acustica* **63**:42-59
- STEPANOFF, A.J. 1957 *Centrifugal and axial flow pumps*. John Wiley, New York
- STIRNEMAN, A., J. EBERL, U. BOLLETER & S. PACE 1987 Experimental determination of the dynamic transfer matrix for a pump. *ASME Journal of Fluids Engineering* **109**: 218-225
- STULEMEIJER, I.P.J.M. 1981 *Beschreibung der Druckschwankungen in hydrostatischen Anlagen und ihre Auswirkung auf den Luftschall*. PhD Thesis, Eindhoven University of Technology.
- TAVERNIER, J., M. MAGNANI, H. GAGLIARDINI, V. LAGARRIGUE & R. PERRET 1993 Characterisation acoustique d'une pompe centrifuge, modelisation dynamique et validation experimentale. Proc. SHF 1st international congress on pump noise and vibration, Clamart (France): 235-241
- TAYLOR, P.D. 1990 Nearfield structureborne power flow measurements. Proc. international

- congress on recent developments in air- and structure-borne sound and vibration, Auburn (USA): 339-345
- TAYLOR, P.D. 1990 Measurement of structural intensity, reflection coefficient and termination impedance for bending waves in beams. Proc. CETIM 3rd international congress on intensity techniques, Senlis (France): 249-256
- TELFER, A.D. 1993 Darlington fuel damage investigation. Proc. SHF 1st international congress on pump noise and vibration, Clamart (France): 443-456
- TENTARELLI, S.C. 1990 *Propagation of noise and vibration in complex hydraulic tubing systems*. PhD Thesis, Lehigh University, USA
- TERAO, M. & H. SEKINE 1993 Fan acoustical characteristics required for reliable HVAC duct sound prediction. Proc. INCE symposium fan noise, Senlis (France): 343-350
- TESÁR, A. & L. FILLO 1988 *Transfer Matrix Method*. Kluwer Academic Publishers, Dordrecht
- THOMPSON, M.C., K. HOURIGAN & A.N. STOKES 1993 Prediction of the noise generation in a centrifugal fan by solution of the acoustic wave equation. Proc. INCE symposium fan noise, Senlis (France): 197-205
- TIJDEMAN, H. 1975 On the propagation of sound waves in cylindrical tubes. *Journal of Sound and Vibration* **39**(1): 1-33
- TIJSSSELING, A.S. 1993 *Fluid-structure interaction in case of waterhammer with cavitation*. PhD Thesis, Delft University of Technology
- TOURRET, J., A. BADIE-CASSAGNET, G. BERNARD, J.P. FOUCAULT & J. KERMAREC 1985 Experimental studies of noise emission and noise generation from a centrifugal pump. Proc. ASME winter annual meeting, Miami Beach, Florida (USA): paper 85-WA/FE-8
- TROLLÉ, J.L., A. BOYER & X. BIRNIE-SCOTT 1989 Détermination de la matrice de transfert et de la source hydroacoustique de la pompe alimentaire N4 Bergeron-Rateau. Proc. SHF XX^e Journées de l'Hydraulique, Lyon: rapport N° II-11
- TROLLÉ, J.L. & E. LUZZATO 1990 Application of structural intensity for diagnostic in one-dimension problems. Proc. CETIM 3rd international congress on intensity techniques, Senlis (France): 397-404
- TROLLÉ, J.L., P. VAUGRANTE, S. FRIKHA, G. COFFIGNAL 1993 Analyse expérimentale des sollicitations dynamiques appliquées a un réseau de tuyauteries. Proc. SHF 1st international congress on pump noise and vibration, Clamart (France): 371-380
- VDI-RICHTLINIEN 1983 Geräusche bei Rohrleitungen. VDI 3733 *Entwurf*, Verein Deutscher Ingenieure, Düsseldorf
- VEIT, I. 1976 Bestimmung der Schallübertragungsdämpfung van Kompensatoren durch Messung ihrer Vierpolparameter. Proc. DAGA'76, Heidelberg, VDI-Verlag: 675-678
- VERHEIJ, J.W. 1980 Cross spectral density methods for measuring structure borne power flow on beams and pipes. *Journal of Sound and Vibration* **70**(1): 133-138
- VERHEIJ, J.W. 1982 *Multi-path sound transfer from resiliently mounted shipboard machinery*. PhD Thesis, TNO Institute of Applied Physics, Delft

- VERHEIJ, J.W. 1990 Measurement of structure-borne wave intensity on lightly damped pipes. *Noise Control Engineering Journal* **35**(2): 69-76
- VERHEIJ, J.W., M.H.A. JANSSENS & D.J. THOMPSON 1993 An equivalent forces method for quantification of structure-borne sound paths. Proc. Noise-93, St. Petersburg: 55-60
- VERHEIJ, J.W., L.J.M. HOPMANS & F.H. VAN TOL 1993 Shipboard measurements of structural intensity on a rotating shaft and its use for sound path quantification. Proc. CETIM 4th international congress on intensity techniques, Senlis (France): 423-429
- VOS, P.H. DE 1984 Stand van de lawaaibestrijdingstechniek bij pijpleidingsystemen. ICG report (in Dutch) LA-02-05
- WANG, A. & R.J. PINNINGTON 1990 An impedance approach to pipework system analysis using the transmission matrix method. Proc. of the Institute of Acoustics **12**(1): 477-484
- WANG, A. & R.J. PINNINGTON 1993 Investigation of the dynamic properties of the liquid-filled pipework systems. Proc. of the Institute of Acoustics **15**(3): 983-990
- WHATHAM, J.F. 1986 Pipe bend analysis by thin shell theory. *ASME Journal of Applied Mechanics* **53**: 173-180
- WHITE, P.H. & R.J. SAWLEY 1972 Energy transmission in piping systems and its relation to noise control. *ASME Journal of Engineering for Industry* **94**: 746-751
- WHITSON, R.J. & I.M. BENSON 1993 Investigation of the fluidborne noise source flow and source impedance characteristics of a single stage centrifugal pump using a secondary noise source. Proc. SHF 1st international congress on pump noise and vibration, Clamart (France): 175-182
- WIGGERT, D.C., F.J. HATFIELD & S. STUCKENBRUCK 1987 Analysis of liquid and structural transients by the method of characteristics. *ASME Journal of Fluids Engineering* **109**(2): 161-165
- WILKINSON, D.H. 1978 Acoustic and mechanical vibrations in liquid-filled pipework systems. Proc. BNES international conference on vibration in nuclear plant, Keswick (UK): 863-878
- WILLIAMS, E.G. 1991 Structural intensity in thin cylindrical shells. *Journal of the Acoustical Society of America* **89**(4): 1615-1622
- WYLIE, E.B. & V.L. STREETER 1978 *Fluid transients*. McGraw-Hill, New York
- YEO, M.F. & L.J. SCHMID 1989 Wave propagation in solid and fluid structures using finite element transfer matrices. *Journal of Sound and Vibration* **130**(3): 439-452

CURRICULUM VITAE

- 21 maart 1961 geboren the Goirle
- 1973 - 1979 Odulphus Lyceum te Tilburg
diploma Atheneum B
- 1979 - 1986 Technische Universiteit Eindhoven
diploma Natuurkundig Ingenieur
- 1986 - 1989 TNO Fysisch en Electronisch Laboratorium, Den Haag
wetenschappelijk medewerker in de divisie Fysica en Akoestiek
- 1990 - heden TNO Technisch Fysische Dienst - TU, Delft
wetenschappelijk medewerker in de hoofdafdeling Geluid

STELLINGEN *behorende bij het proefschrift "Analysis of pulsations and vibrations in fluid-filled pipe systems" door Christ de Jong, oktober 1994*

1. De overdrachtsmatrix methode is aanzienlijk efficiënter voor het berekenen van trillingsoverdracht in pijp- of balksystemen dan de eindige elementen methode of op reflectie- en transmissiecoëfficiënten gebaseerde methoden, zoals het rekenmodel van Horner.
J.L. HORNER & R.G. WHITE 1991 *Journal of Sound and Vibration* 147(1): 87-103
2. Stulemeijer's beschrijving van drukpulsaties in hydrostatische systemen geeft geen directe informatie over het afgestraalde geluid, aangezien hij het aan de pulsaties gekoppelde trillingsgedrag van de pijpen buiten beschouwing laat.
I.P.J.M. STULEMEIJER 1981 *proefschrift Technische Universiteit Eindhoven*
3. De formules van Simpson *et al.* voor het voorspellen van de bronsterkte van centrifugaalpompen is ten onrechte gebaseerd op metingen waarbij de invloeden van pomp en leidingssysteem niet zijn gescheiden.
H.C. SIMPSON, *et al.* 1967 *Journal of Sound and Vibration* 5(3): 456-488
4. In zijn numerieke berekeningen van de instationaire potentiaalstroming in een centrifugaalpompe veronderstelt Badie dat de stroming stationair is in de inlaat en de uitlaat. In de praktijk zal de stroming aan deze randen echter bepaald worden door de tijdsafhankelijke responsie van het pijpsysteem.
R. BADIE 1993 *proefschrift Universiteit Twente*
5. De door Worman afgeleide uitdrukking voor de hydrodynamische "Bernoulli" kracht op het riet van een klarinet gaat uit van de veronderstelling dat de vergelijking van Bernoulli uniform geldig is in het mondstuk. Deze veronderstelling is echter in strijd met het voor zijn model noodzakelijke verband tussen rietopening en volumedebiet.
W.E. WORMAN 1971 *PhD Thesis, Case Weston Reserve University, Cleveland*
6. De klarinet kenmerkt zich door een rijke klank, een groot dynamische bereik en een hoge mate van flexibiliteit bij de bespeling. Theoretische modellen, zoals die van Schumacher en Brod, schieten te kort in de beschrijving van dit gedrag, aangezien hierin essentiële niet-lineaire verschijnselen zoals de beweging van het riet over de kromming van de baan, de effecten van stroming in de buis en vooral ook de invloed van de bespeler ontbreken.
R.T. SCHUMACHER 1978 *Acustica* 40: 298-309; 1981 *Acustica* 48: 71-85
K. BROD 1990 *Acustica* 72: 72-79
7. In het belang van het merendeel van de bewoners van het stiltegebied Waddenzee dient er naast de beperking van het luchtgeluid ook een eis gesteld te worden aan het maximaal toegestane geluidniveau onderwater.
8. Gezien de kans op het optreden van frontale botsingen zouden de NS het gebruik van duwtreinen uit veiligheidsoverwegingen dienen te vermijden.
9. Het dynamisch bereik van de Compact Disc is overdreven groot voor de meest toegepaste functie, het verdrijven van de stilte uit de gemiddelde huiskamer.